INVESTIGATION OF AIRBORNE TRANSMISSION OF COVID-19 AND OTHER TRANSMISSIBLE AIRBORNE DISEASES IN AIRPLANES, AND PUBLIC INDOOR SPACES USING COMPUTATIONAL FLUID DYNAMICS AND SPATIO-TEMPORAL RISK-MAPS

ABU RAIHAN IBNA ALI

A THESIS SUBMITTED TO THE FACULTY OF GRADUATE STUDIES IN PARTIAL FULFILMENT OF THE REQUIREMENTS FOR THE DEGREE OF MASTERS OF APPLIED SCIENCE

GRADUATE PROGRAM IN MECHANICAL ENGINEERING
YORK UNIVERSITY
TORONTO, ONTARIO

APRIL 2024

Abstract

Airborne transmission through respiratory-generated aerosol is identified as one of the major causes of spreading infectious respiratory diseases such as COVID-19. Assessing the risks associated with virus-laden aerosol exposure in a high-density indoor environment is crucial for the risk mitigation of airborne contagious disease transmission. Identification of the most effective strategies is required for the mitigation of airborne disease transmission in the indoor environment. The Eulerian-Lagrangian method combined with two-way coupling was used to numerically obtain the aerosol transport, spatial distribution, and deposition information in indoor environments using Computation Fluid Dynamics (CFD). The study found that aerosol transmission is highly influenced by different factors such as escalator operational speed, ventilation configuration type, index passenger location, and number of outlets. The highly infection zones change accordingly. Further study is required to determine the impact of other associated factors with different intervention strategies.

Dedication

I dedicate this thesis to my parents, who have been a constant source of inspiration, encouragement, and support throughout my whole life.

Acknowledgements

At the very beginning, I would like to praise the most gracious and merciful Almighty Allah and express my immense gratitude.

I would like to express my gratitude, and hearty appreciation to my supervisor Dr. Marina Freire-Gormaly, Department of Mechanical Engineering, York University, for her invaluable guidance, unwavering support, active supervision, constructive suggestion, and constant encouragement throughout the entire master's program.

I extend my appreciation to my thesis committee member, Dr. Ronald Hanson, for his time, and in-depth critique of my research.

I am also grateful to my teammates, lab members, and colleagues who provided me with their support, and helpful discussions throughout this journey. Their insightful comments and suggestions were very helpful.

I also want to express my sincere gratitude to my family members, especially my parents, and sisters, for their unconditional love, and encouragement. Their sacrifices, and constant support served as the inspiration and driving force for my academic achievements.

List of Abbreviations

ASHRAE	American Society of Heating, Refrigerating and Air-Conditioning Engineers
AC	Air Conditioner
ACE	Air Change Effectiveness
ACH	Air Changes per Hour
ANSI	American National Standards Institute
ASHRAE	American Society of Heating, Refrigerating and Air-Conditioning Engineers
ASME	American Society of Mechanical Engineers
BFS	Backward-Facing Step
CADR	Clean Air Delivery Rate
CFD	Computational Fluid Dynamics
COVID-19	Coronavirus disease 2019
cRNA	Complementary RNA
CSA	Canadian Standards Association
DME	Downward Moving Escalator
DPM	Discrete Phase Model
DR	Draft Rate
DUV-LED	Deep ultra-violet (DUV) light emitting diodes (LED)
DV	Displacement Ventilation
ECS	Environmental Control System
FFS	Forward-Facing Step
GA	Genetic Algorithm
GCI	Grid Convergence Index

HEPA	High Efficiency Particulate Air [filter]
HRE	Heat Removal Efficiency
HVAC	Heating, Ventilating and Air Conditioning
IAQ	Indoor Air Quality
IMI	Interferometric Mie Imaging
MV	Mixing Ventilation
PD	Percentage Dissatisfied
PF	Protection Factor
PIV	Particle Image Velocimetry
PM	Particulate Matter
PMV	Predicted Mean Vote index
PPD	Predicted Percentage Dissatisfied index
PPE	Personal Protective Equipment
PRESTO!	PREssure STaggering Options
PV	Personalized Ventilation
RANS	Reynolds-averaged Navier–Stokes
RH	Relative Humidity
RMS	Root Mean Square
RMSE	Root Mean Squared Error
RNA	Ribonucleic Acid
RNG	Renormalization Group
SARS	Severe Acute Respiratory Syndrome
SARS-CoV-2	Severe Acute Respiratory Syndrome CoronaVirus 2
SBS	Sick Building Syndrome
SQP	Sequential Quadratic Programming

SSE	Sum of Squared Error
TCID	Tissue Culture Infectious Dose
TCID50	Median Tissue Culture Infectious Dose
TI	Turbulent Intensity
TIL	Total Inward Leakage
TNUI	Temperature Non-Uniformity Indices
TVOC	Total Volatile Organic Compounds
UME	Upward Moving Escalator
UV	Ultraviolet
UVGI	Ultraviolet Germicidal Irradiation
VNUI	Velocity Non-Uniformity Indices
VOC	Volatile Organic Compounds
WHO	World Health Organization

Nomenclature

C_c	Cunningham correction factor
C_D	drag coefficient
C_p	specific heat capacity ($Jkg^{-1}K^{-1}$)
C_{p_p}	specific heat capacity of droplet ($Jkg^{-1}K^{-1}$)
C_s	vapor concentration on the droplet surface ($kg.m^{-3}$)
C_∞	vapor concentration of air ($kg.m^{-3}$)
D	mass diffusion coefficient of water vapor in air
$D_{T,p}$	thermophoretic coefficient
d_p	diameter of droplet (m)
$\vec{F}$	external forces (N)
F_D	drag force (N)
$\vec{F}_{DPM}$	external forces in DPM (N)
F_g	gravity and buoyancy force (N)
$\vec{F}_{lift,q}$	lift force (N)
$\vec{F}_{wl,q}$	wall lubrication force (N)
$\vec{F}_{other}$	other forces in DPM (N)
$\vec{F}_q$	external body force (N)

F_s	Saffman lift force (N)
F_{th}	thermophoresis force (N)
$\vec{F}_{td,q}$	turbulent dispersion force (N)
$\vec{F}_{vm,q}$	virtual mass force (N)
$\vec{g}$	gravitational acceleration ($m\ s^{-2}$)
G_b	turbulent kinetic energy generation because of buoyancy ($J\ kg^{-1}$)
G_k	generation of the turbulent kinetic energy due to the mean velocity gradient ($J\ kg^{-1}$)
h	convection heat transfer coefficient $W\ m^{-2}K^{-1}$
H_{pyrol}	heat of pyrolysis (J/kg)
H_{latref}	latent heat at reference condition (J/kg)
h_{fg}	latent heat (J)
I	unit tensor
K	thermal conductivity ($W\ m^{-1}K^{-1}$)
K_p	thermal conductivity of droplet particle ($W\ m^{-1}K^{-1}$)
k	turbulence kinetic energy ($J\ kg^{-1}$)
Kn	Knudsen number
m_d	mass of droplets (Kg)
$\dot{m}_p$	mass flow rate of the droplet (kg/s)

$m_{p_{in}}$	mass of the droplet on cell entry (kg)
$m_{p,0}$	initial mass of droplets (kg)
$\dot{m_{p,0}}$	initial mass flow rate of injected droplets (kg/s)
$m_{p_{out}}$	mass of the droplet on cell exit (kg)
Nu	Nusselt number
Nu_d	Nusselt number of droplets
Pr	Prandtl number
Re	Reynolds number
T	temperature (K)
$T_{p_{in}}$	temperature of the droplet on cell entry (K)
$T_{p_{out}}$	temperature of the droplet on cell exit (K)
T_{ref}	reference temperature to estimate enthalpy (K)
T_∞	temperature of bulk fluid (K)
p	pressure (Pa)
r	mesh refinement ratio
RH	relative humidity
Sc	Schmidt number
S_{DPM}	user-defined function for dense discrete phase modeling
S_{other}	user-defined function for other source terms

Sh	Sherwood number
t	time (s)
Δt	time step (s)
u	velocity of air ($m\ s^{-1}$)
u_p	velocity of droplet ($m\ s^{-1}$)
$\vec{v}$	velocity ($m\ s^{-1}$)
$\|v\|$	magnitude of velocity ($m\ s^{-1}$)
V_{axial}	axial velocity ($m\ s^{-1}$)

Greek letters

ε	turbulent kinetic energy dissipation rate ($J\ kg^{-1}s^{-1}$)
λ	molecular mean-free-path
λ_a	thermal conductivity of air ($W\ m^{-1}K^{-1}$)
λ_q	Bulk velocity for second phase q ($m\ s^{-1}$)
μ	molecular viscosity ($m^2\ s^{-1}$)
μ_t	eddy viscosity ($m^2\ s^{-1}$)
μ_q	Shear velocity of second phase q ($m\ s^{-1}$)
ρ	density (kg m^{-3})
ρ_p	density of droplet (kg m^{-3})
σ_k	turbulent Prandtl number for turbulent kinetic energy

σ_ε turbulent Prandtl number for rate of dissipation

$\bar{\bar{\tau}}$ stress-tensor (Pa)

Table of Contents

List of Tables

List of Figures

Chapter 1

Introduction

1.1. Background

The severe acute respiratory syndrome coronavirus 2 (SARS-CoV-2) was the cause of the global COVID-19 pandemic. First appearing in Wuhan, the novel coronavirus (SARS-CoV-2) epidemic expanded throughout the world [1, 2]. Airborne viral transmission through respiratory-generated aerosol was identified as one of the major causes of spreading infectious respiratory diseases such as COVID-19. Some hospital-based studies found airborne SARS-CoV-2, indicating that airborne transmission is an important mode of transmission [3, 4]. Many people die every year because of severe acute respiratory syndrome (SARS). In terms of public health, many infectious diseases, such as COVID-19, tuberculosis, and influenza, are prime examples of airborne transmission. During single sneezing or coughing, thousands of droplets of various sizes are produced which remain airborne by becoming droplet nuclei because of the evaporation process. Furthermore, the deposition of the larger droplets on the surfaces from sneezing or coughing around the infected person infects others who come into contact with these surfaces. The dynamics of respiratory secretions and respiratory droplets spreading in the air are fundamental to airborne disease transmission. An in-depth study of the transmission and deposition of droplets and aerosols in different public places is important to predict and control the transmission of infectious respiratory diseases through respiratory aerosol.

1.2. Motivation

An escalator is a continuously moving mechanical device that carries people vertically while moving a staircase between building floors. Because of its tremendous capacity to move huge numbers of people, it is commonly used in various public facilities such as shopping centers, supermarkets, airports, and subways. An escalator was recommended instead of an elevator during the COVID-19 pandemic situation. During the COVID-19 pandemic, they were preferred over elevators for their ability to maintain physical distance. However, the confined space of an

escalator can also be a potential hotspot for the spread of airborne diseases. The study of respiratory aerosols in escalator environments is a relatively underexplored area in current literature. While there is existing research on airborne disease transmission in indoor environments, such as classrooms, lecture halls, bus office rooms, etc., there is a lack of specific focus on the dynamics of respiratory aerosols in escalator settings. Furthermore, the COVID-19 pandemic has highlighted the need for research in this area, as escalators are frequently used in public spaces where maintaining physical distance can be challenging. Understanding the behavior of respiratory aerosols in escalator environments could provide valuable insights for designing effective ventilation systems and other measures to mitigate the risk of airborne disease transmission.

Similarly, aircraft cabins are one of the most crucial spatial indoor environments for the growing concern of infectious airborne disease transmission spreading throughout the respiratory droplets because of the extreme proximity of passengers. The generated respiratory droplets through talking, coughing, or sneezing from an index passenger can remain suspended in the cabin air for an extended period. The cabin ventilation airflow pattern also significantly impacts transporting the virus-laden respiratory aerosol. The literature gap in understanding respiratory aerosols and airborne disease transmission in single-aisle DASH-8 aircraft cabins is notable, as existing research tends to focus more broadly on larger commercial aircraft or general indoor environments. Single-aisle aircraft like the DASH-8 have unique cabin configurations and airflow patterns that can significantly impact the dispersion and deposition of respiratory aerosols. Specifically, there is limited research on how the ventilation system and cabin layout of single-aisle aircraft affect the spread of respiratory droplets. These aircraft typically have different airflow patterns and ventilation rates compared to larger aircraft, which may influence the concentration and distribution of airborne particles.

Modeling of droplets produced from cough will be much more convenient for understanding the aerosol transmission of contagious diseases like different types of influenza and SARS. COVID-19 (Coronavirus disease) is a viral infectious disease that is caused by the SARS-CoV-2 virus. SARS viruses like other common colds and influenza spread predominantly through the droplets produced from the cough and sneezing processes. The droplets spread around the infected people in the escalator and aircraft cabin which is enough to spread SARS viruses. Therefore, it is important to model the cough in the escalator to understand aerosol transport and

deposition information from cough as many people use it daily. Likewise, assessing the risks associated with virus-laden aerosol exposure in a high-density passenger aircraft cabin environment is crucial for risk mitigation of airborne contagious disease transmission. Additional research is still required to identify the most effective strategies for the mitigation of airborne disease infection risk in the aircraft cabin while ensuring the best comfort to passengers.

1.3. Thesis Scope

This study endeavors to model numerically and analyze airborne respiratory disease transmission from respiratory droplets within confined indoor environments such as upward and downward-moving escalators and aircraft cabins. A comprehensive understanding of different factors such as escalator velocities, Relative Humidity (RH), cabin ventilation layouts, index passenger positions, Personal Protective Equipment (PPE), and passenger comfort on the dispersion of respiratory-generated aerosol was explored. This research carried out Computational Fluid Dynamics (CFD) simulations for modeling airborne disease transmission in the indoor environment to analyze airflow patterns and aerosol transmission with quantification of infection risk. Modeling violent respiratory events such as coughing, and sneezing is essential to understand the dispersion and deposition of droplets in a common public environment. The aerosol transport, dispersion, and deposition can provide better insight to provide guidelines for mitigating airborne contagious disease transmission in different spatial geometry of public places. By providing insights into the dispersion and deposition of droplets in indoor environments, this study hopes to contribute to the broader understanding of airborne transmission and inform mitigation strategies for contagious diseases.

1.4. Objectives

The focus of this study is to model airborne disease transmission via respiratory droplet aerosol in the indoor environment, such as aircraft cabins and escalators under varying Heating, ventilation, and air conditioning (HVAC) configurations. The objectives of this study are as follows:

- Explore the characteristics of respiratory aerosol transmission, dispersion, and deposition numerically.
- Quantify the spatiotemporal heterogenous infection risk associated with respiratory virus-laden aerosols.
- Investigate the efficacy of different mitigation strategies, such as ventilation configurations and face masks to reduce airborne disease transmission.

1.5. Research Approach

The CFD simulation program (ANSYS Fluent) was used to model providing deeper insight into predicting the dispersion, transmission, evaporation, and deposition of cough droplets. Three-dimensional, transient, incompressible, viscous models were solved using the Euler-Lagrangian method including coupling between continuous and discrete phases. As a turbulence model, the realizable k-ε RANS model was adopted, which is reasonably accurate and has a lower computational cost than DNS and LES.

1.6. Layout of Thesis

The thesis follows a well-organized layout, commencing with Chapter 1, which introduces the research topic and establishes its significance. Chapter 2 presents a comprehensive review of existing literature, providing a theoretical foundation. Chapters 3 to 6 delve into the numerical methodology and present results and discussions on specific aspects, such as the upward-moving escalator, downward-moving escalator, and aircraft cabin. The concluding Chapter 7 summarizes findings, offers insights, and proposes recommendations for future research. A brief description of the chapters is given below.

Chapter 1: Introduction

The chapter introduces the motivation of the present study and its importance. The objectives, scopes, and approach of the research are also mentioned in this chapter.

Chapter 2: Literature Review

This chapter presents a comprehensive review of the previous relevant literature on the modeling transmission of respiratory aerosol in different spatial geometries, as well as highlighting the knowledge gap. An attempt was made to illustrate an overview of airborne transmission by aerosol of respiratory droplets based on relevant publications and other sources. This section provides a clear understanding of the research design and the rationale behind the chosen methodology.

Chapter 3: Numerical Methodology

The approach of the CFD study is mentioned in detail in this chapter. Besides, a mathematical representation of the airflow and cough droplet transmission is introduced which was solved numerically.

Chapter 4: Results & Discussion: Upward Moving Escalator

A deep insight into the dispersion, transmission, evaporation, and deposition of cough droplets in the upward-moving escalator is presented in this chapter.

Chapter 5: Results & Discussion: Downward Moving Escalator

This chapter provides a thorough understanding of the dispersion, transmission, evaporation, and deposition of cough droplets in the downward-moving escalator.

Chapter 6: Results & Discussion: Aircraft Cabin

Chapter 6 presents the analysis and findings from the study conducted inside the aircraft cabin, highlighting the key findings and implications that can be inferred from the data collected.

Chapter 7: Conclusion and Recommendation

The contributions of the current research are summarized based on the data analysis of the numerical study. Finally, an outline of potential future works is included that could be explored.

Chapter 2
Literature Review

2.1. Respiratory Aerosol

The dispersion of tiny liquid or solid particles in the gaseous medium is called aerosol [5]. The size of the particles in aerosols ranges between 5nm to 100μm [6]. It is often invisible as dust, but when visible it looks like fog. Droplets of saliva produced by respiratory events such as breathing and coughing generate numerous droplets of different diameters. Sneezing and coughing are multiphase turbulent buoyant clouds with suspended droplets [7]. These droplets create aerosol in the air immediately becoming droplet nuclei after releasing from the mouth as shown in Figure **2.1**. SARS viruses, such as COVID-19, spread when people inhale tiny respiratory airborne droplets and aerosols produced by infected persons. A few droplets containing a contagious virus from an index person are enough to contaminate the respiratory tract [8, 9]. Airborne transmission refers to infection spread by smaller droplets and their nuclei. Some hospital-based studies found SARS-CoV-2 in airborne materials, indicating that airborne transmission is an important mode of transmission [3, 4]. Airborne transmission of such contagious infectious diseases is one of the most important routes in the indoor environment [10–12].

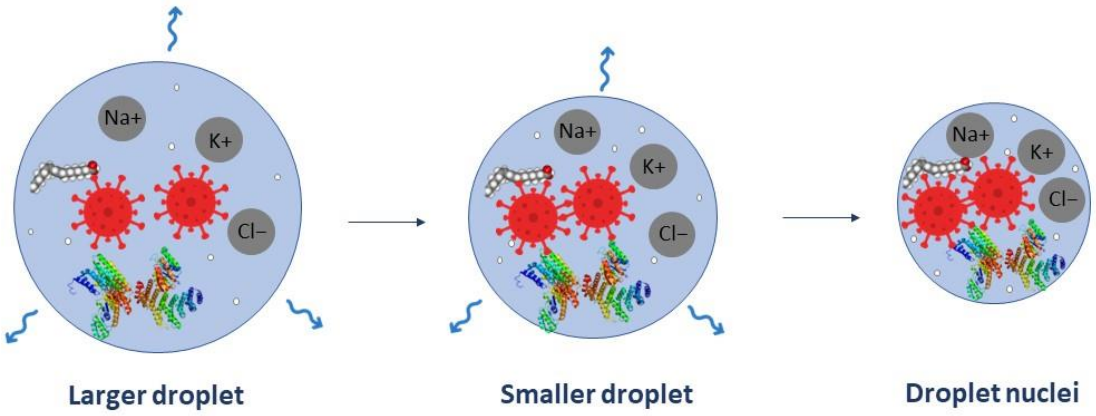

Figure 2.1: Respiratory droplet nuclei formation

Understanding how these aerosols and droplets move is important and many factors influence their movement. The deposition of larger droplets contaminates the surfaces which also spreads the viruses. After a few moments of expelling from the mouth, droplet evaporation enters a relatively stable stage, and the diameter changes by the D^2 law. Droplet size, ambient temperature, and humidity all influence the lifetime of these respiratory droplets. The evaporation rate is higher at lower relative humidity [13]. The difference in water vapor pressure at the droplet surface and the ambient air influences the evaporation rate. The forces such as drag, thermophoresis, buoyancy, and Saffman lift force act on these droplets. Particle inertial separation, turbulent dispersion, electromagnetic radiation, gravitational settling, electrostatic deposition, Brownian motion, thermophoresis, and interception effect are some of the mechanisms involved on the suspended droplets [5]. The larger droplets exhibit higher axial penetration and higher vertical drop than fine droplets.

2.2. Physical Properties of Saliva Droplet

Although the precise composition of the salivary fluid is unknown, organic, inorganic ions, and glycoproteins are assumed to be the non-volatile components. Many factors influence the composition of human saliva, including gender, age, diet, drugs, size of the salivary gland, circadian rhythm type, physiological status, etc. The volatile portion is mainly water with 95% or more of the composition whereas the remaining non-volatile portion contains Na+, Cl−, K+, protein, glycoprotein, dialysable components, and fatty acids. [14–16]. The fluid is viscoelastic because of the constituents like soluble biopolymers and large glycoproteins. Therefore, the physical properties of saliva are closest to water having the density, dynamic viscosity, and surface tension of water as the following table [17–19]:

Table 2.1. Properties of Saliva Droplets

Properties	**Value**	**Unit**
Density, ρ	1000	kg/m^3
Dynamic viscosity, μ	1	mPa.s
Surface tension, σ	60	mN/m

2.3. Size Distributions of Respiratory Droplets

Expelled droplets generated through the atomization process of saliva during respiratory phenomena such as breathing, speaking, coughing, and sneezing can carry SARS-CoV-2 viruses, resulting in airborne transmission. SARS-CoV-2 has a diameter of approximately 60 *nm* -140 *nm* [20] which is 3,000 times smaller in comparison to the size of human hair. The size comparison of SARS-CoV-2 and the expiratory droplet is illustrated in Figure **2.2**.

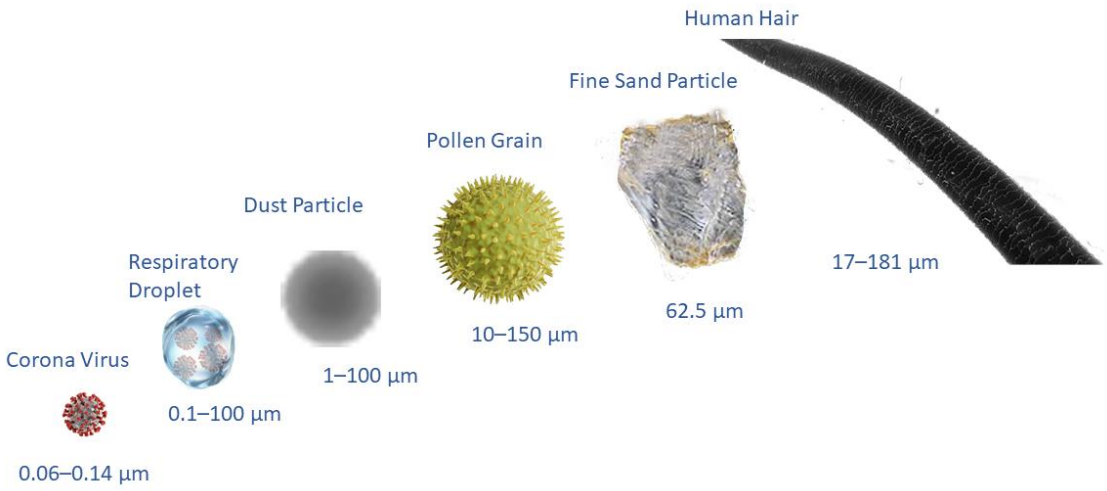

Figure 2.2: Size Comparison of SARS-CoV-2 and Respiratory Droplet

The expelled droplet and droplet nuclei have a wide range of diameters of 0.1 μm to 500 μm [21, 22]. The majority of the droplet and droplet nuclei are between 2 μm and 100 μm [23]. The larger droplets larger than 100 μm are too heavy to float in the air and get deposited immediately on nearby surfaces. Lee et al. [24] studied the size distribution of cough-generated aerosols in an indoor environment. They found that the majority of the particles produced by coughing were below 5 μm. In another investigation, Duguid [16] discovered that 4 μm to 8 μm droplets were the most common in speaking, sneezing, and coughing using direct micrometry technique. Chao et al. [25] measured a mean geometric droplet diameter of 13.5 μm during coughing, and 16 μm during

speaking using the Interferometric Mie Imaging (IMI) method. Fairchild and Stamper [26] used an optical particle counter (OPC) to measure the range of droplets during breath exhalation from 0.09 μm to 3.0 μm.

2.4. Expelled Respiratory Droplet Velocity

The peak velocity and the number of droplets are much higher during a sneeze than the coughing phenomena. Sneezing also generates a higher number of smaller droplets than coughing. Zhao et al. [27] investigated sneezing numerically and found that droplets of sneezing travel a higher distance than the normal breathing process. The maximum droplet velocity during a sneeze is between 12 *m/s* to 15 *m/s* [28]. Bahl et al. [29] used the light-sheet illumination method to visualize the droplets of sneezing to find the velocities of droplets. The experiment found that 80% of droplets travel at velocities less than 5 *m/s* while 1% of droplets travel at velocities greater than 10 *m/s*. Approximately 180 ms to 200 *ms* was detected for a complete sneezing process. On the contrary, a normal coughing process lasts approximately 0.4 *s* which was found in a study conducted by Gupta et al. [30]. Chao et al. [25] found an average velocity of 11.7 *m/s* during coughing, while that was 3.1 *m/s* during speaking with the help of the Particle Image Velocimetry (PIV) method. Another PIV study, conducted by Zhu et al. [19], found that the average cough velocity is 11.2 *m/s*, with peak cough velocity ranging from 6 *m/s* to 22 *m/s*.

2.5. Traveling Distance of Droplets

The larger expiratory droplets, regardless of airflow, follow a ballistic trajectory, whereas the smaller droplets are buoyant and produce aerosols [7]. The traveling distance of droplets of aerosol largely depends on the gravitational force, drag force, buoyant force, temperature, humidity, and flow velocity. The buoyant force of smaller droplets in the aerosol easily overcomes gravity force [31]. These tiny droplets, therefore, get suspended in the air for a long time causing airborne transmission by traveling long-distance [32–34]. A droplet nucleus is the final product of a respiratory droplet after being released into the air for a sufficient time. A 60 μm droplet becoming nuclei of 19 μm diameter can travel more than 4 *m* at 0% RH while a 100 μm droplet passes a mean distance of 1 *m* [35]. Using a high-speed camera at 1000 frames-per-second, L.

Bourouiba [36] discovered that larger droplets are deposited within 2 m of the mouth, whereas smaller droplets can travel up to 6 m to 8 m during a sneeze. According to Parienta et al. [37], droplets of 16 μm can travel more than 7 m during the coughing process.

2.6. Droplet Existence Time in the Air

Depending on the environmental conditions, the droplet size changes over time. The size of the droplets decreases rapidly in the dry air because of the high evaporation rate which increases the existence time in the aerosol [38]. The deposition and dispersion characteristics of the expiratory saliva droplets depend on the droplet diameter. Stokes' settling law determines the settling time of a sphere under the opposing forces of gravity and air friction [39]. A strong correlation was also found between the amount of aerosol generation and the usage of certain consonants and vowels in speech [40–42]. J. P. Duguid [23] experimentally found that nuclei larger than 4 μm remain airborne for approximately 90 minutes while smaller nuclei remain for longer periods without any artificial disturbance.

2.7. Airborne Infection Risk Model

2.7.1. Wells-Riley Model

The Wells-Riley risk model can predict the risk of airborne infection in a simple well-mixed ventilated room with steady-state infectious pathogens concentration [43]. The quanta of infection contaminants are the foundation of this model. The chance of becoming infected rises if the susceptible person breathes in more quanta. The infection probability according to the Wells-Riley risk model is as the following equation:

$$P_I = \frac{C}{S} = 1 - \exp\left(\frac{Iqpt}{Q}\right) \tag{2.1}$$

where the infection cases number and number of susceptible people are denoted by C and S. The other symbols I, q, p, t, and Q are the number of index persons, quanta generation rate, inhalation rate of a person (m^3/s), the interval time of exposure, and ventilation rate of the room respectively. The wells-Riley equation can be written in another form as follows:

$$P_I = 1 - \exp(C_i p t) \tag{2.2}$$

Where contaminant concentration (*quanta-hour/m*^{3}) is denoted by C_i.

But it is very difficult to determine the quanta generation rate, a minimum number of pathogens that infect another person. The value of pathogen quanta has not been accurately quantified in the literature. Another limitation of this model is that airborne pathogens decay over time. Additionally, it does not address the spatiotemporal inhomogeneous dispersion of the pathogens. The indoor airflow is usually heterogeneous. The Wells-Riley model is based on the assumption that pathogen quanta are only removed by ventilated airflow. But practically the concentration of pathogens changes because of thermal and chemical conditions, deactivation by UV irradiance, deposition, decay in air, etc.

2.7.2. Spatiotemporal Airborne Infection Risk Model

Li et al. [44] proposed a quantitative spatiotemporal infection model incorporating some biomedical factors that overcome some of the Wells-Riley limitations. The following equation provides insight into the risk of infection depending on the local pathogen concentration:

$$P_I = 1 - \exp\left(-(1-\eta_s)\frac{\ln 2}{\delta\, TCID_{50}}\frac{c(x,t)d_{p,0}^3}{d_p^3}\, C_{RNA} p\, t_e\right) \tag{2.3}$$

Where, η_s, $c(x,t)$, $d_{p,0}$, d_p, p, and t_e represent the efficiency of PPE (mask worn by susceptible person) filtration, the volume fraction of the local pathogens, the diameter of the initial hydrated particle, droplet diameter after shrinking, respiratory ventilation rate, and time of exposure respectively. The model contains three biomedical terms such as δ, $TCID_{50}$, and C_{RNA} which denote the median value, Tissue Culture Infectious Dose (transmissibility), and Respiratory fluid viral load of an infected person (The copies of RNA per unit volume) respectively.

2.8. Aerosol Transmission in Indoor and Confined Environments

The airborne transmission from respiratory droplets has been studied under various spatial indoor conditions and ventilation systems to assess the infection risk. Inadequate airflow and circulation patterns have been demonstrated to be responsible for airborne transmission in indoor

environments [26]. For example, inadequate ventilation was demonstrated to cause the transmission of SARS-CoV-2 in a restaurant in Guangzhou, China [45]. Recently, some studies were conducted using CFD analysis to understand the dispersion of respiratory droplets expelled from coughing and sneezing in classrooms, conference rooms, restaurants, elevators, and public buses [40, 45–49].

2.8.1. Aircraft Cabin

The recirculated fresh air in the aircraft cabin is a mixture of 50 percent filtered air by HEPA filter from the previously supplied air and the remainder from engine bleed air. Fresh cabin air circulates in a circular pattern from ceiling to floor and exits through floor grilles. The whole cabin air volume is continuously exchanged every 2-3 minutes. Designing a healthy and comfortable aircraft cabin environment with a ventilation system is extremely difficult because of its complex geometry and high-density occupants. There are three major types of ventilation configurations as illustrated in Figure **2.3**: mixing, displacement, and personalized ventilation systems. A mixing type of ventilation system, used by most aircraft manufacturers, supplies fresh air from the inlets placed beneath the ceiling-mounted luggage compartment or from the top sidewall [50–52]. Heat and pollutants are removed through the exhaust grills located on the floor on both sides of the cabin after the recirculation of the fresh air. Infectious airborne diseases such as SARS and influenza can easily be transmitted from one index passenger to another passenger in the mixing ventilation system. But the over-thermal comfort is quite good in this sort of ventilation system.

The displacement ventilation provides fresh air through vents located on the floor. The fresh air exchanges heat with the passenger body, resulting in thermal plumes that travel to the ceiling exhaust vents. Thermal stratification occurs in such ventilation configurations due to the buoyancy effect. The Archimedes number has the potential to significantly influence thermal stratification [53, 54]. A combined displacement and mixing ventilation system can provide high heat removal efficiency while maintaining a lower vertical temperature gradient that elevates thermal stratification [55]. The maximum vertical and horizontal temperature gradients in aircraft cabins recommended by ANSI/ASHRAE Standard 161-2013 are 2.8 $^{\circ}C$ and 4.4 $^{\circ}C$, respectively [56]. The heat from human bodies produces thermal plumes that transport the contaminated air toward the ceiling. One of the major drawbacks of this configuration is that rising warmer air near the

ceiling traps particles, which are then removed by the incoming fresh air current. These trapped particles are close to the passengers' breathing zones. Buildings commonly use displacement ventilation systems due to improved air quality. Displacement ventilation is more energy efficient than mixing ventilation [57, 58].

Personalized ventilation (PV) provides clean air directly to the breathing zone of the passengers which has high ventilation effectiveness. The fresh air serves as a barrier between contaminants inside and outside the breathing zone. PV configuration in the aircraft cabin can provide better air quality though the risk of the draft is higher than DV system [51, 59, 60].

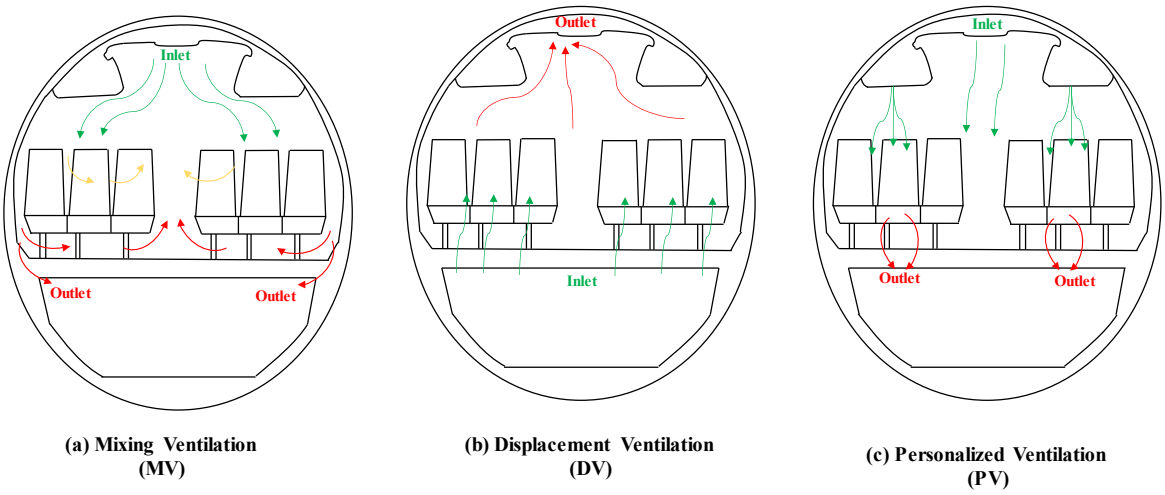

Figure 2.3: Types of ventilation configurations (a) Mixing Ventilation (MV), (b) Displacement Ventilation (DV), and (c) Personalized Ventilation (PV)

There are two major sources of airborne contaminants in an aircraft cabin: expiratory sources from respiratory phenomena such as speaking, coughing, and sneezing, and non-expiratory sources such as dead human skin cells shedding, and dust. Contaminants can be both gaseous and particulate. Volatile organic compounds (VOC), carbon dioxide (CO_2), carbon monoxide (CO), nitrogen oxides, ozone, ethanol, aldehydes, and nicotine are all examples of gaseous pollutants in aircraft cabin [61, 62]. The source of ethanol in the cabin is mainly wet wipes. Ozone is a natural source component of the atmosphere that increases significantly at altitudes of 11,000 *m* (36,000 *feet*) or

higher (in the upper troposphere or lower stratosphere) [63, 64]. At 11,000 m altitude, the air is much pure, dry, and almost pollutant particle-free but with a lower oxygen level. The outside cabin air temperature at that altitude is around -55 °C [65]. The content of moisture in the air is close to zero. The atmospheric pressure is roughly one-fifth that of sea level pressure. The crew members and passengers in the cabin are protected from the harsh environment by an Environmental Control System (ECS) that distributes the properly comfortable and safe conditioned air inside the cabin using an air distribution system. This outside air is extracted as bleed air from the engine (compressor stage) and is delivered in measured amounts to the cabin with filtered cabin air from the HEPA filter maintaining a 50:50 ratio. The reason for using 50% recirculated air is that 100% bleed air consumes significantly more fuel [66]. An ozone catalytic converter is recommended for aircraft flying on routes within which ozone exposure is predicted to be significant [67, 68]. All passenger aircraft must be equipped with HEPA filters capable of removing airborne particles, bacteria, and viruses, as small as 0.3 μm with a 99.97% efficiency [69].

Aerosol dispersion and ventilation effectiveness have been studied by many researchers using different types of tracer gas, including SF_6, CO_2, and N_2O [58, 70–74]. For example, Singer et al. [70] investigated the effects of supplying air from HVAC in meetings and classrooms using carbon dioxide (CO_2) tracer gas. The vertical temperature stratification and perfectly mixed (ERM) metrics were used to assess the exposure to aerosol particles from speaking having a diameter of less than 5μm. The exposure to tracer gas was 2.5 times greater in ventilation with heating because of stratification than perfect mixing. In another experimental study, Yin et al. [71] used sulfur hexafluoride (SF_6) tracer gas in a hospital patient ward with displacement and mixing ventilation systems to figure out the risk of airborne infectious disease for the caretaker. The SF_6 concentration was measured at various points using a photoacoustic multigas analyzer. DV configuration with 6 ACH and high exhaust in the breathing zone yielded the best air quality results in their investigation. The displacement ventilation system's performance is highly dependent on the location of the exhaust diffuser. Exhaust diffusers located at the lowest level cause a higher concentration of pathogens than the mixing type. Chung and Hsu [72] found better ventilation efficiency for the same height with opposite inlet and outlet diffuser locations in their CO_2 tracer gas experiments.

Recently, airborne infectious disease transmission in the aircraft cabin has drawn much attention to researchers besides the study of ventilation effectiveness. The prediction and quantification of airborne transmission risk in aircraft cabins are crucial for taking preventive measures. For example, SARS infected 16 people after a flight carrying one symptomatic person and 119 passengers more [75]. The significance of airborne disease transmission in the aircraft cabin was highlighted by this incidence. Zee et al. [76] explored the expiratory cough particles using the CFD approach in a 5-row cabin section with 30 seats of Boeing 737 from different seated positions of index passengers. Half of the non-volatile portion of the droplets were deposited on various surfaces in the cabin, while the other half was removed by the return air grill. The index passenger row had the highest exposure to expiratory particles. On the contrary, window-seated passengers were less exposed to particles than aisle seats. Another experimental investigation also found that passengers in the same index person row are susceptible to most expiratory aerosols [77]. The front and the back rows from the index passenger are the second most infectious zones [76, 77]. Boeing 767 cabin with a double aisle 11-row section fully occupied seats with passengers was modeled numerically by Isukapalli et al. [78] during the disinfection process of the aircraft. Zhang and Chen [51] investigated MV, DV, and PV systems in Boeing 767 aircraft cabins numerically. The investigation revealed that a personalized ventilation system gives better air quality in the cabin. The performance of various ventilation systems in Boeing 737-200 seven-row cabin mockup was evaluated experimentally by Zhang et al [58]. According to the findings, the DV system has higher heat removal efficiency than the mixing type. However, the thermal uniformity in MV configuration is high. Zhang et al. [79] investigated the Airbus A320 cabin using CFD to observe the susceptible exposure index (SEI). More passengers in the vicinity of an index passenger are at risk during the cough than the normal breaths.

2.8.2. Class, Conference, and Office Room

The rate of ventilation and location of the vents in an indoor environment such as a conference room has a significant impact on the trajectories of expelled respiratory droplets [80]. Mirzaie et al. [46] conducted a numerical analysis of cough droplets in a classroom with varying ventilation rates with and without transparent partitions in front of the seats. Their investigation reveals that the occupants without transparent barriers are subjected to higher droplet concentration than those with transparent barriers. An experiment carried out by Curtius et al. [81] demonstrated

that air purifiers with HEPA filters significantly reduced the risks of SARS-CoV-2 transmission in the classroom. Abuhegazy et al. [82] found in their numerical investigation of a classroom that respiratory pathogens reconcentrate at the return duct of the HVAC system indicating the importance of proper disinfection and the use of a filtration system. The application of transparent glass barriers can reduce aerosol transmission significantly. Arjmandi et al. [83] evaluated the risk of infection from respiratory aerosols considering the thermal comfort parameters (PMV, ACE, PPD) of the ventilation systems in the classroom along with multi-objective optimization using a CFD approach. They found that the ventilation configuration with air inlets on the floor and outlets on the ceiling for each occupant demonstrated a straight and shortest particle path line with the lowest possibility of airborne infection. A. Khan [84] looked into how different ventilation designs, like MV and DV, and injection locations affected the spread of airborne pathogens in lecture halls. A modified Wells-Riley model was used to determine the infection risk. It was found that the MV configuration is more effective in reducing the airborne particles. K. Webb [85] used CFD and Machine Learning (ML) to study the effective ventilation strategy along with some performance indicators in the office room. The study utilized ML in an effective way to predict the infection risk quickly.

2.8.3. Cafeteria and Restaurant

Wu et al. [86] investigated a small cafeteria numerically consisting of one counter and six tables. Two cases were studied: 1) sneezing by a standing cashier; and 2) sneezing by a customer. Their investigation revealed that almost half of the droplets were deposited on the opposite customer. The horizontal airflow from the AC behind the cashier spreads respiratory droplets throughout the cafeteria. The inadequate ventilation demonstrated the transmission of SARS-CoV2 in a restaurant in Guangzhou, China [45].

2.8.4. Elevator

Through CFD simulation, Shao et al. [87] assessed the risks of airborne transmission by an infected person in an elevator. Their investigation revealed that the risk of airborne transmission is lower at a higher ventilation rate. The Increased ventilation strengthens the circulation zone causing more deposition of droplets on the nearby wall.

2.9. Safeguards against Aerosol Transmission

2.9.1. Mask

Facemasks have been suggested by the World Health Organization (WHO) in public places for the prevention of COVID-19 transmission. It significantly minimizes the forward traveling distance of virus-laden droplets by half which are expelled from respiratory phenomena, providing personal protection against airborne pathogens. Wearing a mask minimizes lateral dispersion as well. Infection probability is reduced by four times if one wears a mask [88]. However, facemasks are helpful in minimizing the transmission of airborne pathogens to some extent only. Facemasks of various types, such as reusable cloth-based masks, surgical facemasks, and N95 facemasks, have efficacy rates of roughly 30%, 70%, and 95%, respectively. The tiny gaps cause leakage of droplets surrounding the mask instead of a tight fitting contributing to an additional reduction of mask efficiency. This sort of leakage permits respiratory droplets from the outside air to directly contaminate the wearer and vice versa. The following equation can be used to calculate the protection factor (PF) of the facemask:

$$PF = \frac{1}{TIL} \tag{2.4}$$

Total inward leakage (TIL) is the percentage of droplets entering the mask through both the filter and the gaps.

2.9.2. Glass Barrier and Sneeze Shield

Talaat et al. [89] carried out CFD simulations in Boeing 737 cabin to understand aerosol transmission by varying passengers' number and incorporation of sneeze shields with particle diameters of 1 μm to 50 μm. They found that the walls and seats of the cabin were contaminated higher than the ground. It was demonstrated that the reduction of passenger capacity and utilization of sneeze shields on full-capacity flights have approximately the same results. Sneeze shields between passengers in the aircraft cabin can increase droplet deposition to the back portion of seats in front of the index passenger while reducing the lateral dispersion of aerosols to other passengers [89].

2.9.3. Ventilation

The transmission of diseases via aerosol in a confined indoor space is much higher than in the open air. Proper ventilation can assist in lowering the concentration of airborne pathogens, microorganisms, and other contaminants by displacing indoor pollutants through the introduction of outside air into a space. The transmission of the SARS-CoV-2 virus via aerosol in a restaurant in Guangzhou, China, demonstrated the importance of proper ventilation, including air filtration and disinfection [45]. However, it is unknown what the effective minimum ventilation rate is for avoiding airborne transmission. Higher ventilation rate by increasing the fresh air supply is recommended by the American Society of Heating, Refrigerating, and Air-Conditioning Engineers (ASHRAE) [90]. Seppanen and Fisk [91] found the symptoms of Sick Building Syndrome (SBS) 30% – 200% higher in the case of air-conditioned buildings compared with naturally ventilated buildings.

A building can be ventilated using one of three methods: natural, mechanical, or hybrid (a combination of natural and mechanical ventilation). Natural ventilation uses natural forces like buoyancy and wind to provide fresh air inside the room. The extent of natural ventilation largely depends on the climatic conditions, the geometry of the room, the orientation of the building, landscaping, inlet-exhaust arrangement, exterior wind or breeze velocity, the density difference between exterior and interior air, type of ventilation (single-sided ventilation, cross-ventilation, stack ventilation), etc. Thermal buoyancy and wind act as two sources of natural ventilation. Thermal buoyancy refers to the movement of hot air in the upward direction as the density of hot air is less than that of cold air. It is also called as stack effect. The flow rate of air will be high if cross-ventilation is used. The percentage of openings and high exterior wind velocity will further increase the airflow rate. Natural ventilation, on the other hand, may not be sufficient and is often used for auxiliary purposes.

As a result, the mechanical ventilation system is primarily used to improve indoor air quality by diluting contaminants. For mechanical ventilation, the airflow pattern and ventilation rate are very important to achieve a certain air quality. Spot ventilation, another auxiliary system, can improve the performance of both natural and mechanical ventilation systems by removing pollutants from the source. For filtration and disinfection, high-efficiency particulate air (HEPA)

filters and ultraviolet germicidal irradiation (UVGI) are used in conjunction with mechanical ventilation system [92–94]. Pavelchak et al. [95] investigated monitoring airflow characteristics in respiratory isolation rooms (IR) using visible smoke. Their investigation found that 38% of IRs were designed with inappropriate outward airflow. There were many reasons behind the inappropriate outward airflow direction such as imbalanced ventilation systems (54%), shared anterooms (14%), patterns of turbulent airflow 11%), and inaccuracy of automated control systems (10%). Liu et al. [96] investigated the effect of ventilation type on the airborne particle. The study used two types of ventilation systems: mixing ventilation (MV) and displacement ventilation (DV). Improved IAQ was found for the DV system.

2.9.4. UV Disinfection

UV disinfection systems use high-intensity ultraviolet rays (254 nm UV-C) to disinfect bacteria, fungi, and viruses such as influenza, SARS-CoV-2, etc. It should be used without exposure to the human body as exposure to such irradiation has a harmful impact on the eye and skin. The coronaviruses can survive up to 9 days on surfaces like metal, plastic, glass etc. [53]. Ong et al. [97] concluded that SARS-CoV-2 can survive more than an hour in the air. Another investigation reveals that SARS-CoV-2 can survive in aerosols for up to three hours [98]. UV rays with 254 nm wavelength (UV-C) are used to disinfect indoor air and the surfaces of various objects such as clothing, medical instruments, and so on [99–101]. Low-pressure mercury lamp emits such wavelengths. The circulating air disinfector using such irradiation can reduce the risk of airborne transmission by deactivating SARS-CoV-2. A recent investigation carried out by Shimoda et al. [102] showed that irradiation of 265 *nm* from a DUV-LED lamp can inactivate SARS-CoV-2 at the same level as 254 *nm* UV. The use of DUV-LED is expected to significantly reduce the amount of mercury in the environment. The main drawback of UV disinfection systems is that effectiveness decreases as relative humidity rises [103].

2.9.5. Filtration and Disinfection of Contaminated Air

Air purifiers improve IAQ by lowering PM2.5 and TVOC levels [104]. An air purifier is an effective way to reduce the risk of airborne transmission from pathogens transmitted through the air in public spaces [105]. The air purifier uses a combination of HEPA filter, activated carbon

filter, Ionizer, and UV disinfection. HEPA filters can capture dust, pollen, mold spores, some bacteria, and other airborne particles of 0.3 μm. An internal fan draws air into the machine, which then passes it through the filter. Airborne pollutants are trapped when air passes through the HEPA filter. The activated carbon filter is commonly used in conjunction with the HEPA filter in air purifiers which is extremely porous, allowing it to absorb specific types of impurities from the air such as odors, gases, and vapors from things like smoke and other volatile organic compounds. Furthermore, an ionizer is used that uses negative ions to remove certain airborne particles by settlement. However, none of these technologies can inactivate airborne pathogens and microorganisms. Therefore, UV irradiation is used in air purifiers to disinfect airborne pathogens and microorganisms.

The required time to filter the fraction of particles from air can be estimated from the following equation:

$$C(t) = C_0 e^{-\left(\frac{CADR}{v}\right)t} \tag{2.5}$$

where initial particle concentration and particle concentration at time t are denoted by C_0 and $C(t)$. CADR is clean air delivery rate, whereas the volume of air being filtered is v.

Chapter 3
Numerical Methodology

3.1. Computational Domain

The computational domain is the region in which the simulation is carried out to solve the problem. The details of the escalator and aircraft cabin computational domains are given below.

3.1.1. Escalator

Figure **3.1** illustrates the computational domain that was discretized into the computational grid to solve discretized equations. Simplification of the computational domain was made to avoid complexity and high computational cost.

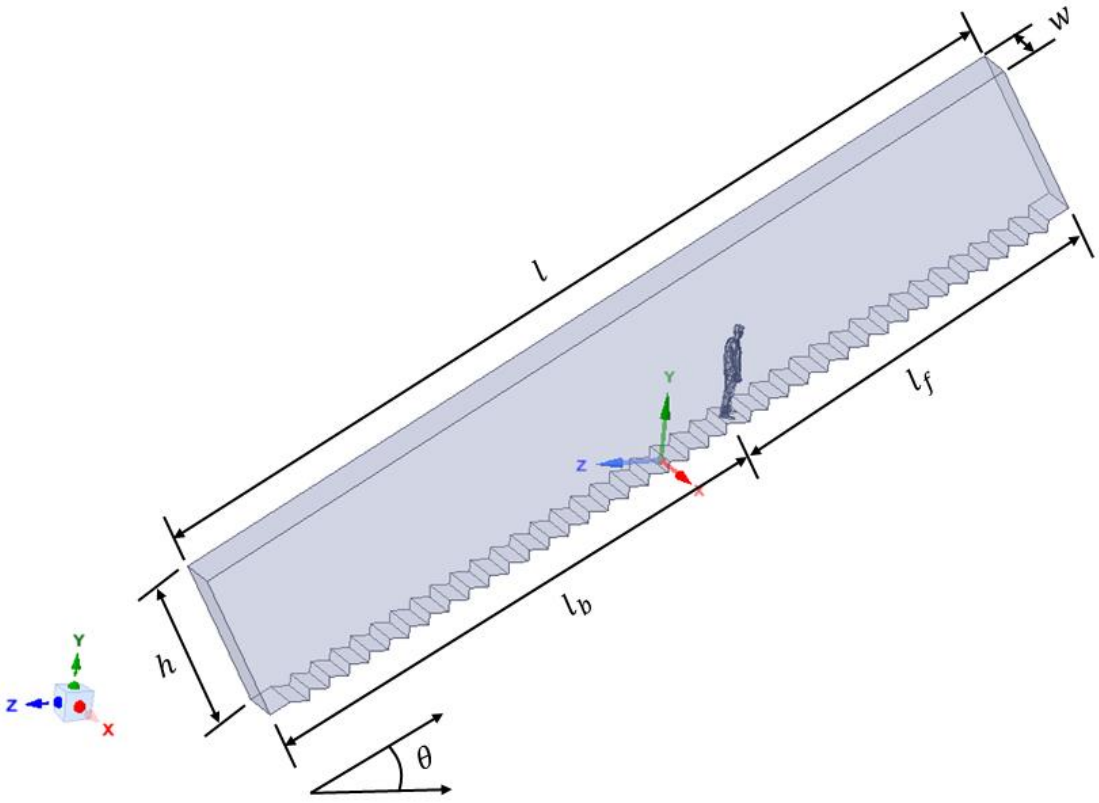

Figure 3.1: Computational Domain of Escalator

The coordinate shown in Figure **3.1** was used as a reference point to calculate the data of other points. The length and width of the escalator are denoted by l and w. h represents the height of the computational domain. The slop of the upward and downward-moving escalator is expressed using θ. The manikin on the escalator was chosen as a frame of reference. l_f and l_b are the distances from the front and backside of the man's location, respectively. The angle of inclination for the escalator should not exceed 30° according to ASME A17.1-2013/CSA B44-13 of the American Society of Mechanical Engineers (ASME) and Canadian Standards Association (CSA) Group [106]. Therefore, the angle of inclination of the escalator (θ) was selected at 30°. The parameters of this computational domain are given in the following table.

Table 3.1. Values of the parameters

Symbol	Values
l	17.6 m
w	0.81 m
h	3.3 m
l_f	7.32 m
l_b	10.28 m
θ	30°

The height of the man was selected as 1.77 m with a shoulder width of 0.47 m. In general, most manufacturers produce steps of the escalator with a width of 24 in, 32 in, and 40 in. The width of the steps was set to 32 in for the computational domain while the depth of the step was 0.22 m.

3.1.2. Aircraft cabin

The computational domain for the aircraft cabin consists of a single aisle with a total of seven rows. In this configuration, there is a total of 28 passengers seated across the seven rows, with 4 passengers per row. The aisle serves as the main passage for passengers to access their seats and move within the aircraft.

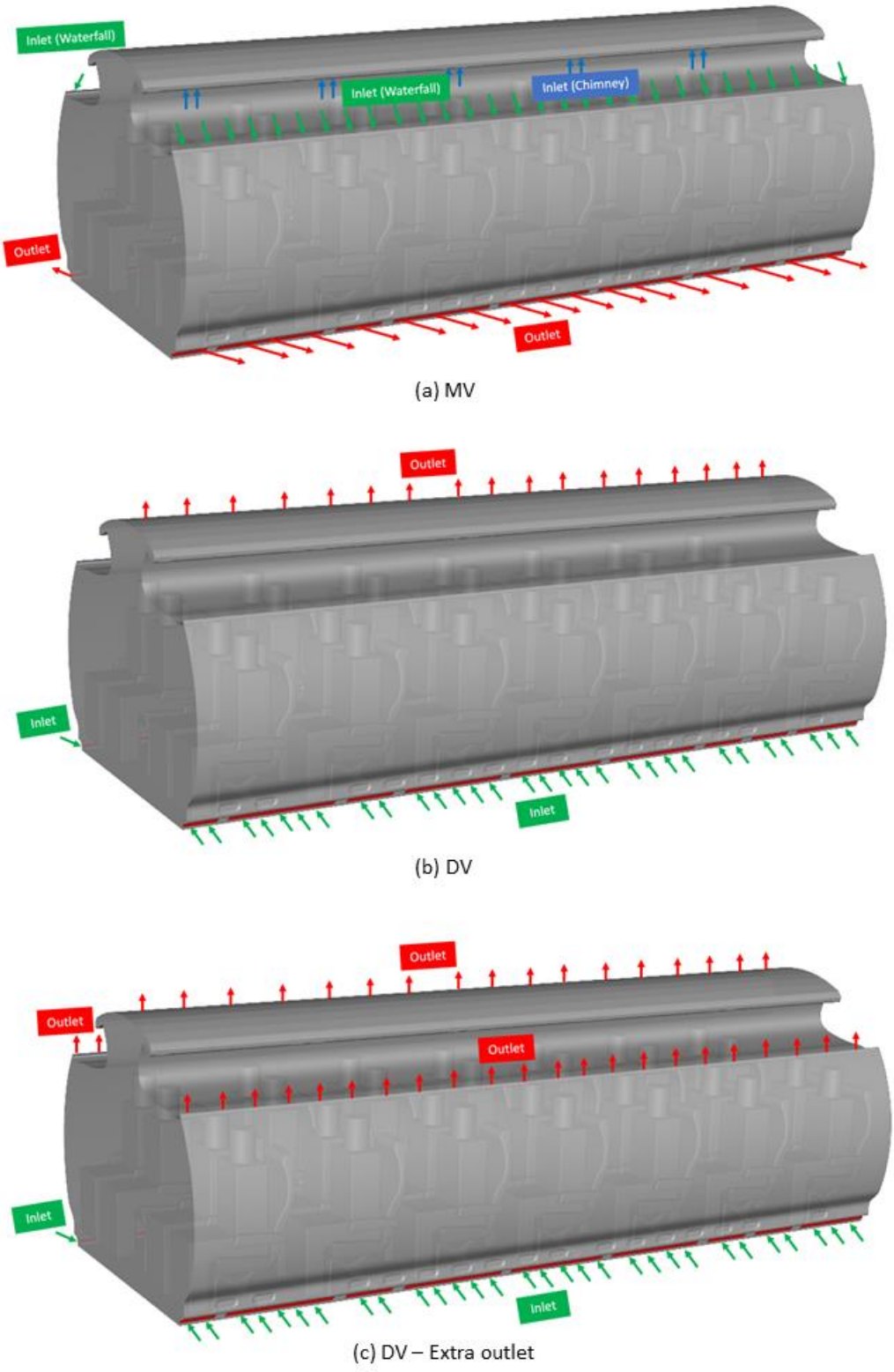

Figure 3.2: Computational domain of aircraft cabin

For the simulation of ventilation within the given aircraft cabin, three distinct ventilation configurations were employed as shown in Figure **3.2**: Mixed Ventilation (MV), Displacement Ventilation (DV), and DV with an additional outlet. Fresh air is provided near the ceiling while cabin air is removed near the floor in the MV configuration. In DV configuration, fresh air is introduced at low-level positions near the floor, allowing it to slowly displace and push the contaminated warmer air toward ceiling exhaust vents.

3.2. Assumptions of the Computation

Some assumptions were used to simplify the geometry to reduce the computational cost. The following assumptions were used for the calculation:

1. The Brownian motion of the droplets is negligible.
2. Droplets were spherical.
3. The movement of the human body while standing on the escalator was neglected.
4. The airflow from human breathing was neglected.

3.3. Mathematical Modelling of Flow

The modeling of cough aerosol in the escalator was done based on the Euler-Lagrange multiphase model [107, 108] approach. The first phase was air while droplets of cough were the second phase. Air was treated as the continuous phase by solving the Navier-Stokes equations which was composed of mainly two species. These two species were air and water vapor. Droplets of cough were modeled as discrete phases tracking a large number of particles using the Lagrangian approach. The Boussinesq model is used to include the effect of buoyancy.

3.3.1. Governing Equation

The solution solved some governing equations and auxiliary equations. The governing equations for the analysis are developed below. The governing equations include the conservation of mass, momentum, energy, and species. The common form of the continuity equation for both compressible and incompressible flow is as follows:

$$\frac{\partial \rho}{\partial t} + \nabla.(\rho \vec{v}) = S_{DPM} + S_{other} \tag{3.1}$$

The conservation of momentum is expressed as follows for a non-accelerating frame of reference:

$$\frac{\partial}{\partial t}(\rho \vec{v}) + \nabla.\rho|v\rceil\vec{v} = \nabla.\bar{\bar{\tau}} - \nabla\, p + \rho\vec{g} + \vec{F}_{DPM} + \vec{F}_{other} \tag{3.2}$$

where $\bar{\bar{\tau}}$ is the stress tensor which is expressed by the following equation:

$$\bar{\bar{\tau}} = \mu\left[(\nabla\vec{v} + \nabla\vec{v}^{T}) - \tfrac{2}{3}\nabla.\vec{v}I\right] \tag{3.3}$$

here, molecular viscosity and unit tensor are denoted by μ and I.

The momentum equation for the second phase (q) represents the following equation:

$$\frac{\partial}{\partial t}\left(\alpha_q\rho_q\vec{v}_q\right) + \nabla.\left(\alpha_q\rho_q\vec{v}_q\right) = -\alpha_q\nabla p + \nabla.\bar{\bar{\tau}}_q + \alpha_q\rho_q\vec{g} + \sum_{p=1}^{n}\left(\vec{R}_{pq} + \dot{m}_{pq}\vec{v}_{pq} - \dot{m}_{qp}\vec{v}_{qp}\right) + \left(\vec{F}_q + \vec{F}_{lift,q} + \vec{F}_{wl,q} + \vec{F}_{vm,q} + \vec{F}_{td,q}\right) \tag{3.4}$$

here, the stress-tensor is denoted as $\bar{\bar{\tau}}$.

$$\bar{\bar{\tau}} = \alpha_q\,\mu_q\left(\nabla\vec{v}_q + \vec{v}_q^{T}\right) + \alpha_q\left(\lambda_q - \tfrac{2}{3}\mu_q\right)\nabla.\vec{v}_q\bar{\bar{I}} \tag{3.5}$$

here,

$\vec{R}_{pq}$= Interaction force between phases

$\vec{F}_q$= external body force

$\vec{F}_{lift,q}$=Lift force

$\vec{F}_{wl,q}$ = Wall lubrication force

$\vec{F}_{vm,q}$= Virtual mass force

$\vec{F}_{td,q}$=Turbulent dispersion force

μ_q=Shear for second phase q

λ_q= Bulk velocity for second phase q

The conservation of energy equation is expressed as follows:

$$\frac{\partial}{\partial t}(\rho T) + \nabla(\rho u T) = \nabla\left(\frac{k}{C_p}\Delta T\right) + S_T \tag{3.6}$$

3.3.2. Modeling of Discrete Phase

The mass of generated droplets from a cough is comparatively small which satisfies the DPM condition. The droplets are governed by the following equations. Newton's second law is followed in the Lagrangian approach. Particle trajectories are determined by equations of motion in the Lagrangian approach, which emphasizes the behavior of each particle [109]. The Lagrangian method is preferred for determining particle dispersion and motion [110]. The cough droplets satisfy the equation of motion as follows [111]:

$$m_p \frac{dV_p}{dt} = \sum F = F_D + F_g + F_{th} + F_s \tag{3.7}$$

where droplet mass and velocity vector are denoted by m_p and V_p, respectively. The combined force acting on the droplets is denoted by F. F_D is the drag force, F_{th} is the thermophoresis force. The gravity and buoyancy forces are represented by F_g, in the negative and positive direction. F_s is Saffman lift force.

The Reynolds number for the particles was between 0.0027 - 0.027. Stokes-Cunningham-Drag Law was used to calculate the drag force of sub-micron droplets which is as follows:

$$F_D = \frac{18\mu}{{d_p}^2 \rho_p C_c} \tag{3.8}$$

The Cunningham correction factor of Stokes' drag law is denoted as C_c , and is calculated as follows:

$$C_c = 1 + \frac{2\lambda}{d_p}\left(1.257 + 0.4e^{\frac{-.1d_p}{2\lambda}}\right) \tag{3.9}$$

Here, the molecular mean-free-path is denoted by λ.

The thermophoretic force (F_{th}) is the force experienced by a small aerosol particle when it encounters a temperature gradient. This force is represented by the following equation:

$$F_{th} = -D_{T,p}\left(\frac{1}{T}\nabla T\right) \tag{3.10}$$

Here, the thermophoretic coefficient is denoted by $D_{T,p}$, and is calculated as follows:

$$D_{T,p} = \frac{6\pi d_p \mu^2 C_s(K+C_t Kn)}{\rho(1+3C_m Kn)(1+2K+2C_t Kn)} \tag{3.11}$$

$$K = k/K_p \tag{3.12}$$

Knudsen number, $Kn = 2\lambda/d_p$

where C_s=1.7, $C_t = 2.18$, $C_m = 1.14$, λ is the mean free path of the fluid. Fluid and particle thermal conductivity are denoted by K and K_p respectively. T and μ are the local fluid temperature and viscosity of the fluid.

The submicron droplet wall causes a shear rate (gradient in fluid velocity profile) resulting in a lateral lift force which is known as the Saffman's Lift Force. Saffman's Lift Force is typically two orders of magnitude smaller than the Stokes drag-force. It is represented by the following equation [112, 113]:

$$F_s = m_p \frac{2K\upsilon^{\frac{1}{2}}\rho d_{ij}}{\rho_p d_p (d_{lk}d_{kl})^{\frac{1}{4}}}(\vec{u} - \vec{u}_p) \tag{3.13}$$

where the constant value of K is 2.594 and the deformation tensor is denoted by d_{ij}.

The change in droplet temperature mainly depends on evaporation, convection, and radiation. For each droplet, the energy equation is represented as follows:

$$m_p C_p \frac{dT}{dt} = \pi d^2 h(T_\infty - T) + \frac{dm_p}{dt}h_{fg} + Radiation \tag{3.14}$$

The latent heat is denoted by h_{fg}. The radiation of droplets is neglected as the operating temperature is comparatively low. Here, the convective heat transfer coefficient is represented by h which is an empirical correlation. The convective heat transfer coefficient of droplets is expressed as follows:

$$Nu_d = \frac{hd}{\lambda} = 2 + 0.6Re_P^{0.5}Pr^{0.33} \quad (3.15)$$

Where Nu and Pr are the Nusselt number and Prandtl number respectively.

Evaporation takes place if the temperature of the droplet is more than the saturation temperature. In that case, the rate of change in evaporated mass is represented as follows:

$$-\frac{dm_p}{dt} = \pi d^2 K_c (C_s - C_\infty) \quad (3.16)$$

where C_s and C_∞ are vapor concentration on the droplet surface and vapor concentration of air. The vapor concentration of air is estimated by solving the transport equation of the continuous phase. The coefficient of mass transfer is denoted by K_c. The above equation demonstrates that the relative humidity of air directly affects the rate of change in evaporated mass. The difference in concentration between the droplet and air also plays an important role.

The Sherwood number (Sh) is expressed by the following correlation:

$$Sh_d = \frac{K_c d}{D} = 2 + 0.6Re_P^{0.5}Sc^{0.33} \quad (3.17)$$

where Schmidt number is denoted by Sc.

$$Sc = \frac{\nu}{D} \quad (3.18)$$

where the mass diffusion coefficient of water vapor in the air is denoted by D.

The evaporation rate is represented as follows when the temperature of the droplet reaches boiling point:

$$-\frac{dm_p}{dt} = \pi d^2 \left(\frac{\lambda}{d}\right)\left(2 + 0.46Re_d^{0.5}\right) + ln\frac{\left(1+\frac{C_p(T_\infty - T)}{h_{fg}}\right)}{C_p} \quad (3.19)$$

The heat conductivity of air is denoted by λ . The specific heat of bulk flow is represented by C_p.

3.3.3. Turbulence Model

k-ε model is the most widely-used engineering turbulence model which is robust and reasonably accurate. It provides good convergence while not being memory-extensive. It is a semi-empirical

model based on transport equations for turbulence kinetic energy and turbulent dissipation rate. Three k-ε models are commonly used which are the standard k-ε model, the RNG k-ε model, and the realizable k-ε model. Each model has its limitations. In the standard k-ε model, the transport equation of k is derived from the exact equation, while the transport equation for ε is derived using physical reasoning. The weaknesses of the standard k-ε model are poor performance for flows with strong separation, large streamline curvature, and a large pressure gradient. The transport equation for epsilon in the RNG k-ε model has resulted from an effort to solve the Navier-Stokes equation. On the other hand, the realizable k-ε model accurately predicts flows with rotation, boundary layers under significant adverse pressure gradients, and recirculation with good convergence. The realizable k-ε model also shows a better result for low to medium swirl of fluid than the standard k-ε model and RNG k-ε model.

3.3.4. Realizable k-ε Model

The realizable k-ε model [86, 114] was chosen as the turbulent model because of its high accuracy compared to the standard k-ε model. The enhanced wall function was used as the epsilon (ε) equation contains a term that cannot be calculated without the wall function.

3.3.5. Transport Equation of k-ε Model

The transport equation for turbulent kinetic energy (k) was used as follows:

$$\frac{\partial(\rho k)}{\partial t} + \frac{\partial(\rho k u_j)}{\partial x_j} = \frac{\partial}{\partial x_j}\left[\left(\mu + \frac{\mu_t}{\sigma_k}\right)\frac{\partial k}{\partial x_j}\right] + G_k + G_b - \rho\varepsilon - Y_M + S_k \tag{3.20}$$

And the transport equation for turbulent dissipation rate (ε) was:

$$\frac{\partial(\rho\varepsilon)}{\partial t} + \frac{\partial(\rho\varepsilon u_j)}{\partial x_j} = \frac{\partial}{\partial x_j}\left[\left(\mu + \frac{\mu_t}{\sigma_\varepsilon}\right)\frac{\partial \varepsilon}{\partial x_j}\right] + \rho C_1 S\varepsilon - \rho C_2 \frac{\varepsilon^2}{k+\sqrt{v\varepsilon}} + C_{1\varepsilon}\frac{\varepsilon}{k}C_{3\varepsilon}G_b + S_\varepsilon \tag{3.21}$$

$$Where,\ C_1 = max\left[0.43, \frac{\eta}{\eta+5}\right] \tag{3.22}$$

$$\eta = S\frac{K}{\varepsilon} \tag{3.23}$$

$$S = \sqrt{2S_{ij}S_{ij}} \tag{3.24}$$

G_k = Generation of the turbulent kinetic energy due to the mean velocity gradient

G_b = Turbulent kinetic energy generation because of buoyancy

Y_M = Fluctuating dilatation contribution in the compressible turbulence to overall the rate of dissipation

σ_k = Turbulent Prandtl number for turbulent kinetic energy

σ_ε = Turbulent Prandtl number for rate of dissipation

$C_{1\varepsilon}, C_2$ are constants

Model Constants:

The default values of model constants $C_{1\varepsilon}, C_2, \sigma_k, and\ \sigma_\varepsilon$ determined from experiments for fundamental turbulent flows and have the following values:

$C_{1\varepsilon} = 1.44, C_2 = 1.9, \sigma_k = 1.0, \sigma_\varepsilon = 1.2$

3.3.6. Turbulent Viscosity Modeling

Eddy viscosity (μ_t) accounts for the transport of momentum by turbulent eddies, which is calculated from the following equation:

$$\mu_t = \rho\, C_\mu \frac{K^2}{\varepsilon} \tag{3.25}$$

C_μ is not constant in the realizable k-ε model which is calculated from the following equation. It is a function of mean strain, rotation rates, and the angular velocity of system rotation.

$$C_\mu = \frac{1}{A_0 + A_S \frac{KU^*}{\varepsilon}} \tag{3.26}$$

Here, U^* is as follows:

$$U^* \equiv \sqrt{S_{ij}S_{ij} + \tilde{\Omega}_{ij}\tilde{\Omega}_{ij}} \tag{3.27}$$

$$where, \tilde{\Omega}_{ij} = \Omega_{ij} - 2\varepsilon_{ijk}\omega_k \tag{3.28}$$

$$\Omega_{ij} = \overline{\Omega_{ij}} - \varepsilon_{ijk}\omega_k \tag{3.29}$$

The mean rate of rotation tensor is denoted by $\overline{\Omega_{ij}}$ with an angular velocity ω_k. A_0 and A_s are model constants which are as follows:

$$A_0 = 4.04, A_s = \sqrt{6}\cos\varphi \tag{3.30}$$

where,

$$\varphi = \frac{1}{3}\cos^{-}\left(\sqrt{6}W\right) \tag{3.31}$$

$$W = \frac{S_{ij}S_{jk}S_{ki}}{\tilde{S}^3} \tag{3.32}$$

$$\tilde{S} = \sqrt{S_{ij}S_{ij}} \tag{3.33}$$

$$S_{ij} = \frac{1}{2}\left(\frac{\partial u_j}{\partial x_i} + \frac{\partial u_i}{\partial x_j}\right) \tag{3.34}$$

3.3.7. Wall Function

The fluid flow near the wall is always laminar type. The k-ε model was not formulated for the near-wall flow phenomena like laminar flow. The model was developed primarily for the completely turbulent condition. A damping function is required to provide a bridge between the completely turbulent flow in the main zone and the near-wall laminar flow which is called the wall function. The wall function is an empirical function that adds computation cost to the solution. Enhanced wall treatment was chosen as a wall function for the near-wall effects. It combines the linear and logarithmic laws of the wall using the following function:

$$u^+ = e^{\Gamma}u^+_{lam} + e^{\frac{1}{\Gamma}}u^+_{turb} \tag{3.35}$$

where Γ is the blending function which is as follows:

$$\Gamma = -\frac{a(y^+)^4}{1+by^+} \tag{3.36}$$

where the constants a and b are 0.01 and 5 respectively.

3.4. Two-way Coupling between the continuous and discrete phases

An interaction is found between the expelled cough droplets and the air. Mass, momentum, and heat are exchanged between the continuous phase (air) and the discrete phase (droplets). Therefore, two-way coupling between the continuous and discrete phases should be considered to include mass, momentum, and heat transfer. Two-way coupling is obtained by solving the governing equations of continuous and discrete phases until the results in these phases do not change. The mass exchange from cough droplets to air is calculated by evaluating the mass change of a droplet as it travels through every control volume of the continuous phase. This change in the mass of the droplet is included in the continuous phase as the source term. By looking at the difference in momentum of a particle as it goes through each control volume, the momentum exchange from air to droplet is measured. The momentum transfer comes as a sink term in the momentum balance of air. The change in thermal energy of a droplet as it travels through each control volume is used to calculate the amount of heat transfer from the continuous to the discrete phase. The change in mass momentum and energy are calculated by the following three equations:

$$M = \frac{\Delta m_p}{m_{p,0}} \dot{m}_{p,0} \tag{3.37}$$

$$F = \sum \left(\frac{18 \mu C_D Re}{\rho_p d_p^2 24} (u_p - u) + F_{other} \right) \dot{m_p} \Delta t \tag{3.38}$$

where ρ_p, d_p, u_p, $\dot{m}_p$ are the density, diameter, velocity, and mass flow rate of the droplet particle. viscosity and velocity of the fluid are denoted as μ and u. And Re, C_D, Δt, and F_{other} are relative-Reynolds number, drag coefficient, time step, and other forces.

$$Q = \frac{\dot{m_{p,0}}}{m_{p,0}} \left[(m_{p_{in}} - m_{p_{out}}) [-H_{latref} + H_{pyrol}] - m_{p_{out}} \int_{T_{ref}}^{T_{p_{out}}} C_{p_p} dT + m_{p_{in}} \int_{T_{ref}}^{T_{p_{in}}} C_{p_p} dT \right] \tag{3.39}$$

where $\dot{m_{p,0}}$ and $m_{p,0}$ are the initial mass flow rate of injected droplets and the initial mass of droplets. The mass of the droplet on cell entry and exit are $m_{p_{in}}$ and $m_{p_{out}}$. The temperatures of the droplet on cell entry and exit are denoted by $T_{p_{in}}$ and $T_{p_{out}}$. C_{p_p}, H_{pyrol}, H_{latref}, and T_{ref} are heat capacity of the droplet, the heat of pyrolysis, latent heat, and reference temperature to estimate enthalpy.

3.5. Ventilation parameters calculation

3.5.1. Velocity Non-Uniformity Indices (VNUI)

Velocity non-uniformity indices (VNUI) of a ventilation system indicates the uniformity of air distribution in an indoor environment around a person. A lower VNUI value indicates good ventilation system uniformity, while a higher value indicates the worsts. The equation of VNUI can be expressed as follows:

$$K_v = \frac{\delta v}{\bar{v}} \tag{3.40}$$

Where δv and $\bar{v}$ are velocity RMS deviation of airflow and average velocity of all points.

The expression of velocity RMS deviation of airflow is as follows:

$$\delta v = \sqrt{\frac{\sum(\bar{v}-v_i)^2}{n}} \tag{3.41}$$

Where v_i is the velocity of air at point i, and n is the total number of measuring points.

3.5.2. Temperature Non-Uniformity Indices (TNUI)

Temperature non-uniformity indices (TNUI) of air in a ventilation system indicates the uniformity of temperature distribution in an indoor environment around a person. A higher TNUI value indicates a more non-uniform distribution of temperature. The equation of TNUI can be expressed as follows:

$$K_T = \frac{\delta T}{\bar{T}} \tag{3.42}$$

Where δT and $\bar{T}$ are RMS deviation of temperature and average temperature of all points.

The expression of velocity RMS deviation of airflow is as follows:

$$\delta T = \sqrt{\frac{\sum(\bar{T}-T_i)^2}{n}} \tag{3.43}$$

Where T_i is the velocity of air at point *i*, and *n* is the total number of measuring points.

3.5.3. Heat Removal Efficiency (HRE)

The heat Removal Efficiency (HRE) of a ventilation system reflects energy efficiency. The required energy will be lower if the HRE index is higher. The equation of HRE is as follows [55, 57, 115]:

$$HRE = \frac{1}{2}\frac{T_e - T_s}{T_{cabin} - T_s} \tag{3.44}$$

Where T_s and T_e are the temperature of supply and exhaust air. The mean cabin temperature is denoted by T_{cabin}.

3.5.4. Draft Rate (DR)

The percentage of Draft Rate is found by the following equation [116–118]:

$$DR = (34 - T_i)(v_i - 0.05)^{0.62} . (0.37 . v_i . TI + 3.14) \tag{3.45}$$

$$if\ v_i < 0.05\ ms^{-1}, use\ v_i = 0.05\ ms^{-1}$$

$$DR > 100\%, use\ DR = 100\%$$

Where T_i is the temperature of local air in °C, v_i is the velocity of local air in m/s, and TI is the turbulent intensity of local air (%).

TI can be found by the following expression:

$$TI = \frac{\sqrt{\frac{1}{3}(u'^2 + v'^2 + w'^2)}}{V} \tag{3.46}$$

Where mean velocity is denoted by V; u', v', and w' are velocities in the respective directions.

3.5.5. Percentage Dissatisfied (PD)

The Percentage Dissatisfied (PD) refers to the local discomfort because of the temperature difference between the head and ankle level. PD can be estimated by the following equation [117, 119]:

$$PD = \frac{100}{1+exp(5.76-0.856\ .\Delta T_v)} \tag{3.47}$$

Where ΔT_v is the temperature difference between the head and ankle.

3.6. Spatiotemporal Airborne Infection Risk Model

A spatiotemporal infection model, Li et al. [44] model, was coupled with CFD simulations based on the time history of aerosol particle trajectories to quantify the spatiotemporal heterogenous airborne infection risk. The infection risk was calculated based on the following model:

$$P_I = 1 - exp\left(-(1-\eta_s)\frac{ln\,2}{\delta\ TCID_{50}}\frac{c(x,t)d_{p,0}^3}{d_p^3}\ C_{RNA}p\ t_e\right) \tag{3.48}$$

Where, η_s, $c(x,t)$, $d_{p,0}$, d_p, p, and t_e represent the efficiency of PPE (mask work by susceptible person) filtration, the volume fraction of the local pathogens, the diameter of the initial hydrated particle, droplet diameter after shrinking, respiratory ventilation rate, and time of exposure respectively. The parameters for $TCID_{50}$ was set to 4000 *virion*s, $2.35\ \times 10^{15}$ *copies/mL* for cRNA, 5 for δ, and 6 L/Min for p.

3.7. Mesh Independency Analysis

3.7.1. Escalator Domain

Mesh independency was investigated for the 0.6 *m/s* upward-moving escalator at a 30° inclination angle. The ambient temperature and RH were 25℃ and 54%, respectively. The static pressure and axial velocity were taken from a point of P (0,1,1). The differences in static pressure and axial velocity of M1 and M2 meshes are not significant from the first sight of view. The axial velocity of point P was selected to check the Grid Convergence Index (GCI).

Table 3.2. Static pressure at selected point

Mesh	Cells No.	P_{static} (Pa)
M1 (Fine)	1957879	0.0427
M2 (Medium)	708845	0.0445
M3 (Coarse)	284127	0.0686

Grid Convergence Index (GCI)

The Grid Convergence Index (GCI) is used to measure the error caused by grid sensitivity. The GCI expresses how far the computed value deviates from the asymptotic numerical value. Three mesh sizes of h_1, h_2, and h_3 were selected for fine, medium, and coarse meshes respectively. The mesh refinement ratio (r) was 1.5. Mesh independency analysis was investigated using Richardson's extrapolation method [120–122]. This method is used for estimating a higher-order continuum value from a succession of lower-order discrete values.

$$\textit{Mesh refinement ratio, } r = \frac{h_2}{h_1} = 1.5 \tag{3.49}$$

The continuum value at zero grid spacing was estimated from the following equation:

$$(P_{static})_{h=0} = (P_{static})_1 + \frac{(P_{static})_1 - (P_{static})_2}{r^p - 1} \tag{3.50}$$

where the order of accuracy (p) is calculated by the following equation:

$$p = \frac{ln\left(\frac{(P_{static})_3 - (P_{static})_2}{(P_{static})_2 - (P_{static})_1}\right)}{ln\,2} \tag{3.51}$$

The percentage of relative error was estimated as:

$$Error = \frac{(P_{static})_h - (P_{static})_{h=0}}{(P_{static})_h} \times 100 \tag{3.52}$$

Table 3.3. Percentage error for each mesh

Mesh	P_{static} ***(m/s)***	**Error (%)**
$(P_{static})_{h=0}$	0.0419	
M1	0.0427	1.835
M2	0.0445	6.192
M3	0.0686	38.912

The grid convergence index (GCI) was used as a measure of mesh convergence. A low GCI value suggests that the mesh is in the asymptotic convergence area. GCI also indicates the error of discretization. The estimation of GCI is as follows:

$$GCI_{12} = F_s \frac{\left|\frac{(P_{static})_1 - (P_{static})_2}{(P_{static})_1}\right|}{r^p - 1} \times 100 \tag{3.53}$$

$$GCI_{23} = F_s \frac{\left|\frac{(P_{static})_2 - (P_{static})_3}{(P_{static})_2}\right|}{r^p - 1} \times 100 \tag{3.54}$$

where F_s is a security factor whose value is 1.25 having three different meshes [123].

Table 3.4. Result of Grid Convergence Index (GCI)

	Grid Convergence Index (GCI) %
GCI_{12}	2.29
GCI_{23}	29.26

A lower value of GCI indicates that the calculation is within the asymptotic range. The value of GCI_{12} is 2.29% which indicates that the computation has reached a solution within 2.29% of the theoretical asymptotic solution. Therefore, The M1 (Fine) mesh was selected as it gave a lower discretization error and GCI. During the solution, some other variables such as static temperature, pressure coefficient, and drag coefficient were monitored for the solution convergence with residual values.

3.7.2. Aircraft Cabin Domain

The grid size used for the grid independence study was 75 *mm*, 50 *mm*, and 33 *mm*. The velocity profiles at the midplane at two horizontal lines are compared in Figure 3.3(b, c, d) for the different grid sizes. The velocity profile for the medium and fine grids is nearly identical except for some points. A 50 *mm* grid size with 4.68 million cells was chosen considering the computational cost. The grid size was 2 *mm* near the inlet waterfall, 3 *mm* near the inlet chimney, 5 *mm* near the wall chimney, and 10 mm near the outlet in the MV configuration. The same cell size was used for the DV configuration. The average y+ of various surface values was between 2.4 to 8.9.

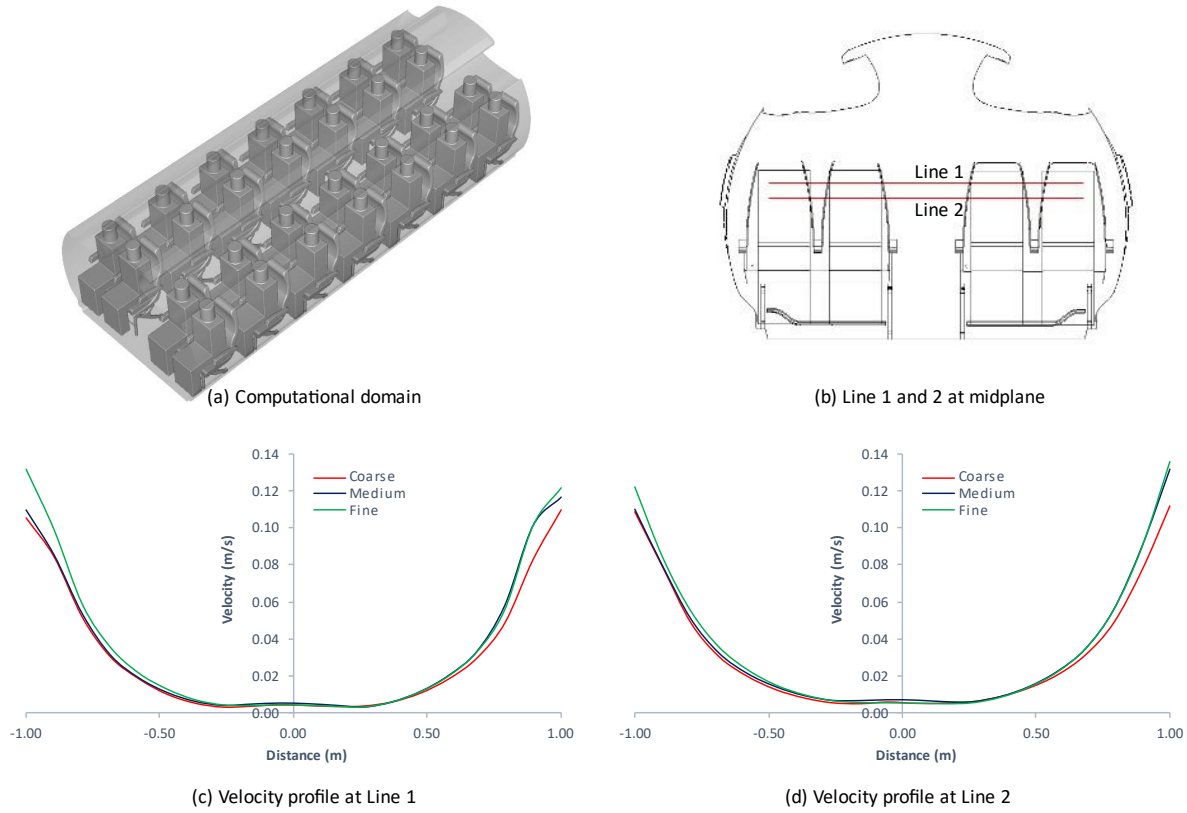

(a) Computational domain

(b) Line 1 and 2 at midplane

(c) Velocity profile at Line 1

(d) Velocity profile at Line 2

Figure 3.3: Velocity profile comparison for different grid sizes

3.8. Discretization of the Computational Domain

3.8.1. Escalator

Hexahedral and tetrahedral were mainly used for meshing of the computational domain. The tetrahedral mesh was applied near the man and the steps of the escalators. The total number of cells and nodes were 1957879 and 690198, respectively. The maximum size of the grid was 0.06 *m*. The maximum grid sizes for local mesh refinement near the human body and steps were 0.03 *m* and 0.04 *m*, respectively. The inflation layer was used on both steps and the man skin's boundary wall.

Several statistics, such as maximum skewness, orthogonal quality, aspect ratio, and Jacobian ratio can aid in determining the quality of a mesh. The essential statistic, however, is skewness. The quality of the mesh was ensured by keeping the skewness within an acceptable limit. Figure 3.2 demonstrates the cross-sectional view of the mesh.

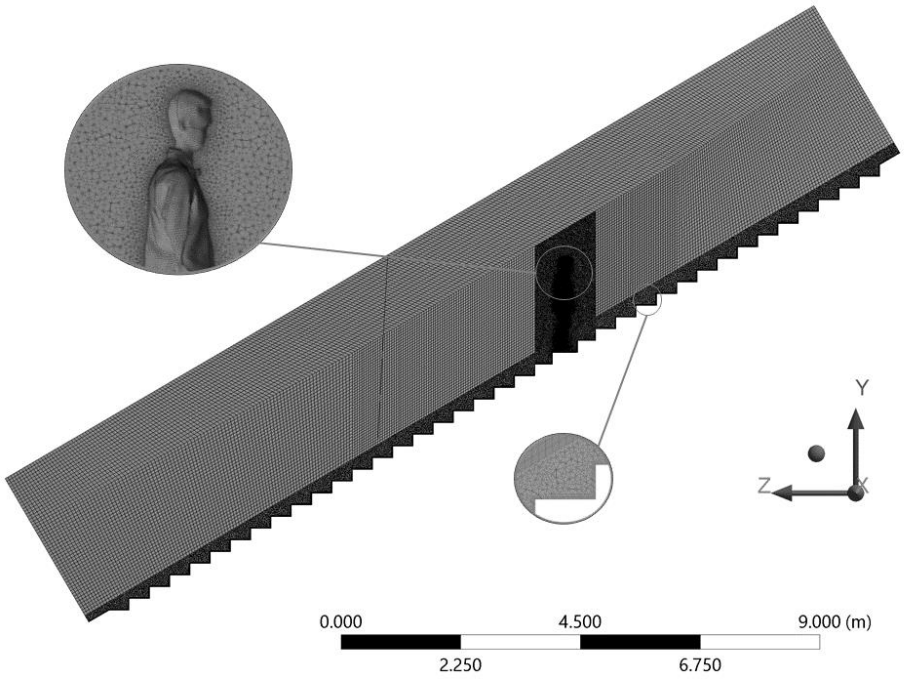

Figure 3.4: Cross-sectional view of the escalator mesh

3.8.2. Aircraft Cabin

Tetrahedral was mainly used for meshing of the computational domain. The total number of elements and nodes were 23622850 and 4680827 respectively. A 50 *mm* grid size with 4.68 million cells was used for meshing. The grid size was 2 *mm* near the inlet waterfall, 3 *mm* near the inlet chimney, 5 *mm* near the wall chimney, and 10 *mm* near the outlet in the MV configuration. The same cell size was also used for the DV configuration.

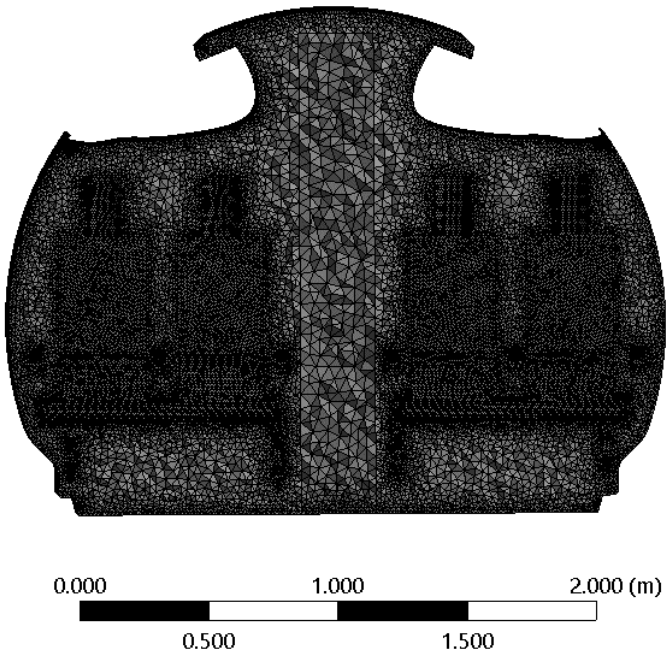

Figure 3.5: Cross-sectional view of the aircraft cabin mesh

3.8.3. The Skewness of the Computational Domain

The difference between the shape of a meshed cell and the equivalent volume of the equilateral cell is known as skewness. The equilateral cell is identified by the value zero. The skewness should be less than 0.95 for a decent solution. However, obtaining excellent skewness for a complex geometry is difficult.

Escalator

The average and maximum skewness of the mesh in this investigation were 0.246 and 0.924, respectively. The shape of man is much more complex. Therefore, this value is adequate to produce a satisfactory solution. The standard deviation was 0.13015. The number of mesh elements for certain skewness values is demonstrated in Figure **3.6**.

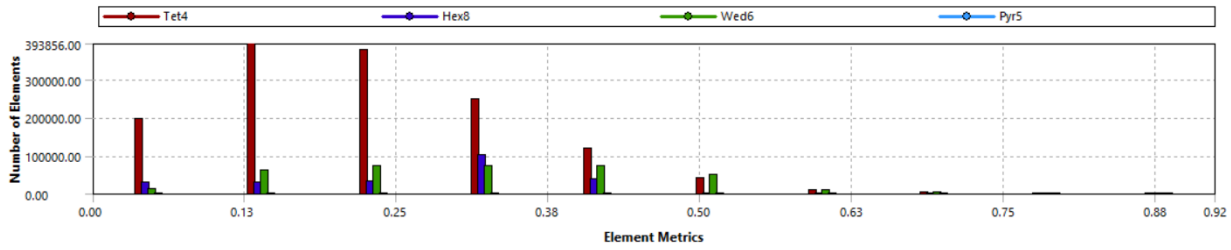

Figure 3.6: Skewness value for the escalator mesh

Aircraft Cabin

The average and maximum skewness of the mesh in this investigation were 1.9×10^{-11} and 0.849, respectively. The standard deviation was 0.1203. The number of mesh elements for certain skewness values is demonstrated in Figure **3.7**.

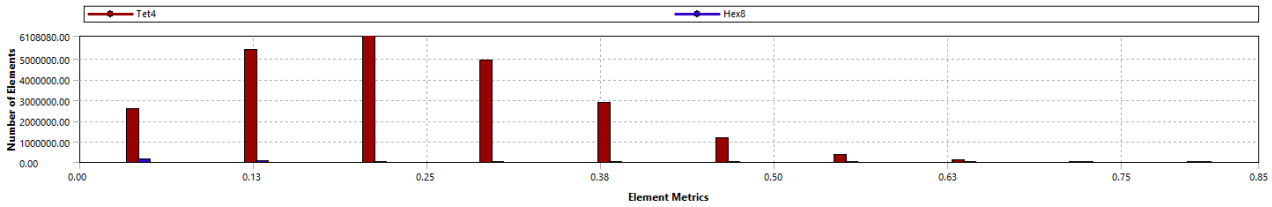

Figure 3.7: Skewness value for the aircraft cabin mesh

3.9. Boundary Conditions

3.9.1. Escalator

The operating pressure was 101325 *Pa* for all cases. The ambient temperature, relative humidity (RH), and velocity of the escalator were kept according to Table 3.5 for different cases.

In warm tropical weather, relative humidity levels typically range from 60% to 90%. In commercial buildings in warm weather, the relative humidity is typically maintained at a comfortable level for occupants, which is generally between 30% to 60%. Therefore, the humidity level was selected accordingly for the warm weather climate. The mass fraction of water vapor, O_2, and N_2 was applied according to Table 3.5. The escalator steps and man skin were set to trap for the droplets of cough. The sides of the computational domain were set to escape for the droplets. The no-slip condition was applied to the steps and human body. The left, right, and top sides of the computational domain were assigned the free slip condition. The turbulent intensity and turbulent viscosity ratio were set to 5% and 10, respectively.

Table 3.5. Ambient temperature, RH, and escalator velocity for different cases

Ambient temperature (°*C*)	**RH (%)**	**Velocity of escalator (*m/s*)**
25	54-84	0.4-0.7

Table 3.6. Mass fraction of water vapor, O_2, and N_2 at different temperatures and ambient relative humidities

Ambient temperature (°C)	**RH (%)**	**mass fraction**		
		water vapor	**O_2**	**N_2**
25	54	0.01071	0.22754	0.76175
25	56	0.01097	0.22748	0.76156
25	58	0.01136	0.22739	0.76125
25	60	0.01176	0.22730	0.76095
25	62	0.01215	0.22721	0.76064
25	64	0.01271	0.22708	0.76021
25	66	0.01294	0.22702	0.76004
25	68	0.01334	0.22693	0.75973
25	70	0.01373	0.22684	0.75943
25	72	0.01413	0.22675	0.75912

25	74	0.01472	0.22662	0.75867
25	76	0.01492	0.22657	0.75851
25	78	0.01532	0.22648	0.75821
25	80	0.01571	0.22639	0.75790
25	82	0.01611	0.22630	0.75760
25	84	0.01673	0.22615	0.75712

3.9.2. Aircraft Cabin

Fresh air enters the cabin through the chimney and waterfall near the ceiling and exits through the nearby floor outlet in MV. For the DV, fresh air enters the cabin through the inlets near the floor and exits through outlets near the ceiling area. In the case of the DV, fresh air enters the cabin through the inlets near the floor and leaves through outlets close to the ceiling. Fresh air was delivered at 9.5 *L/s* per person. The data for relative humidity (RH) levels of 15% and 20% indicated that lower humidity did not affect Heat Removal Efficiency (HRE). The aircraft cabin wall, ceiling, floor, and passenger body all had a "trap" boundary condition, whereas particles escaped through outlets. The commercial aircraft maintain a relative humidity between 15 and 30%. Therefore, relative humidity 30% was selected for this study considering passenger comfort level. Maintaining lower humidity helps to protect the aircraft cabin structure from corrosion and different damages. High humidity can speed up the corrosion of metal components in the aircraft that causes potential safety issues and increased maintenance costs.

Table 3.7. Parameters of the simulations

Parameters	**Value**
Ventilation per person	9.5 *L/s*
Fresh air temperature	293.15 *K*
Ceiling temperature	295.15 *K*
Floor temperature	296.15 *K*
Wall temperature	295.15 *K*
Manikin body temperature	309.82 *K*
Seat	adiabatic

3.9.3. Injection

Particles of 1-200 μm diameters can be injected using standard Rosin-Rammler distribution. The cough droplets were injected for 0.5 s with a Rosin-Rammler diameter distribution. The injection was cone-type with a 30-degree cone angle. The minimum, maximum, and mean diameters were 1 μm, 100 μm, and 10 μm, respectively. The velocity of the expelled cough droplets was set to 12 m/s. The flow rate was 5.24×10^{-8} kg/s. Droplet temperature was 309 K same as human body temperature. The evaporating species was water liquid. The density of droplets was 1000 kg/m^3. The volatile component fraction was set to 90%.

3.10. Methods of Solution

ANSYS Fluent (2020) was used to solve the governing equations of the model under transient conditions. The modeling of the cough aerosol in the escalator was performed based on the Euler-Lagrange approach multiphase model [107, 108]. The first phase of the flow was air while the cough droplets were the second phase. Both the momentum and pressure-based continuity equations were used simultaneously with the Coupled Pressure-Velocity Coupling algorithm.

3.10.1. Coupling Between Continuous Phase and Discrete phase

The diameter of the droplets is reduced by the interaction with the continuous phase. The continuous phase and discrete phase were coupled to include mass, momentum, and heat exchange between these two phases.

3.10.2. Continuous Phase Solver

An implicit pressure-based solver was used. Both the momentum and pressure-based continuity equations simultaneously use the Coupled Pressure-Velocity Coupling algorithm. If the larger time steps are used, the algorithm should be Coupled Pressure-Velocity Coupling. The least-squares cell-based gradient was used to calculate the gradients. The least-squares gradient has a

lower computational cost than the node-based gradient. The accuracy of the least-squares gradient method is nearly similar to that of a node-based gradient for unstructured distorted mesh.

PREssure STaggering Option (PRESTO!) was used as a discretization scheme for pressure [109]. It provides more accurate results by avoiding interpolation errors. But the computation cost of PRESTO! is slightly higher. This technique is more suitable for issues involving strong body forces, such as swirl. Second-order upwind spatial discretization was used for momentum, energy, phase 1 H_2O, and O_2, while the first-order upwind discretization was used for turbulent kinetic energy and dissipation rate. The transient formulation was selected as second-order implicit.

3.10.3.Discrete Phase Solver

Injection of cough droplets was set as a discrete phase. Interaction with continuous phase was enabled. Droplets were tracked as unsteady particle tracking with fluid flow time step. The 'implicit' and 'trapezoidal' schemes were chosen. Thermophoretic force and Saffman lift force were included. On the other hand, virtual mass force, pressure gradient force, collision, breakup, and Brownian motion were neglected. Two-way turbulence force coupling was also considered.

3.11. Multi-Objective Optimization Using Genetic Algorithm

The genetic algorithm (GA) is a heuristic optimization technique based on natural selection that can be used to solve unconstrained and constrained problems. There is no need for an initial solution with heuristic optimization algorithms such as GA. GA can address both continuous and discrete variables as there is no derivative term. The ‘gamultiobj’ function was used to implement the multi-objective optimization in MATLAB.

3.11.1.Design Variables

The key design variables used in the model are enlisted in the following table with lower and upper bounds. The design variables are limited to escalator velocity and relative humidity to reduce the number of simulations for the dataset.

Table 3.8. List of design variables

variable	symbol	lower and upper bound	unit
Escalator velocity	v	$0.4 \leq v \leq 0.7$	*m/s*
Relative humidity	RH	$54\% \leq h \leq 84\%$	-

3.11.2.Multi-Objective Optimization

For multi-optimization objectives, the aerosol concentration (J1) was selected as an objective in addition to the droplet penetration length (J2). The objectives are minimization of aerosol concentration and droplet penetration length.

3.11.3.Model Validation

The algorithm codes are validated using the following test functions. The first function is the unimodal Ackley Function [124].

$$f(x) = -200e^{-0.2\sqrt{x_1^2+x_2^2}} \tag{3.55}$$

$$-32 \leq x \leq 32$$

The second function is the Bird Function [124].

$$f(x) = -\sin(x_1)\, e^{(1-\cos(x_2))^2} + \cos(x_2)\, e^{(1-\sin(x_1))^2} + (x_1 - x_2)^2 \tag{3.56}$$

$$-2\pi \leq x \leq 2\pi$$

The comparison of the derived data from GA and SQP is given in the following table. Bird Function (multimodal) has two local minima. GA cannot find these two local minima at the same time. After some random runs, the second local minima is found in GA. SQP is dependent on the initial guess to find the local minima of the Bird function. But it cannot find the second local minima.

Table 3.9. Test function and optimization algorithm code

Function	**Global minimum (x*)**	**f(x∗)**	**GA**	**SQP**
Ackley Function (unimodal)	(0, 0)	−200	x*(0, 0) f(x∗) = -200	x*(0, 0) f(x∗) = -200
Bird Function (multimodal)	(4.70104, 3.15294), (−1.58214, −3.13024)	−106.764537	x*(-1.59, -3.123), (4.69, 3.16) f(x∗) = -106.787	initial guess (-1 -3) x*(-1.59, -3.123), f(x∗) = -106.787

3.11.4.Sensitivity Analysis

Upward Moving Escalator (UME)

There are two design variables in the objective function: escalator operational speed & RH. The gradient of aerosol concentration and RH are calculated from each single objective. The gradients of the single objective concentration function in UME are as follows:

$$\nabla J^* = \begin{bmatrix} \frac{\partial J}{\partial v} \\ \frac{\partial J}{\partial RH} \end{bmatrix} = \begin{bmatrix} -4.3503e-10 \\ 4.5550e-12 \end{bmatrix}$$

The gradients are normalized to understand the effect on the objective function. The normalized sensitivity of the objective function with respect to design variables is derived as follows:

$$\nabla \bar{J}^* = \begin{bmatrix} \frac{\partial J}{\partial v}\frac{v}{J^*} \\ \frac{\partial J}{\partial RH}\frac{RH}{J^*} \end{bmatrix} = \begin{bmatrix} -1.2455 \\ 1.0060 \end{bmatrix}$$

The escalator velocity demonstrates higher sensitivity than RH. One percent of the increase in escalator velocity causes a 1.25% decrease in the aerosol concentration. The increase in one percent RH at the optimal point incurs a 1% increase in the concentration.

The gradients and normalized sensitivity of single objective droplet penetration length function in the UME are as follows:

$$\nabla J^* = \begin{bmatrix} \frac{\partial J}{\partial v} \\ \frac{\partial J}{\partial RH} \end{bmatrix} = \begin{bmatrix} 8.0434 \\ 3.7000e-08 \end{bmatrix}$$

$$\nabla \bar{J}^* = \begin{bmatrix} \frac{\partial J}{\partial v}\frac{v}{J^*} \\ \frac{\partial J}{\partial RH}\frac{RH}{J^*} \end{bmatrix} = \begin{bmatrix} 1.0347 \\ 8.3060e-07 \end{bmatrix}$$

The above sensitivity analysis shows that one percent of the increase in the escalator causes a 1.03% increase in the penetration length.

Downward Moving Escalator (DME)

The gradients and normalized sensitivity of single objective aerosol concentration function in the DME are as follows:

$$\nabla J^* = \begin{bmatrix} \frac{\partial J}{\partial v} \\ \frac{\partial J}{\partial RH} \end{bmatrix} = \begin{bmatrix} -2.0580e-10 \\ 4.2817e-12 \end{bmatrix}$$

$$\nabla \bar{J}^* = \begin{bmatrix} \frac{\partial J}{\partial v}\frac{v}{J^*} \\ \frac{\partial J}{\partial RH}\frac{RH}{J^*} \end{bmatrix} = \begin{bmatrix} -0.4112 \\ 0.6600 \end{bmatrix}$$

One percent of the increase in escalator velocity causes a 0.41% decrease in the aerosol concentration. The increase in one percent RH at the optimal point incurs a 0.66% increase in the concentration.

The gradients and normalized sensitivity of single objective droplet penetration length function in the UME are as follows:

$$\nabla J^* = \begin{bmatrix} \frac{\partial J}{\partial v} \\ \frac{\partial J}{\partial RH} \end{bmatrix} = \begin{bmatrix} 2.2856 \\ -0.0026 \end{bmatrix}$$

$$\nabla \bar{J}^* = \begin{bmatrix} \frac{\partial J}{\partial v}\frac{v}{J^*} \\ \frac{\partial J}{\partial RH}\frac{RH}{J^*} \end{bmatrix} = \begin{bmatrix} 0.5285 \\ -0.1262 \end{bmatrix}$$

One percent increase in escalator velocity causes a 0.53% increase in droplet penetration length in DME.

3.11.5. Genetic Algorithm (GA) Tuning

GA tuning is crucial to achieving the quality of the design solution. Multiple investigations were carried out using different population sizes, mutation functions, and crossover fractions for tuning GA. The population size varied between 200 to 400. The crossover fraction varied between 0.3 to 0.9. Constrain-dependent, Gaussian, and uniform functions were investigated for mutation tuning. Crossover functions of scattered, single point, two points, and intermediate were investigated.

Finally, the population size was selected as 400. The Tournament function with a size of 2 was used to accomplish the selection procedure. The crossover operation was performed using an intermediate function keeping a crossover fraction of 0.8. The constraint-dependent function was used for mutation operation. The direction of migration was chosen forward with a fraction of 0.2 and 20 intervals. The GA termination conditions were 600 generations, function, and constraint tolerance of 1e-4 and 1e-3.

Chapter 4
Results & Discussion: Upward Moving Escalator

Investigations were conducted to better understand the transmission of cough droplets and their nuclei while riding an upward-moving escalator. The investigations aimed to look for the dynamics of cough droplet transmission and their nuclei in a unique scenario, while riding an upward-moving escalator.

4.1. Airflow Dynamics

The fate of aerosol transport is determined by some properties of the phase-1 airflow dynamics such as velocity magnitude, velocity vector, vorticity, and turbulent kinetic energy. The discrete phase of the cough aerosol is influenced by the path lines of phase-1 (airflow) as soon as the injection of droplets is stopped.

4.1.1. Velocity Contour

The effect of velocity and RH on the velocity contour at the midplane is illustrated in Figure **4.1** and Figure **4.2** after the cough injection. Two different escalator velocities of 0.4 *m/s* and 0.6 *m/s* at 54% RH were chosen to compare the effect of the escalator's operational speed. To study the effect of the RH, the escalator velocity was held at 0.4 *m/s* with a varying RH of 54% and 84%. The no-slip condition was used on the boundary of escalator steps and the human body. In comparison to the rest of the domain, the velocity between the steps is much lower. For all cases, air recirculates between two consecutive steps, as shown in Figure **4.3**. Therefore, cough aerosol also recirculates with air whenever it reaches this zone. The maximum velocity is located near the top of the human head for all velocities and RHs as shown in Figure **4.1** and Figure **4.2**. The wake region increases as the escalator velocity increases. The local velocity and the wake region remain almost the same whenever the RH increases. This was found the same for 40% RH also. Because of adverse pressure gradient in association with flow separation, eddies form in the downstream side wake region at the back end of the torso and legs. The fluid inside the downstream side begins to move backward and in a circular motion, resulting in the formation of eddies. The movement of fluid particles is extremely chaotic at this location. These eddies eventually leave the vicinity of

man and float away with the main airflow. In general, observing the wake flow behind the passenger reveals that the body of the passenger acts as a bluff-body.

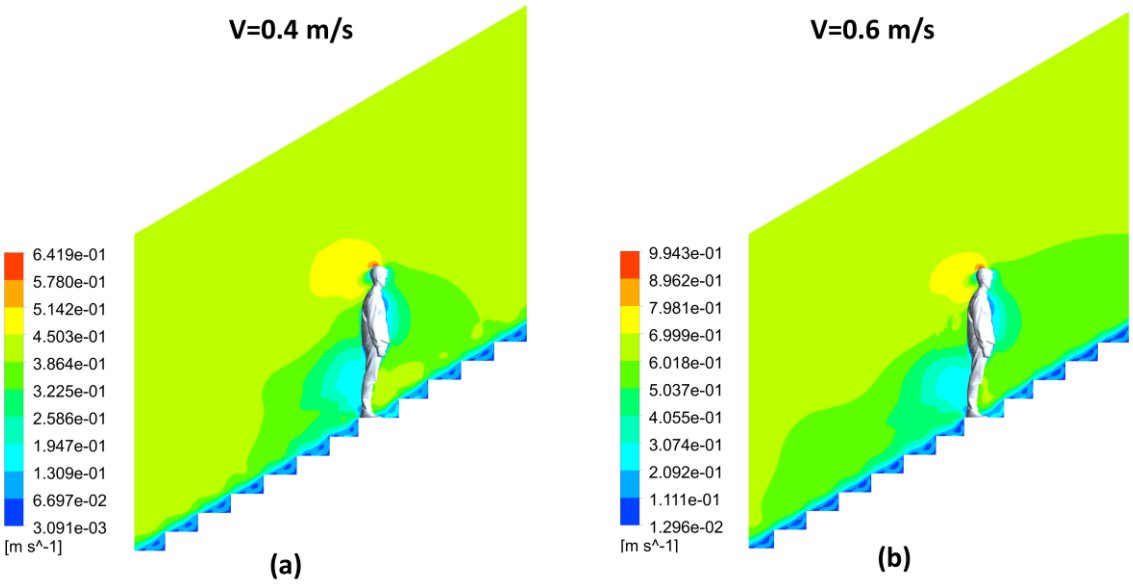

Figure 4.1. Velocity contours for different escalator velocities in upward-moving escalator (at midplane, velocity effect) a) v=0.4 m/s, b) v=0.6 m/s

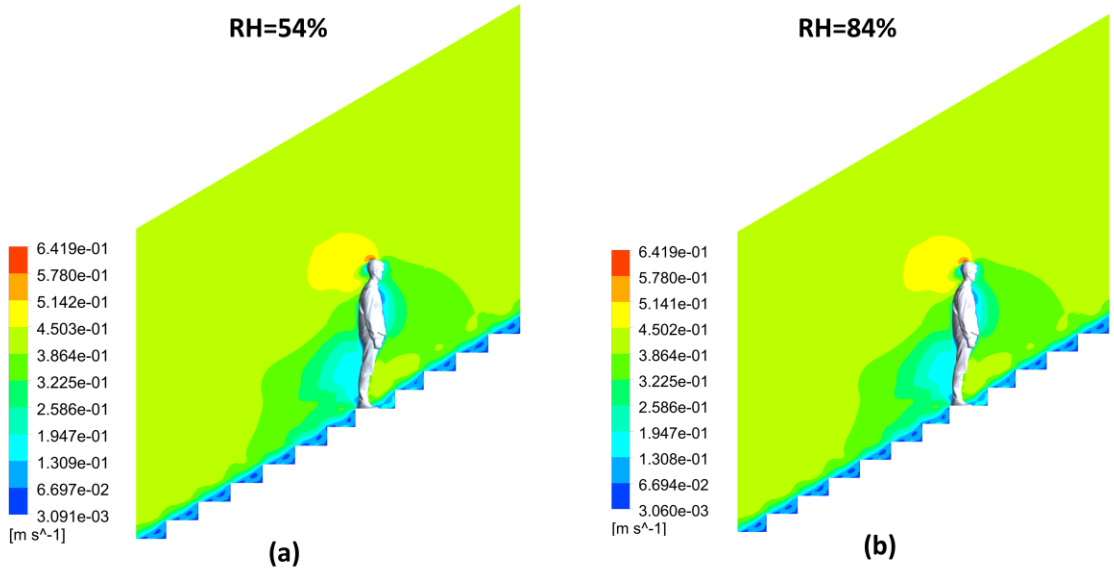

Figure 4.2. Velocity contours for different escalator velocities in upward-moving escalator (at midplane, RH effect) a) RH=54%, b) RH=84%

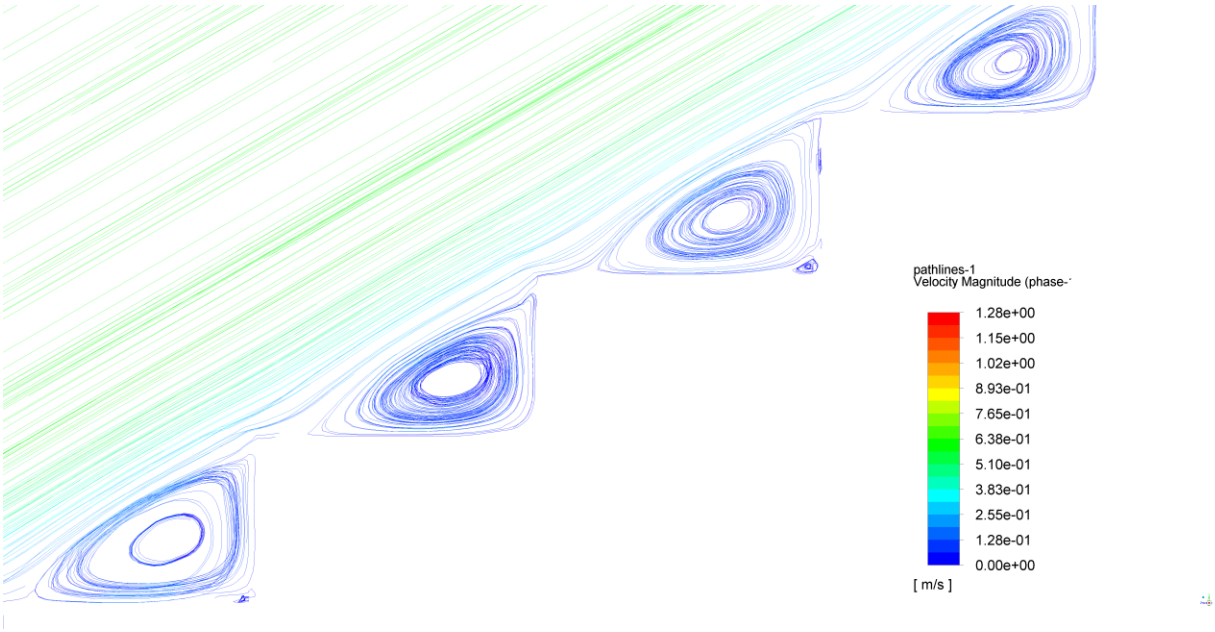

Figure 4.3. Circulation between two consecutive steps

4.1.2. Turbulent Kinetic Energy

The mean kinetic energy per unit mass associated with eddies in turbulent flow is referred to as turbulence kinetic energy, whereas it is defined physically by root-mean-square velocity fluctuations. As the fluid flow velocity increases, eddies become more numerous. The larger the eddies, the greater their energy content. It is dissipated by viscous forces at the Kolmogorov scale as it travels down the turbulence energy cascade. Kinetic energy is transferred from large eddies to small eddies during this process until it is dissipated. In turbulent flow, the smallest scales are known as Kolmogorov microscales. The Kolmogorov scale is dominated by viscosity, and the turbulent kinetic energy is dissipated as heat.

Because of low pressure in association with flow separation, eddies form in the downstream side wake region at the back end of the torso and legs. The fluid inside the downstream side begins to move backward and in circles, resulting in the formation of eddies. The movement of fluid particles is extremely chaotic at this location. These eddies eventually leave the vicinity of man and float away with the main airflow.

The effect of escalator velocity on the turbulent kinetic energy contour at the midplane is illustrated in Figure **4.4**. The variation of turbulent kinetic energy is more significant at the back end of the neck, torso, and legs. It is also observed that higher kinetic energy is found at the regions of the step's outer sharp edge than in the inner regions of consecutive steps. As expected, the extent and zone of higher turbulent kinetic energy expand with increasing escalator velocity, and an escalator velocity of 0.6 *m/s* has a higher turbulence intensity than 0.4 *m/s*. The extent of higher turbulent kinetic energy is found up to 3rd step behind the passenger, whereas it was observed up to 5th step for 0.6 *m/s* escalator velocity. It is revealed that the maximum turbulent kinetic energy for 0.6 *m/s* is approximately 1.9 times higher than 0.4 *m/s* operational speed. Overall, the turbulence scale rises as the escalator speed rises. Figure 4.5 depicts the variation of turbulent kinetic energy at the midplane for two different ambient relative humidities of 54% and 84%. There are no noticeable differences for both 54% and 84% RH. The peak for 54% and 84% RHs is observed on the backside of the neck. This was found the same for 40% RH also.

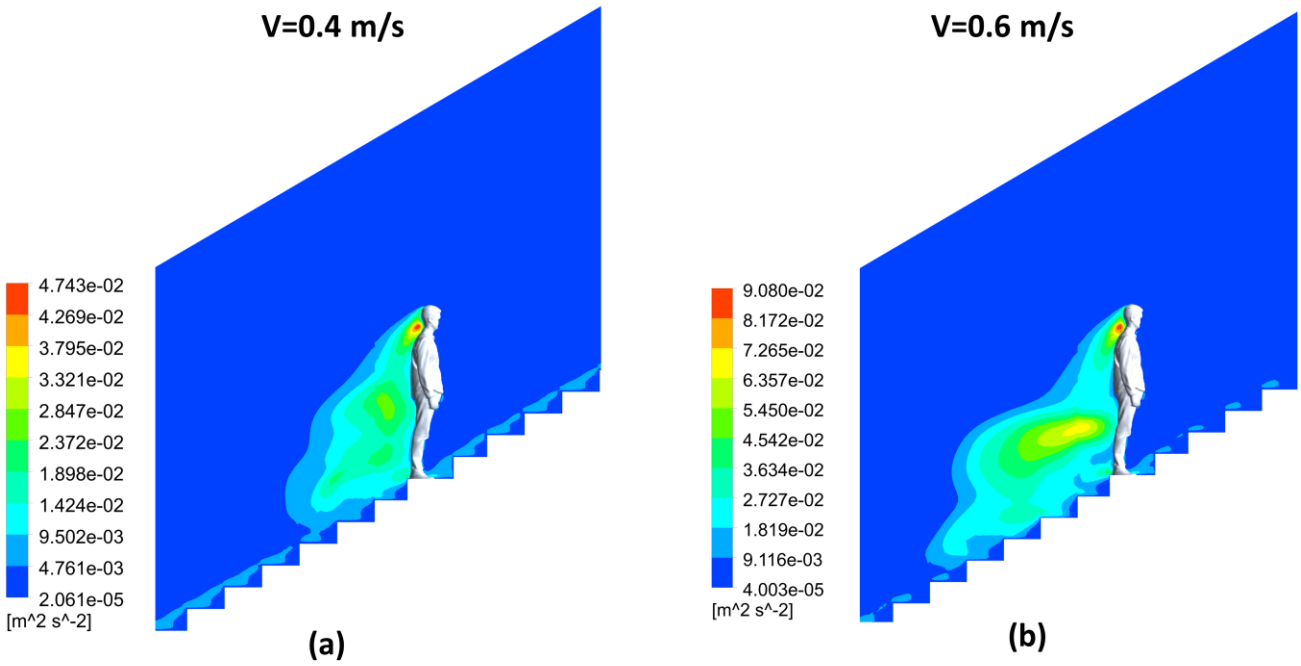

Figure 4.4. Turbulent kinetic energy for different escalator velocities in upward-moving escalator (at midplane, velocity effect) a) v=0.4 m/s, b) v=0.6 m/s

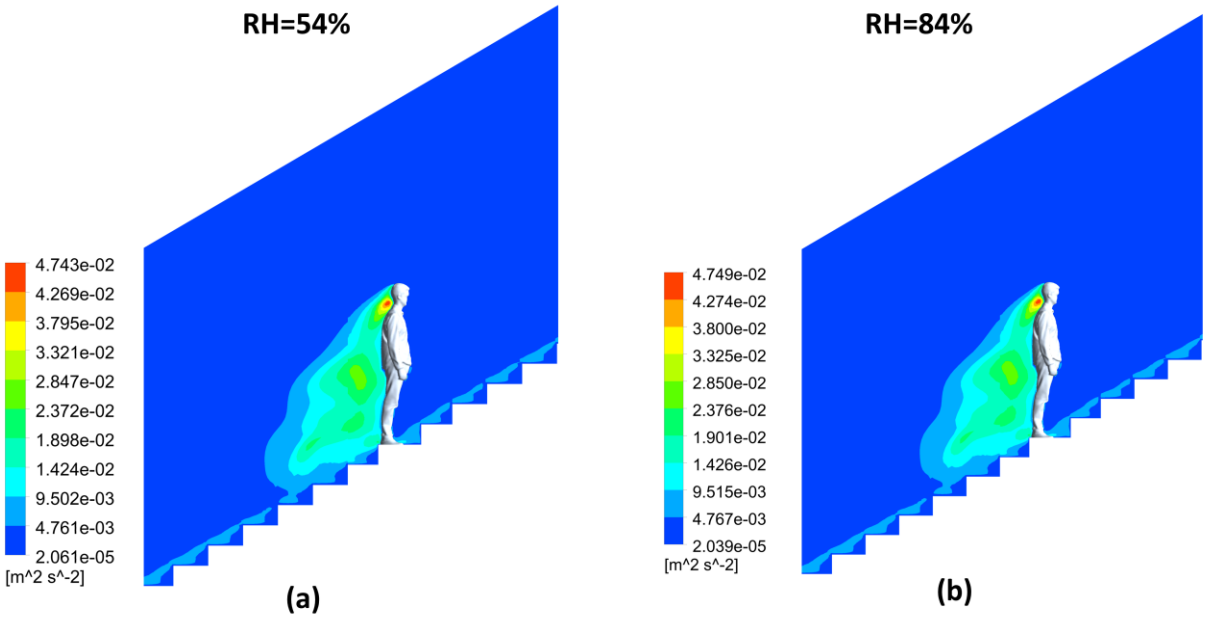

Figure 4.5. Turbulent kinetic energy for different escalator velocities in upward-moving escalator (at midplane, RH effect) a) RH=54%, b) RH=84%

4.2. Cough Droplets Penetration

The penetration of cough droplets in an upward-moving escalator with velocities of 0.4 *m/s*, 0.5 *m/s*, 0.6 *m/s*, and 0.7 *m/s* is demonstrated in Figure **4.6**(a) at 54% RH. Figure 4.6(b) illustrates the effect of RH on droplet penetration length for the RH of 54%, 64%, 74%, and 84% at 0.4 *m/s* operational speed. Penetration length of droplets increases for each case over the flow time. There is no noticeable difference observed up to 0.14 *s* in Figure **4.6**(a). After 0.14 s, higher penetration of cough droplets is observed for higher escalator operational speeds. The penetration length of the cough droplet for 0.7 *m/s* is 53.88% higher than the operational speed of 0.4 *m/s* at 5 *s*. In general, the higher velocity of the escalator is associated with higher droplet penetration.

Figure 4.6(b) depicts an inverse relationship between droplet penetration length and RH. But after 4 *s*, the penetration length of 84% RH is higher than 64% and 74% RH. Droplet penetration length is almost identical up to 0.8 *s* for all RH. Because of the continuous movement of the escalator, the length of droplet penetration increases with the increase in flow time. At 5 *s*, the penetration length for 74% RH is 7.76% less than 54% RH.

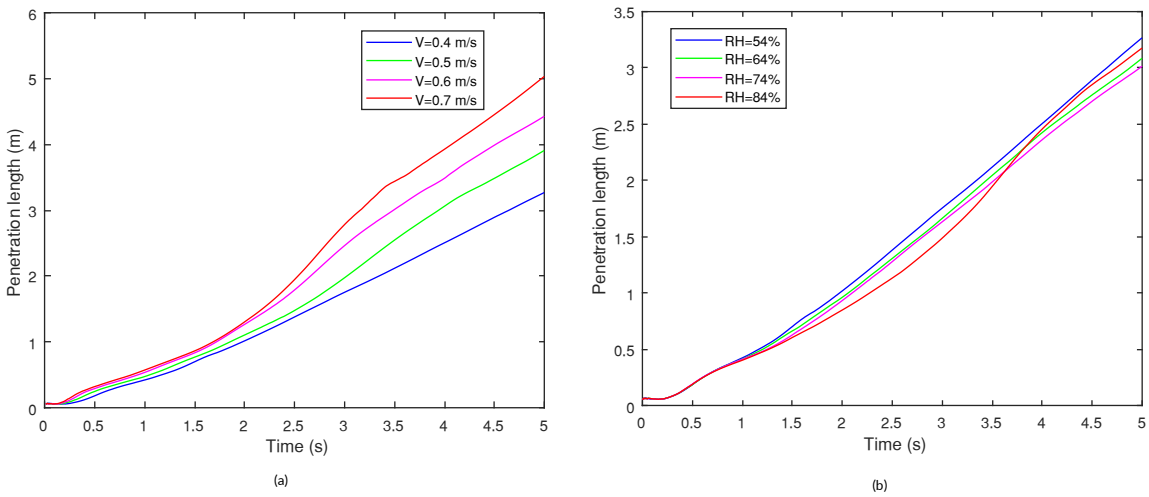

Figure 4.6. Penetration length for different (a) escalator velocities (b) RHs in upward-moving escalator

Droplet evaporation influencing influences the acting forces and complicates the motion of droplets by reducing droplet size during droplet in its trajectory. Investigations were carried out to provide a clear physical demonstration of droplets' transport with different escalator velocities and ambient relative humidity to study the influence of droplet evaporation. Figure **4.7** depicts the comparison of droplets' dispersion for 0.4 *m/s* (Figure **4.7**(a, c, e, g, i)) and 0.6 *m/s* (Figure **4.7**(b, d, f, h, j)) operational speed at 54% RH. The difference in the trajectories of cough droplets is almost negligible for escalator velocity of 0.4 *m/s* and 0.6 *m/s* at 0.2 *s*. At 0.5 *s*, the escalator velocity begins to affect the traveling distance. Smaller droplets are seen to move first along the upper side of the shoulders of the man because of their lightweight. The droplets enter the wake region at 1 *s* flow time behind the torso. Later, the cough aerosol enters the recirculation zone near the steps. After a few seconds, at 5 *s*, the droplets recirculate with the air between two consecutive steps. Few droplets get trapped on the steps during the recirculation, while the remaining slowly move to the back steps. Only the lower portion of the human body (other passengers), such as the waist and legs, is contaminated by these droplets, behind the infected person. Most of the droplets of smaller size are found behind the immediate backside of the human body at 5 *s* flow time. The maximum and minimum droplet sizes for both escalator velocities are 22.9 μm and 0.464 μm at 5 *s*. For the same amount of time, the cough droplets with lower escalator velocity travel a shorter distance than higher escalator velocity.

The variation of cough droplet trajectories for the ambient relative humidity of 54% (Figure **4.8** (a, c, e, g, i)) and 84% (Figure **4.8**(b, d, f, h, j) at 0.4 *m/s* is demonstrated in Figure **4.8**. The transport of cough droplets is affected by humidity. Figure **4.8** illustrates that higher ambient relative humidity slows the transport process of the cough droplets. Droplets with lower relative humidity reach the steps of the escalator earlier than higher ambient relative humidity. The maximum and minimum droplet sizes for both ambient relative humidities are 22.9 μm and 0.464 μm at 5 *s*. The trajectories of almost all droplets are near the escalator steps as these get trapped in the recirculation zone. Dispersion of the cough droplets for RH of 54% is found in a wider zone than RH of 84% at the same flow time. Most of the larger droplets are found in front of the trajectories in 54% RH whereas a few larger droplets are still dispersed in the wake zone behind the torso.

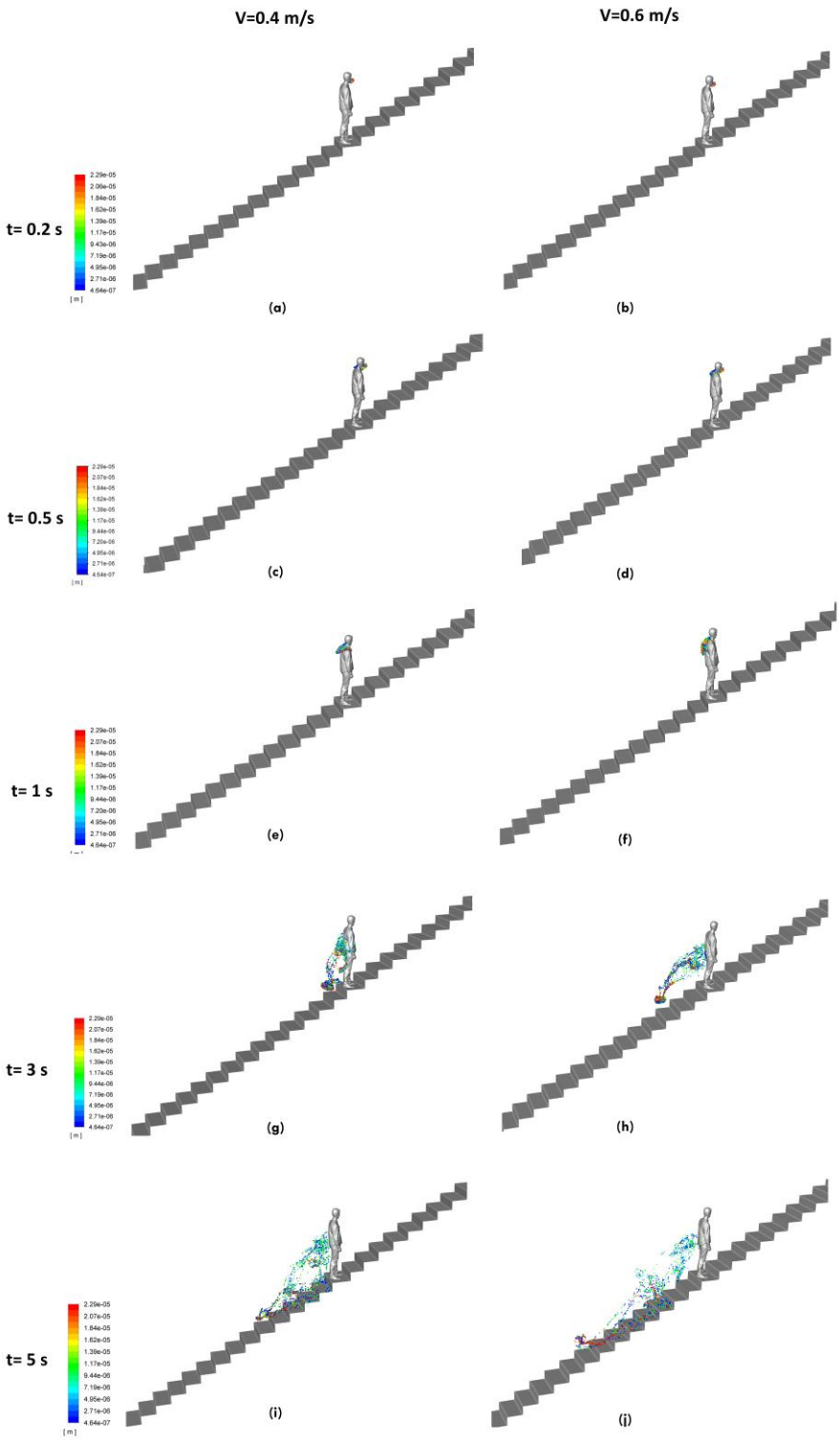

Figure 4.7. Cough droplet trajectories for different escalator velocities at different times in upward-moving escalator (velocity effect)

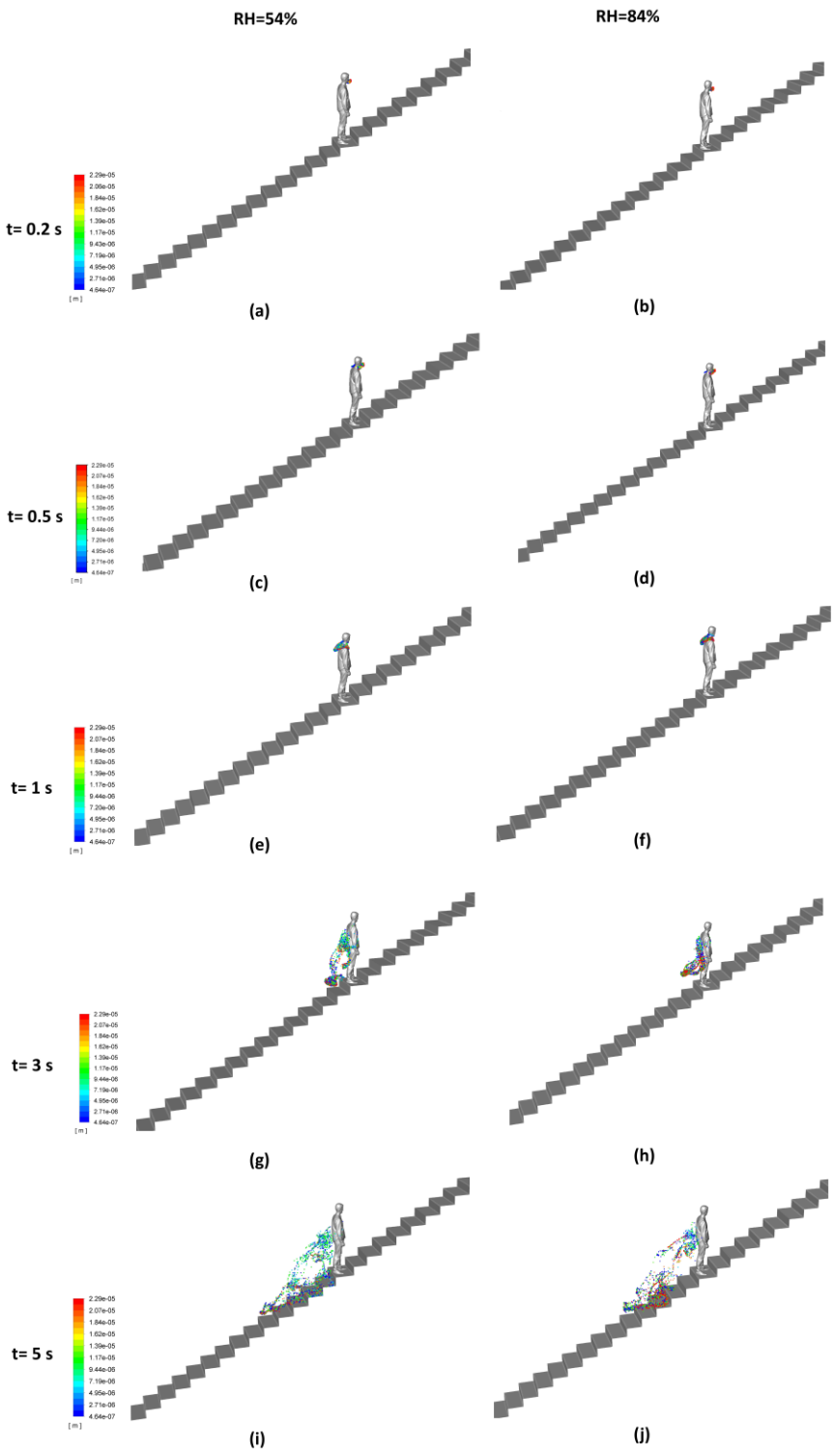

Figure 4.8. Cough droplet trajectories for different escalator velocities at different times in upward-moving escalator (RH effect)

Figure 4.9 traces the droplets along with path lines of air for escalator velocities of 0.4 *m/s* and 0.6 *m/s* at 5 *s* flow time. Droplets recirculation with air between two steps starts from the first step behind the human body for an escalator velocity of 0.4 *m/s*, whereas it starts for 0.6 *m/s* escalator velocity from the third step. At t= 5 *s*, the extent of circulation zone for 0.6 *m/s* escalator is found higher than 0.4 ms^{-1} escalator. The horizontal distance for 0.4 *m/s* and 0.6 *m/s* escalator velocities traveled by the cough droplets is approximately 2.1 *m* and 3.2 *m* from the body of the infected person. As a whole, cough droplet dispersion in the horizontal direction increases as operational speed increases.

Figure 4.10 depicts the droplets trace and path lines of fluid particles (air) for ambient relative humidity levels of 54 and 84 percent at a flow time of 5 seconds. Strong circulation of air and cough droplets is seen between steps with low-velocity magnitude. A high level of chaos is present behind the torso. Recirculation regions develop between the steps. Cough droplets enter the circulation zone between the steps at an early flow time for a lower relative humidity of 54%. Droplets recirculation with air between two steps starts from the first step behind the human body for a 54% RH, whereas it starts for 84% RH from the third step. Strong vorticity is found at 3rd step behind the man. The horizontal distance for 54% and 84% RH traveled by the cough droplets is approximately 2.1 *m* from the body of the infected person.

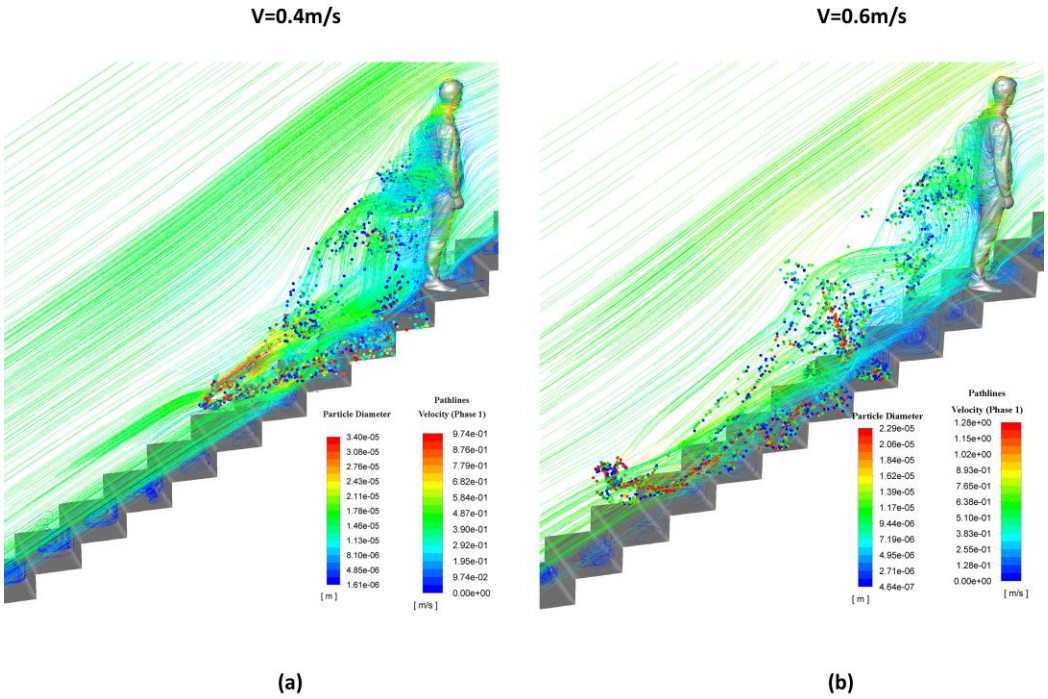

Figure **4.9**. Path lines of phase 1 and cough droplets trace for different escalator velocities in upward-moving escalator (at t= 5 s, RH=54%, velocity effect)

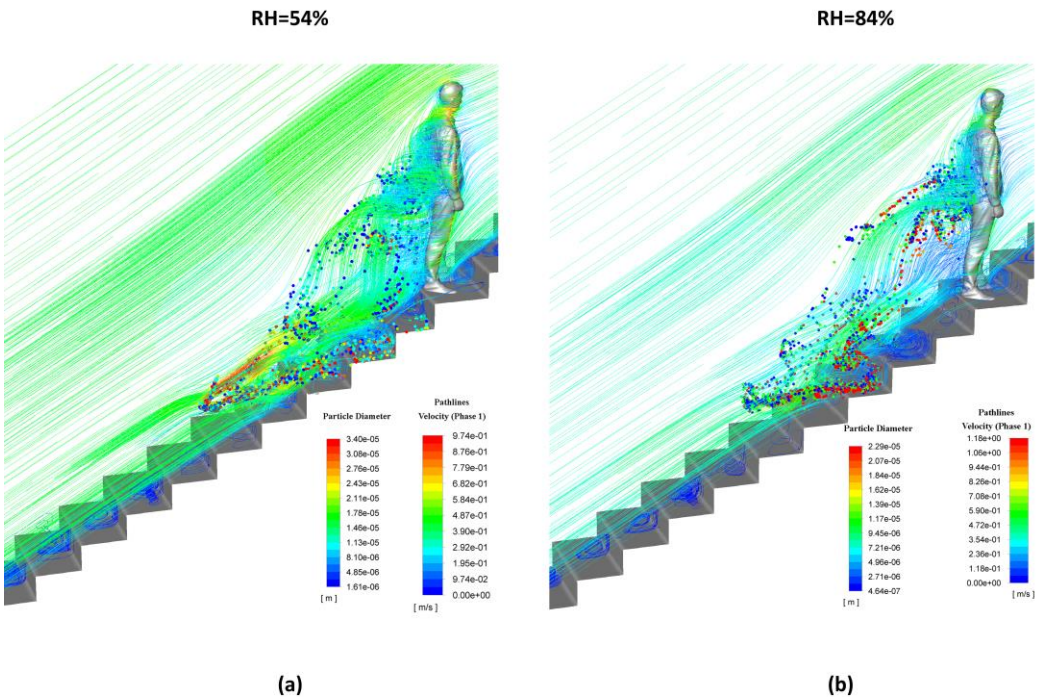

Figure 4.10. Path lines of phase 1 and cough droplets trace for different escalator velocities in upward-moving escalator (at t= 5 s, V=0.4 ms^{-1}, RH effect)

4.3. Evaporation of Droplets

Evaporation is the process by which a liquid is vaporized to gas at temperatures lower than the boiling point. It occurs on the liquid surface. The volatile portion of the cough droplets only evaporates during this process. Droplet evaporation influences the acting forces and complicates the motion of droplets by reducing droplet size during droplet trajectory. Investigations were carried out to provide a clear physical demonstration of droplets transport with different escalator velocities and ambient RH to study the influence of droplet evaporation.

4.3.1. Evaporation Rate

Because of evaporation, the diameter of cough droplets changes continuously, affecting their trajectories, residence time, and dispersion. The effect of escalator operational speed and RH on the evaporation rate are illustrated in Figure **4.11**. The evaporation rate for each case is significantly higher up to 0.5 *s* than the remaining flow time. The kinetic energy of the injected cough droplets is much higher during the injection period of cough droplets. Evaporation proceeds more quickly at higher kinetic energy because of the higher flow rate between the air and the cough droplet. Liquid molecules can easily escape the Knudsen layer, also known as the evaporation layer at higher kinetic energy. The evaporation rate decreases dramatically between 0.5 *s* to 0.7 *s* as soon as the injection of cough droplets is stopped. Higher operational speed and lower RH demonstrate a higher evaporation rate up to 0.5 *s*. No common trend is found after 0.5 *s* when the droplets enter the wake zone.

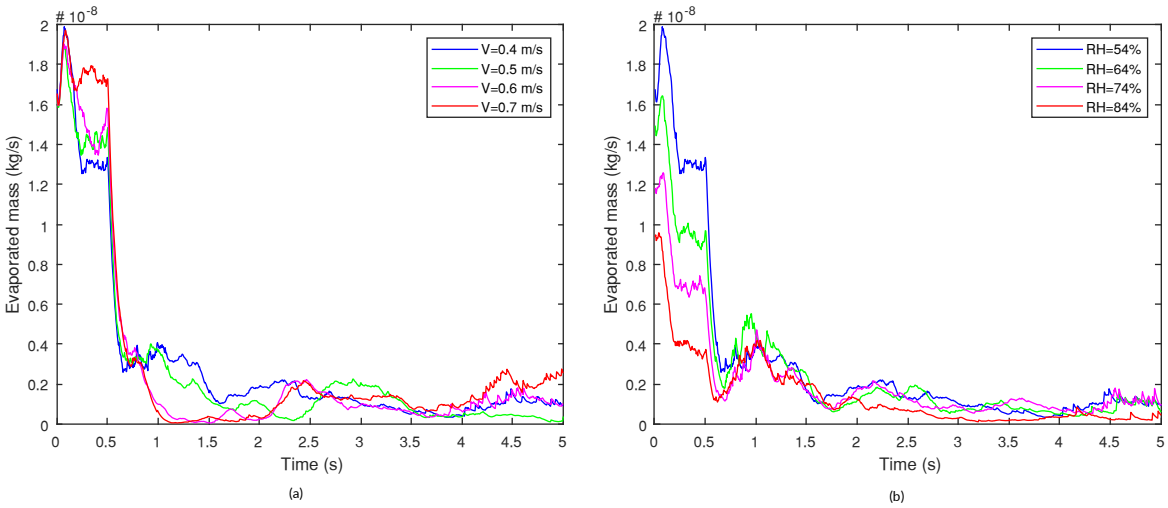

Figure 4.11. Evaporation rate for different (a) escalator velocities, (b) RHs in upward-moving escalator

4.3.2. Average Droplets Diameter

Figures **4.12** (a, b) demonstrates the effect of velocity and RH on the change in the average diameter of droplets over time because of the evaporation and coalescence process. The average diameter of the droplets was calculated arithmetically which is the summation of diameters of all suspended droplets to the total number of the suspended droplets. Initially, the collision among the droplets is higher when the cough droplets are injected. Therefore, the average diameter of cough droplets increases up to 0.02 *s* as the number of droplets decreases because of the coalescence process. Coalescence is the process by which two or more droplets merge into one large droplet. There is no noticeable difference observed up to 0.14 *s* for the velocity and RH effect. But the average diameter reduced drastically up to 0.23 *s* because of a higher evaporation rate. Fluctuations of average diameter are observed between 0.25 *s* and 3.5 *s* flow time due to the higher droplet coalescence. It is observed that the fluctuations are almost negligible from 3.8 *s*. It is seen from the illustrations that the average diameter of the cough droplets is found higher at a higher velocity and RH up to 0.5 *s* and for the rest of the flow, it fluctuates.

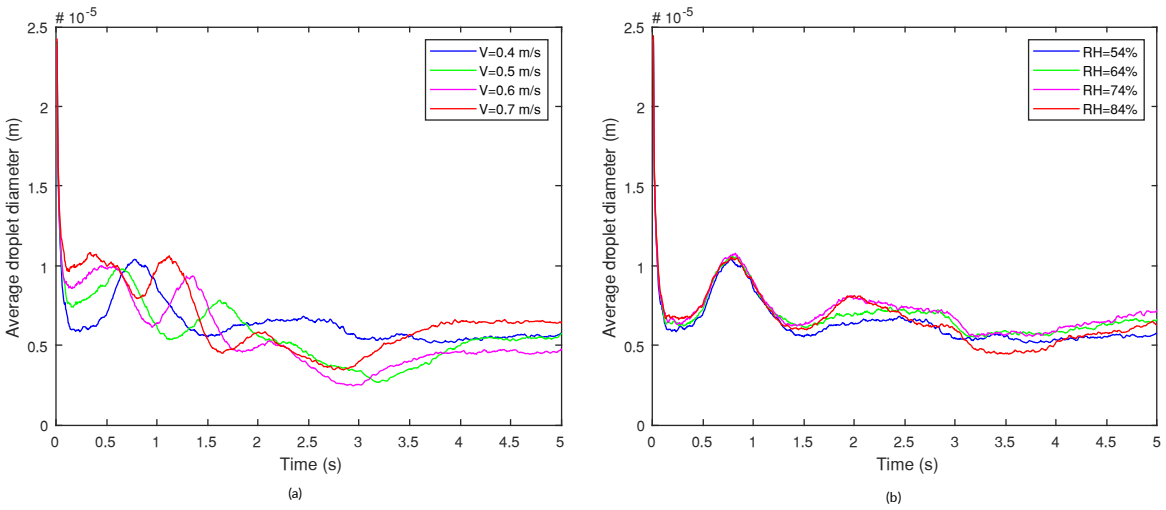

Figure 4.12. Average droplets diameter for different (a) escalator velocities (b) RHs in upward-moving escalator

4.4. Deposition of Droplets

The droplets containing viral particles get deposited on the surfaces (man skin, steps) because of the gravity. Deposition of droplets depends on many factors such as the pattern of airflow, velocity of airflow, RH, the extent of turbulence, properties of liquid, size of droplets, surface texture, surface properties, etc. The effect of escalator velocity and ambient relative humidity on the deposition of cough droplets is studied in this section.

The comparison of droplets deposition on different surfaces (man skin, steps) with escalator velocities of 0.4 ms^{-1}, 0.5 *m/s*, 0.6 *m/s*, and 0.7 *m/s* at 54% RH is demonstrated in Figure **4.13** (a). The cough droplets were deposited on the human skin first because it was the nearest-surface to adhere. The deposition (2.81×10^{-13} kg/m^2) on the man's skin begins at 0.24 *s* for the higher escalator velocity of 0.7 *m/s*, whereas it begins at 0.61 s for the lower escalator velocity of 0.4 *m/s*, which is 1.02×10^{-11} kg/m^2. The deposition of droplets on the human skin is the lowest for escalator velocity of 0.7 *m/s* than other velocities although deposition begins earlier for higher velocity. On the other hand, the deposition on the steps of the escalator begins approximately at 3.25 *s* for 0.7 *m/s*. Higher deposition on the escalator steps is found for higher escalator velocity. At 5 *s*, the deposition on the steps of the escalator for 0.4 ms^{-1}, 0.5 *m/s*, 0.6 *m/s*, and 0.7 *m/s* are

8.75×10^{-12} kg/m^2, 1.29×10^{-11} kg/m^2, 1.6×10^{-11} kg/m^2, and 1.64×10^{-11} kg/m^2 respectively. In general, lower operational speed demonstrates higher deposition on human skin.

Figure 4.13 (b) depicts the deposition of droplets for an ambient relative humidity of 54%, 64%, 74%, and 84% at 0.4 *m/s* operational speed. At 0.4 *m/s*, the lower ambient relative humidity is associated with greater deposition on the human body except for 64% RH. The deposition on the man's skin begins at 0.61 *s*, 0.6 s, 0.67 *s*, and 0.7 *s* for the RH of 54%, 64%, 74%, and 84% respectively while deposition on steps begins at 3.49 *s*, 4.19 *s*, 3.98 *s*, 4.03 *s*, respectively. At 5 *s*, the deposition on the human body for RH of 54%, 64%, 74%, and 84% are 3.09×10^{-10} kg/m^2 and 4.4×10^{-10} kg/m^2, 2.059×10^{-10} kg/m^2, 2.07×10^{-10} kg/m^2 respectively. Except for 64% RH, lower RH results in higher deposition on human skin.

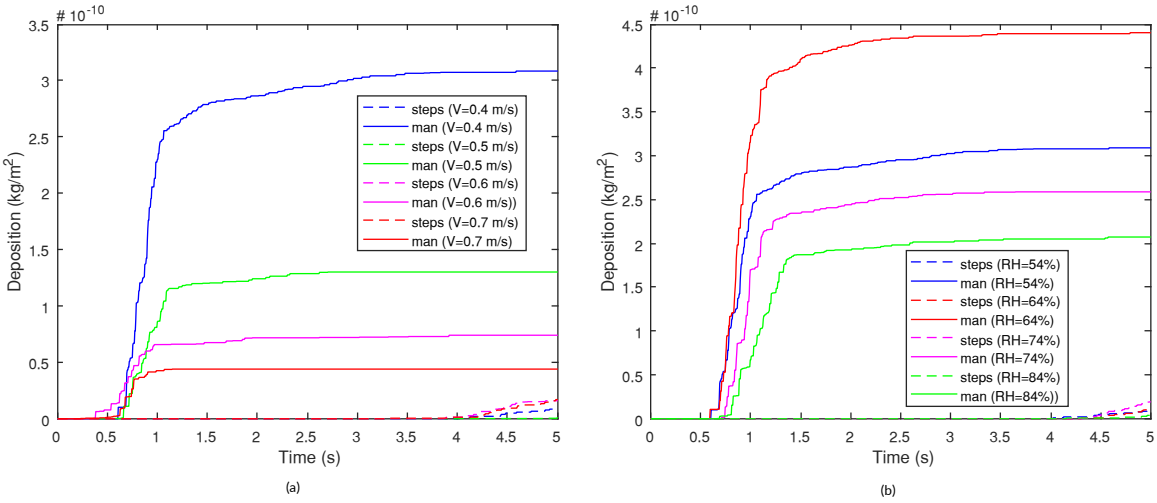

Figure 4.13. Deposition of droplets for different (a) escalator velocities, (b) RHs in upward-moving escalator

4.5. Response Surfaces of Cough Droplets

The response surfaces of deposition on the human body and steps, aerosol concentration, and penetration length at 5 s are shown in Figure 4.14(a-d) respectively. It is observed from Figure 4.14(a) that deposition on the human body in lower RH is higher at lower operational speed. But

between 0.6 ms^{-1} to 0.7 ms^{-1}, higher deposition is observed for RH between 60-70%. In Figure **4.14**(b), higher operational speeds with RH between 65-75% demonstrate higher deposition on the steps. The lowest aerosol concentration is found in Figure **4.14**(c) for the speed of 0.4 *m/s* and 0.7 *m/s* at 54% RH. From Figure **4.14**(d), higher droplet penetration length is found at higher operational speed and lower RH. Four quadratic fittings are derived using the contours from Figure **4.14**(a-d) as a function of escalator operational speed and RH for the deposition of cough droplets on the human body and steps, concentration of aerosol, and penetration length.

$$Dm(V,RH) = 1.634 \times 10^{-9} - 6.462 \times 10^{-9}\, V + 1.598 \times 10^{-11}\, RH + 4.382 \times 10^{-9}\, V^2 + 1.19 \times 10^{-11}\, V\, RH - 1.825 \times 10^{-13}\, RH^2 \quad (4.1)$$

$$Ds(V,RH) = -1.903 \times 10^{-10} - 1.627 \times 10^{-10}\, V + 6.838 \times 10^{-12}\, RH + 1.679 \times 10^{-10}\, V^2 + 5.046 \times 10^{-13}\, V\, RH - 5.054 \times 10^{-14}\, RH^2 \quad (4.2)$$

$$C(V,RH) = -4.707 \times 10^{-11} + 1.184 \times 10^{-09}\, V - 4.31 \times 10^{-12}\, RH - 1.311 \times 10^{-09}\, V^2 + 4.544 \times 10^{-12}\, V\, RH + 5.783 \times 10^{-14}\, RH^2 \quad (4.3)$$

$$L(V,RH) = -3.861 + 22.68\, V + 0.02468\, RH - 11.1\, V^2 - 0.08264\, V\, RH + 5.772 \times 10^{-05}\, RH^2 \quad (4.4)$$

The statistics of fit quality are mentioned in the Table 4.1.

Table 4.1. Statistics of fit quality for UME

Functions	**SSE**	**R-square**	**Adjusted R-square**	**RMSE**
$Dm(V,RH)$	1.74e-20	0.9152	0.8445	5.38e-11
Ds(V, RH)	1.66e-22	0.828	0.6847	5.26e-12
$C(V,RH)$	3.89e-22	0.9949	0.9906	8.047e-12
L(V, RH)	0.0987	0.9777	0.9591	0.1282

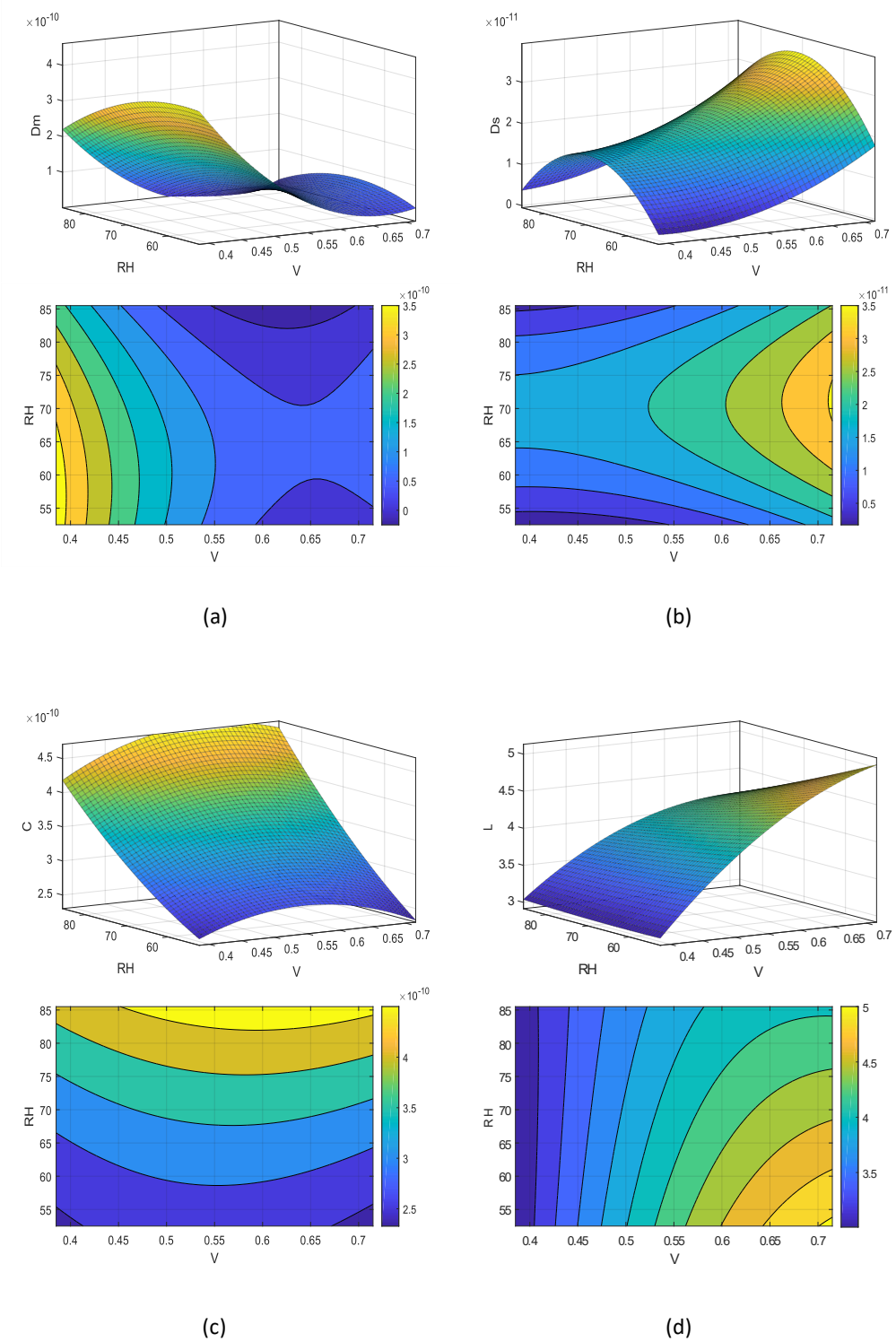

Figure 4.14. Response surface of (a) deposition on the human body, (b) deposition on steps, (c) aerosol concentration, (d) droplet penetration length in upward-moving escalator

4.6. Multi-objective Optimization

A multi-objective optimization was carried out using a metaheuristic genetic algorithm (GA) to identify the optimal operational speed and RH for minimizing aerosol concentration and aerosol penetration length from a cough. The objectives focused on reducing aerosol concentration and penetration length by adjusting the operational speed and RH as design variables. The Pareto front, which contains non-dominated solutions, is illustrated in Figure 4.15. Non-dominated solutions of Pareto front for UME are listed in table A2.

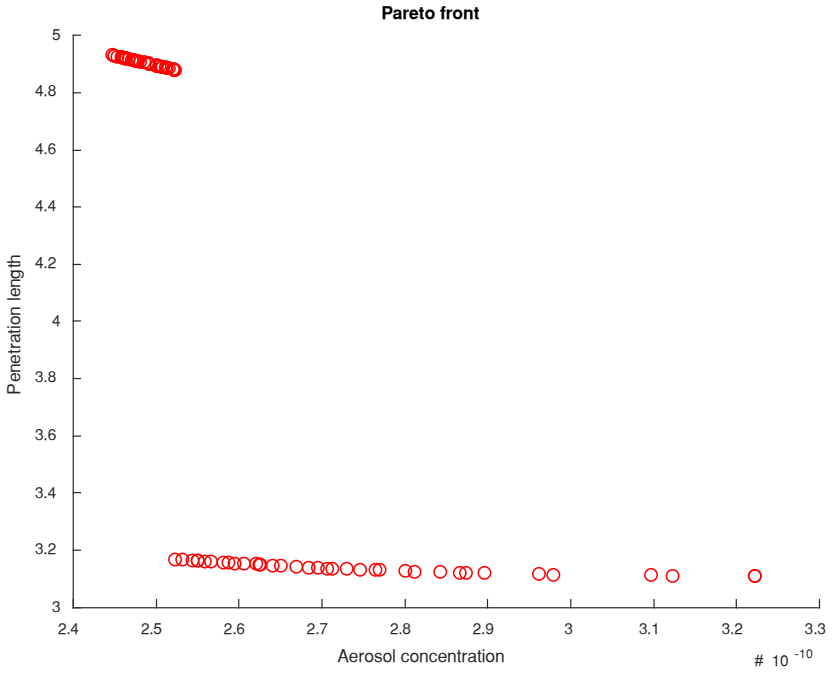

Figure 4.15. Pareto front of UME optimization

The Pareto front exhibits two distinct zones due to the concave response surface. From the non-dominated solutions of the Pareto front, it is noticeable that higher operational speed and lower RH are responsible for lower concentration with increased penetration length. As the aerosol concentration increases, the droplet penetration length is reduced.

Small changes in escalator operational speed have a greater impact on droplet penetration length than small changes in RH. Conversely, small changes in RH, have a greater impact on escalator operational speed than small changes in RH.

4.7. Conclusion

The investigation into cough droplet transmission dynamics on an upward-moving escalator provided detailed insights into the complex interplay between airflow dynamics, droplet behavior, and environmental conditions. The study focused on understanding how cough droplets and their nuclei disperse and settle in a unique scenario, namely, on an escalator in motion.

The airflow dynamics were found to be crucial, with properties such as velocity magnitude, vorticity, and turbulent kinetic energy influencing the fate of aerosol transport. The velocity contours revealed interesting patterns, showing that escalator speed and RH affected the airflow around the human body, leading to recirculation zones where cough aerosols could linger and potentially spread. The wake region behind the passenger was particularly important, as it showed how the body acted as a bluff-body, impacting the flow and dispersion of droplets. Turbulent kinetic energy (TKE) distribution was also examined, showing that escalator speed and RH influenced the intensity and extent of turbulence. Higher escalator speeds resulted in more significant turbulent effects, affecting the movement and dispersion of cough droplets. The TKE contours highlighted how turbulence varied along the escalator, with higher speeds and lower RH leading to increased turbulence intensity. The study also looked at droplet penetration lengths, showing that higher escalator speeds and lower RH were associated with greater penetration distances. Droplet evaporation played a significant role, affecting droplet sizes and trajectories. Evaporation rates were higher at higher escalator speeds and lower RH, leading to changes in droplet behavior over time. Deposition of droplets on surfaces, such as the human body and escalator steps, was influenced by various factors, including airflow patterns, velocity, RH, turbulence, and droplet properties. Lower RH resulted in higher deposition on the human body, while higher escalator speeds led to higher deposition on escalator steps. Multi-objective optimization using a genetic algorithm was performed to identify optimal escalator speeds and RH levels for minimizing aerosol concentration and droplet penetration length. The Pareto front

showed trade-offs between reducing aerosol concentration and minimizing penetration length, highlighting the complex relationships between these variables.

In conclusion, the study provided valuable insights into the transmission dynamics of cough droplets on an upward-moving escalator. The findings underscore the importance of considering airflow dynamics, turbulence, droplet behavior, and environmental conditions when assessing the risk of airborne disease transmission in indoor environments like escalators.

Chapter 5
Results & Discussion: Downward Moving Escalator

This chapter provides results and discussions of numerical simulations of the cough aerosol transmission in a downward-moving escalator. Simulations were carried out to better understand the transmission of cough droplets in a downward-moving escalator by altering velocity, and relative humidity.

5.1. Airflow Dynamics

The velocity contour, turbulent kinetic energy, and droplet trajectories are analyzed in this section.

5.1.1. Velocity Contour

Figure **5.1** shows velocity contours at midplane for two different escalator velocities of 0.4 *m/s* and 0.6 *m/s*. There is no-slip condition on the boundary of escalator steps and the human body. The velocity between the consecutive steps is much lower. There is always a recirculation of air between two steps for all cases. The airflow over the steps acts as forward-facing steps (FFS). The flow is separated at the corner of the steps. On the contrary, flow separation occurs behind the head which forms a recirculation zone. The wake zone behind the human for escalator velocity of 0.6 *m/s* is much greater than 0.4 *m/s* escalator velocity. The cough aerosol recirculates with the air in this wake zone. The maximum velocity is located at the forehead for both velocities. In the near wake of the human, multiple recirculation zones are formed. Higher wake zones are found in downward-moving escalator than downward-moving escalator. The velocity field for 54% RH is almost similar to 84% RH. Overall, observing the wake flow behind the passenger reveals that the body of the passenger acts as a bluff-body.

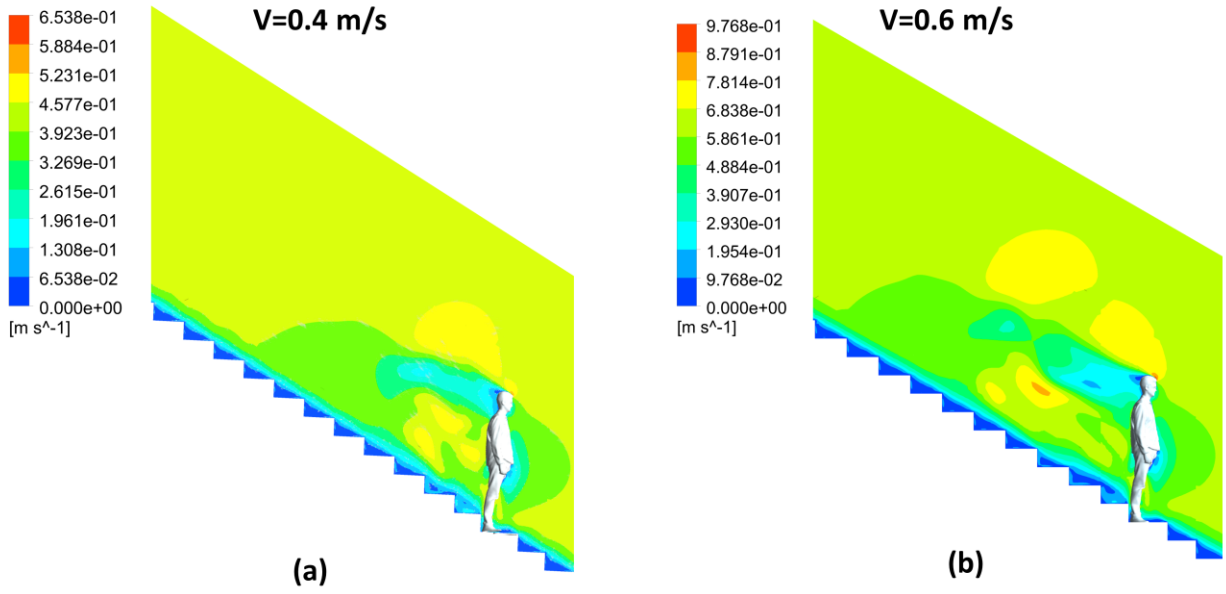

Figure 5.1. Velocity contours for different escalator velocities in downward-moving escalator (at midplane, velocity effect) a) v=0.4 *m/s*, b) v=0.6 *m/s*

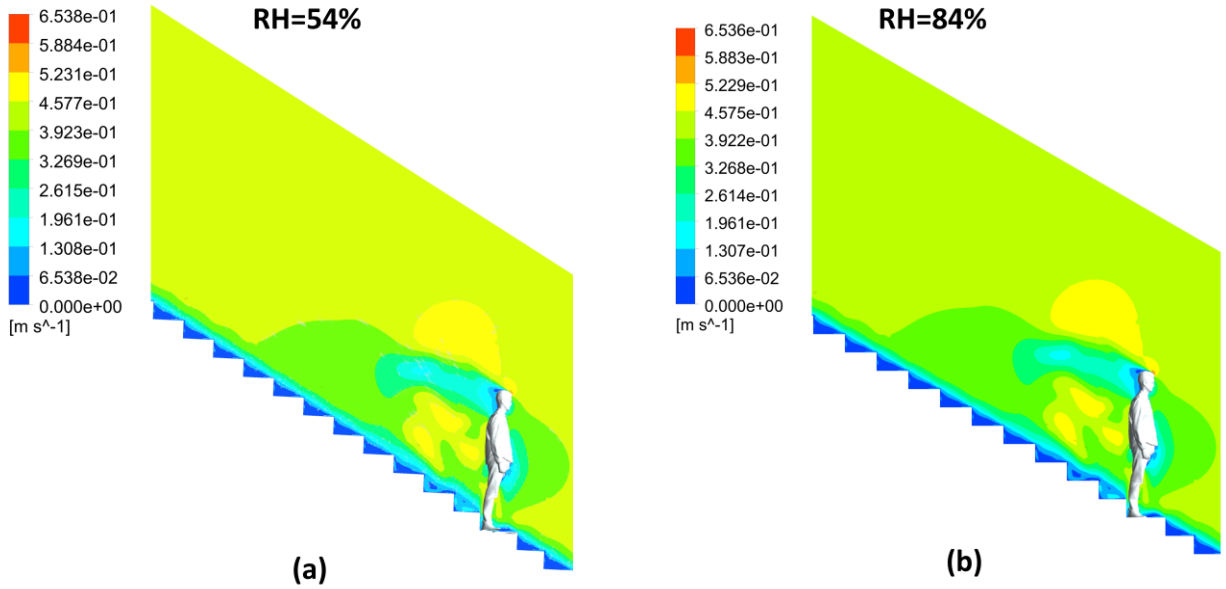

Figure 5.2. Velocity contours for different escalator velocities in downward-moving escalator (at midplane, RH effect) a) RH=54%, b) RH=84%

5.1.2. Turbulent Kinetic Energy

The variation of turbulent kinetic energy at mid-plane is demonstrated by Figure **5.3** for downward-moving escalator velocities of 0.4 *m/s* and 0.6 *m/s*. The maximum turbulent kinetic energy for all cases is found behind the leg. The regions near the step's outer sharp edge contain higher kinetic energy than the inner region of consecutive steps. As predicted, the region of increased turbulent kinetic energy expands with increasing escalator velocity, with 0.6 *m/s* having a greater value than 0.4 *m/s*. Figure **5.4** depicts the variation of turbulent kinetic energy at mid-plane for 54% and 84% RH in downward-moving escalator. The zones of turbulent kinetic energy for lower and higher RH are nearly the same.

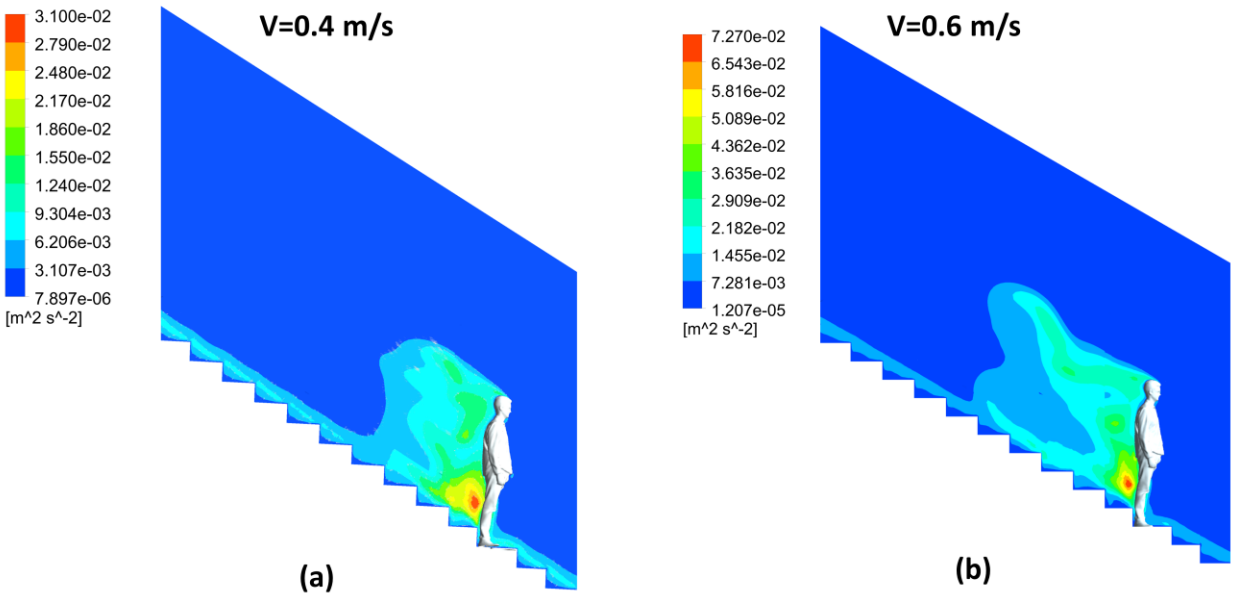

Figure 5.3. Turbulent kinetic energy for different escalator velocities in downward-moving escalator (at midplane, velocity effect) a) v=0.4 *m/s*, b) v=0.6 *m/s*

Figure 5.4. Turbulent kinetic energy for different escalator velocities in downward-moving escalator (at midplane, RH effect) a) RH=54%, b) RH=84%

5.2. Cough Droplets Penetration

Figure **5.5**(a) illustrates the penetration length of 0.4 *m/s* and 0.5 *m/s* downward-moving escalators with ambient relative humidity and temperature of 54% and 25℃. The effect of escalator velocity on cough droplet penetration length is nearly identical up to 0.18 *s*. After 0.18 *s*, escalator velocity of 0.6 *m/s* demonstrates higher penetration length than 0.4 *m/s*. Cough droplet penetration length in a 0.6 *m/s* downward-moving escalator is 2.23 *m* at 5 *s*, which is almost 24.6 percent greater than 0.4 *m/s*. The penetration length in a 0.6 *m/s* downward-moving escalator is roughly 80 to 85 percent greater than that of a 0.4 *m/s* escalator between 0.27 *s* and 0.36 *s*. The penetration length gradient for 0.4 *m/s* is substantially lower between 3.5 *s* to 4.0 *s*. For both escalator velocities, the penetration length of cough droplets increases with flow time. The penetration length of cough droplets in 54% and 84% ambient relative humidity is demonstrated in Figure **5.5**(b) for downward-moving escalator with velocity and temperature of 0.4 *m/s* and 25℃. For both ambient relative humidity, the penetration length is almost the same up to 1.2 *s*. Cough droplets penetrate 1.79 *m* and 1.69 *m* at 5 *s* for 54 percent and 84 percent ambient relative humidity, respectively. Higher humidity reduces the droplets' penetration length.

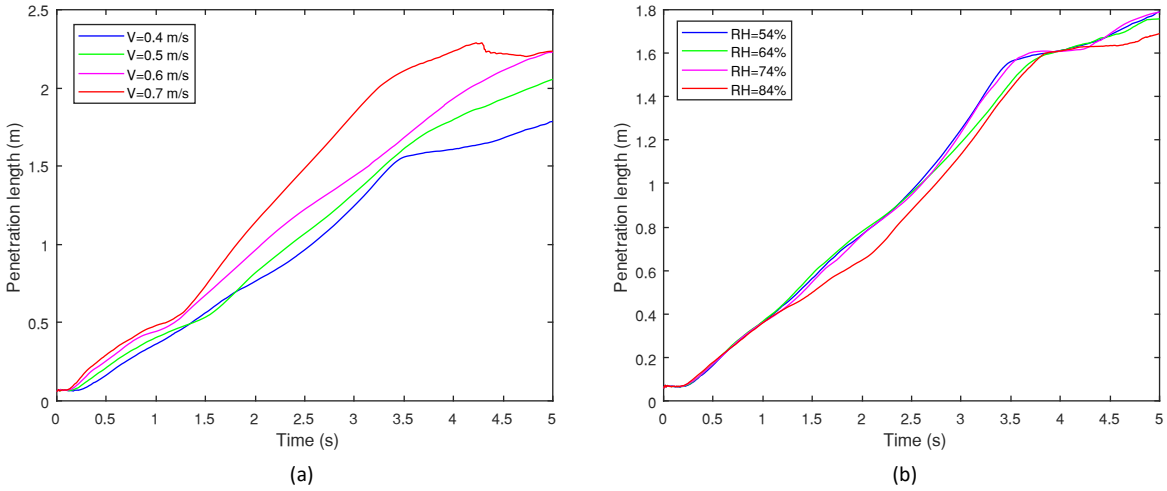

Figure 5.5. Penetration length for different (a) escalator velocities (b) RHs in downward-moving escalator

The dispersion of the droplet for the downward-moving escalator is illustrated for 0.4 *m/s* (Figure **5.6** (a, c, e, g, i)) and 0.6 *m/s* (Figure **5.6** (b, d, f, h, j)) operational speed at 54% RH. Cough droplet trajectory differences between escalator velocities of 0.4 *m/s* and 0.6 *m/s* at 0.2 *s* are essentially negligible. The effect of escalator velocity becomes prominent after 0.5 *s*. The droplets enter the recirculation zone behind the torso after 1*s*. At 5 s, cough droplets are found between the steps. The droplets contaminate the full body if another passenger stands three steps behind the index patient. At 5 *s*, most of the larger droplets are found near the steps. The vertical and horizontal dispersion of cough aerosol in the downward-moving escalator is found higher than the upward-moving escalator. Higher escalator operational speed causes greater dispersion. The dispersion for 0.6 *m/s* operation speed is found up to the sixth step behind the index patient, while it was up to the fourth step for 0.4 *m/s*. The maximum and minimum droplet sizes for both escalator velocities are 23 μm and 0.464 μm at 5 *s*.

The trajectories of cough droplets for the ambient relative humidity of 54% (Figure **5.7**(a, c, e, g, i)) and 84% (Figure **5.7** (b, d, f, h, j) at 0.4 ms^{-1} is shown in Figure **5.7**. The maximum and minimum droplet sizes for both ambient relative humidities are 23 μm and 0.464 μm at 5 s. The dispersion of cough droplets is observed a little bit higher for the lower RH.

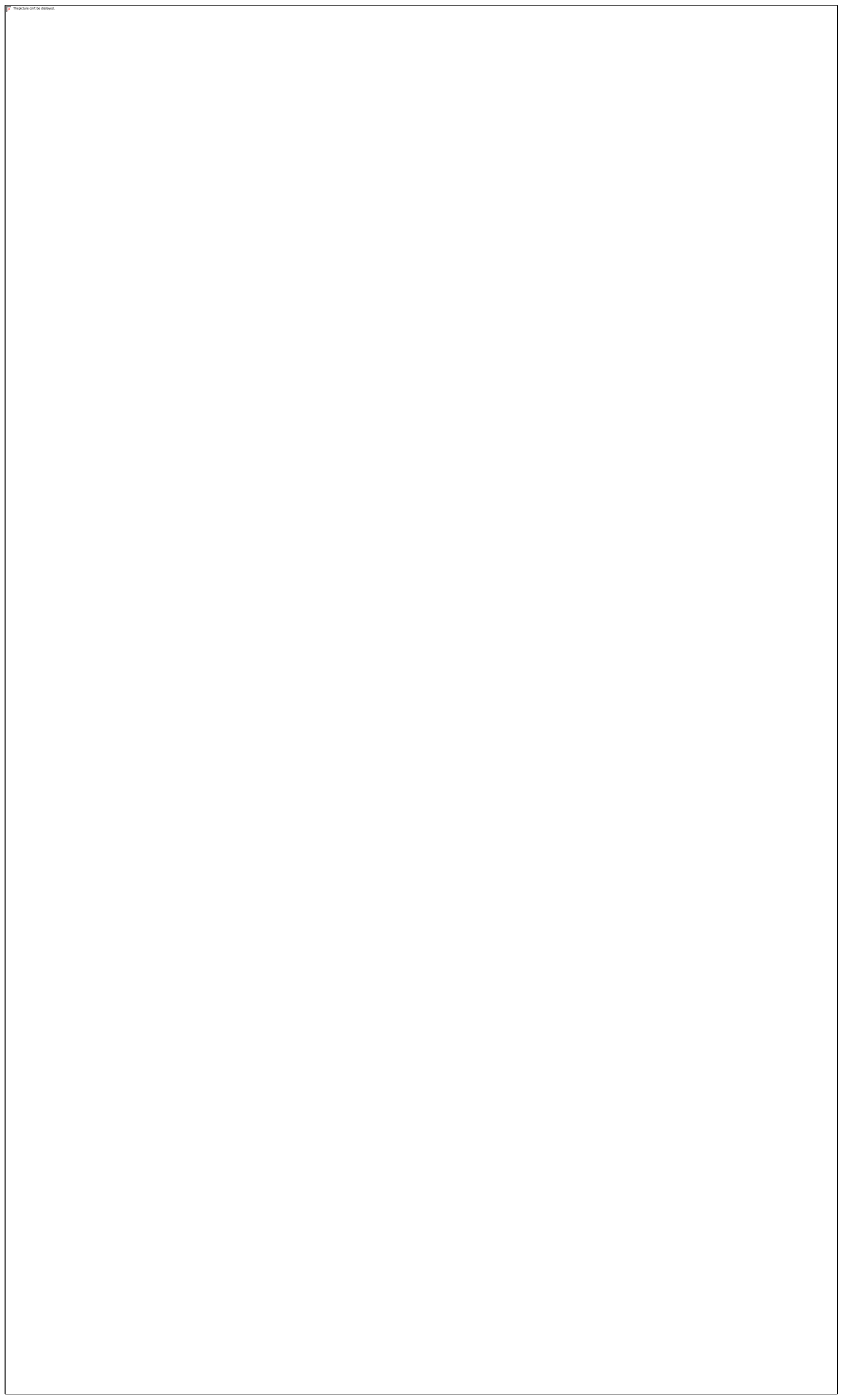

Figure 5.6. Cough droplet trajectories for different escalator velocities at different times in downward-moving escalator (velocity effect)

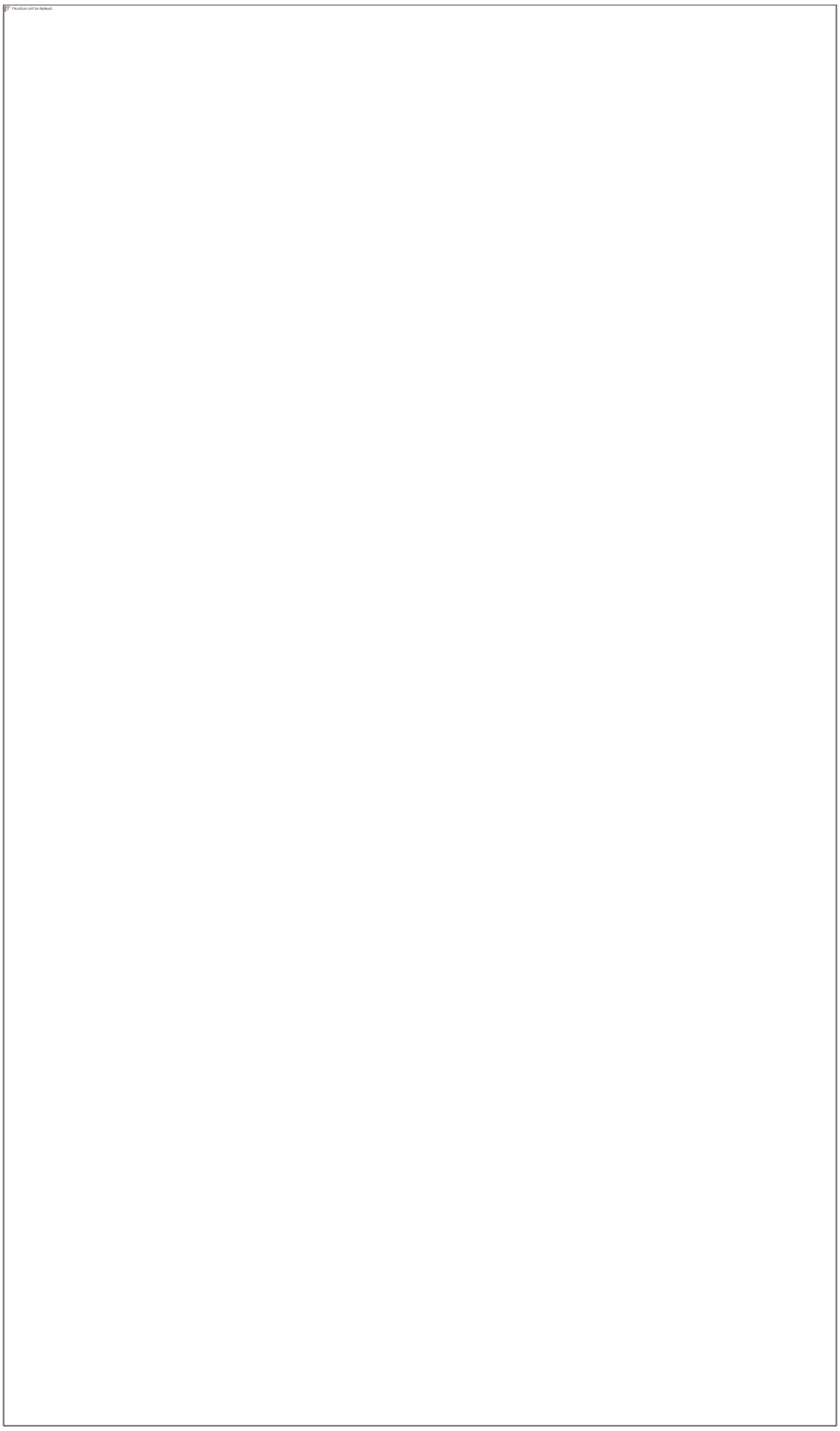

Figure 5.7. Cough droplet trajectories for different escalator velocities at different times in upward-moving escalator (RH effect)

Figure **5.8** illustrates the droplets along with the path lines of air for the escalator velocity of 0.4 *m/s* and 0.6 *m/s* at 5 *s* flow time. The recirculation of droplets is observed from the second step behind the index passenger for the escalator velocity of 0.4 *m/s* , whereas it is found from the third step for the escalator velocity of 0.6 *m/s*. The horizontal distance for 0.4 *m/s* and 0.6 *m/s* escalator velocities traveled by the cough droplets is approximately 1.52 *m* and 2.29 *m* from the body of the infected person. Overall, the horizontal dispersion distance increases along with increase in escalator operational speed. Figure 5.9 traces the droplets along with path lines of air for RHs of 54% and 84% at 0.4 *m/s* in a downward-moving escalator. Recirculation regions develop between the steps. Cough droplets enter the circulation zone between the steps at an early flow time for a lower relative humidity of 54%. Droplets recirculation with air between two steps starts from the second step behind the human body for both RHs. The horizontal distance for 54% and 84% RH traveled by the cough droplets is approximately 1.52 *m* from the body of the infected person.

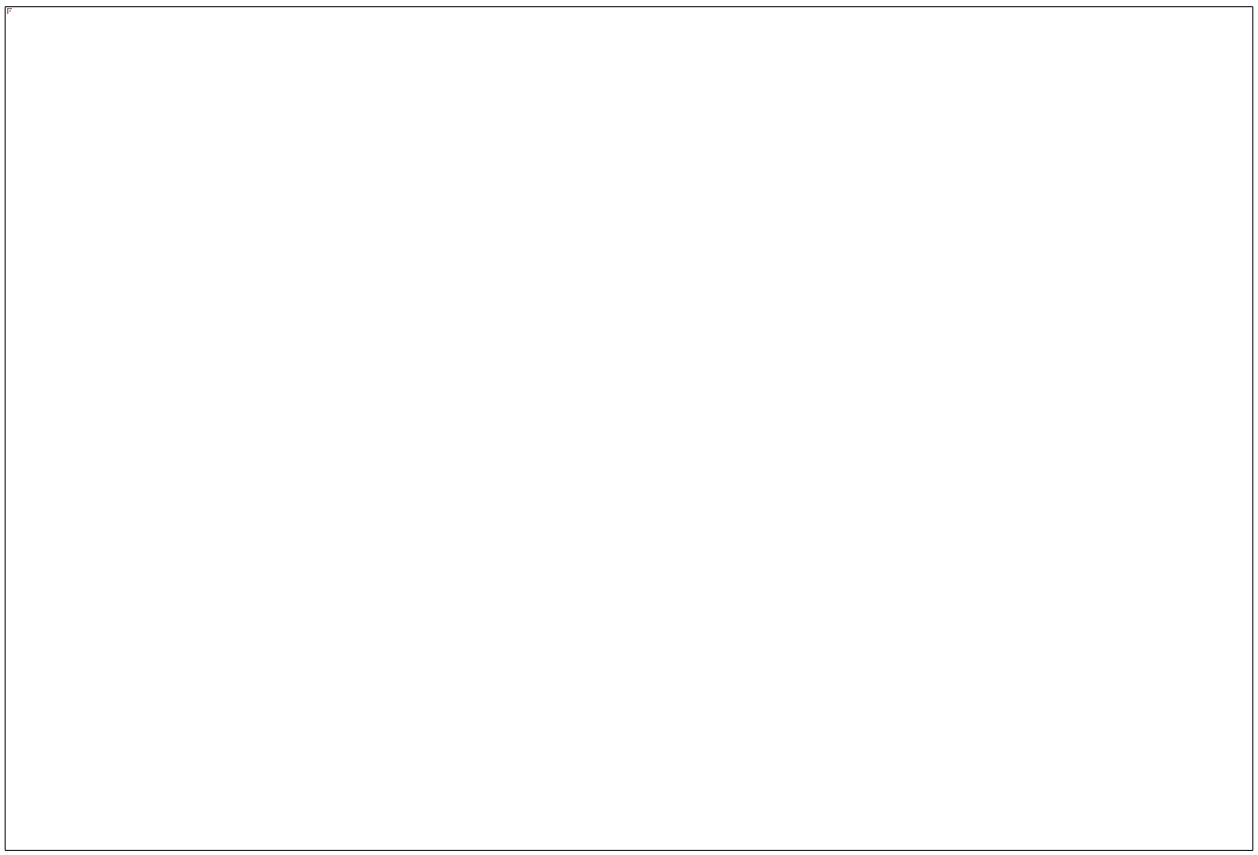

Figure **5.8**. Path lines of phase 1 and cough droplets trace for different escalator velocities in upward-moving escalator (at t= 5 s, RH=54%, velocity effect)

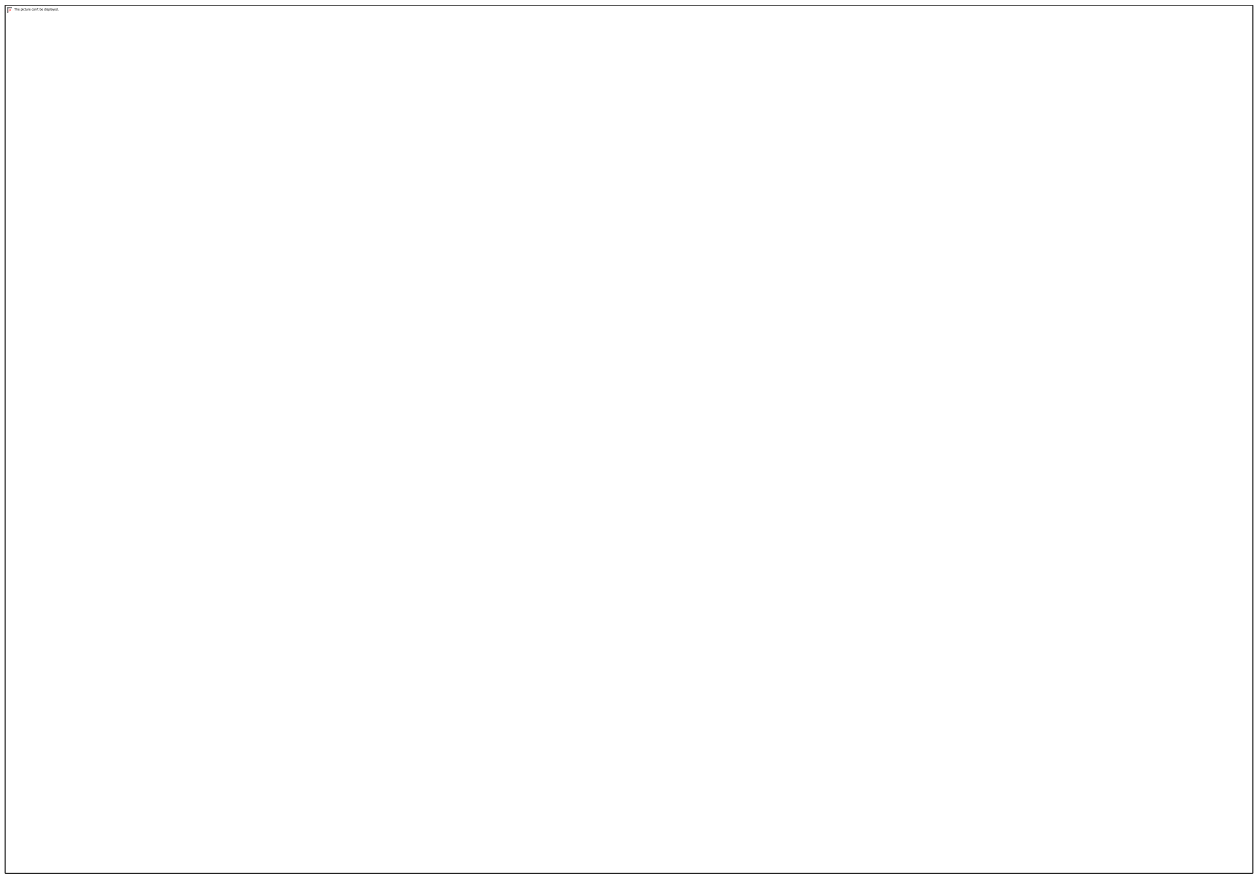

Figure 5.9. Path lines of phase 1 and cough droplets trace for different escalator velocities in upward-moving escalator (at t= 5 s, V=0.4 ms^{-1}, RH effect)

5.3. Evaporation of Droplets

5.3.1. Evaporation Rate

The rate of evaporation of cough droplets in downward-moving escalator is compared in Figure **5.10**(a) for escalator velocities of 0.4 *m/s* and 0.6 *m/s* with ambient relative humidity and temperature of 54% and 25°*C*, respectively. The maximum evaporation takes place at 0.06 *s* which is 1.8×10^{-8} *kg/s*. The evaporation rate for both escalator velocities is substantially higher up to 0.5 *s* than the remaining flow time as the higher kinetic energy helps to escape the Knudsen layer. Because of the reduction in kinetic energy, evaporation decreases dramatically between 0.5 *s* to 0.7 *s* as soon as the injection of cough droplets stops at 0.5 *s*. The rate of evaporation for two different ambient RHs of 54% and 84% is demonstrated in Figure **5.10**(b) with downward-escalator velocity of 0.4 *m/s*. Because of the significant volume of water vapor in the air with

higher humidity, the rate of evaporation of cough droplets is comparatively slower. The maximum evaporation of cough droplets at 54% and 84% ambient relative humidity occurs in 0.065 *s* and 0.045 *s* which are 1.76×10^{-08} *kg/s* and 8.72×10^{-09} *kg/s* respectively. Evaporation is much higher during the injection period due to the higher kinetic energy of cough droplets. Between 1.2 s to 4.3 *s*, the evaporation rate has plateaued out in 84% ambient relative humidity.

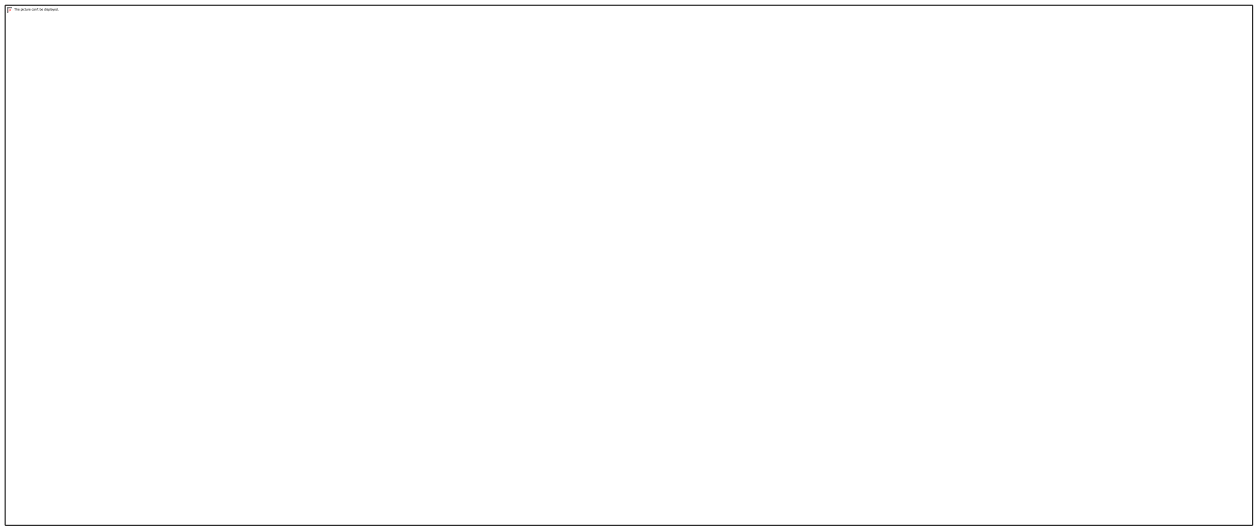

Figure 5.10. Evaporation rate for different (a) escalator velocities, (b) RHs in downward-moving escalator

5.3.2. Average Droplets Diameter

The average diameter of droplets decreases owing to evaporation while increasing due to coalescence. The effect of escalator velocity and ambient relative humidity is investigated on the average cough droplets diameter in this section.

Figure **5.11**(a) depicts the change in average diameter of droplets over time as a result of the evaporation and coalescence processes in a downward-moving escalator with velocities of 0.4 *m/s* and 0.6 *m/s* at 54% relative humidity. It is observed that the average diameter of cough droplets increases up to 0.02 *s*. The number of the droplets decreases because of the coalescence process as the collision among the droplets is higher initially. After 0.02 *s*, the average diameter reduces dramatically up to 0.23 *s* because of the higher evaporation rate for both velocities. The average

diameter of cough droplets for 0.6 *m/s* escalator velocity is greater than the velocity of 0.4 *m/s* up to 3.1 *s*. The coalescence is significantly higher in escalator velocity of 0.4 *m/s* after 3.1 *s*. At 5 *s*, the average diameter is approximately the same for both velocities which is 6.5 μm.

The average droplets diameter for two different ambient relative humidities of 54% and 84% in 0.4 *m/s* downward-moving escalator is compared by Figure **5.11**(b). The average diameter of cough droplets increases up to 0.02 *s* because of greater coalescence effect. Later, the average diameter decreases substantially up to 0.23 *s* in both ambient relative humidities. Some fluctuations are noticeable after 0.23 *s*. Higher average diameter is observed for ambient relative humidity of 84% except between 3.1 *s* to 4.6 *s*. Higher coalescence effect is observed as soon as the cough droplets reaches into the recirculation zone near the steps after 3.1 *s*.

Figure 5.11. Average droplets diameter for different (a) escalator velocities (b) RHs in downward-moving escalator

5.4. Deposition of Droplets

Deposited cough droplets cause indirect contact transmission of the SARS virus. Escalator velocity and ambient relative humidity affect the deposition of cough droplets. The amount of deposition on the escalator steps and the skin of human is investigated in this section.

Figure 5.12(a) depicts the deposition of cough droplets at 0.4 *m/s* and 0.6 *m/s* downward escalator velocities with an ambient relative humidity of 54%. Deposition of cough droplets on

human skin in 0.6 *m/s* downward-moving escalator starts from 0.215 *s* whereas it begins from 0.315 *s* in 0.4 *m/s* downward-moving escalator. The deposition is greater at 0.6 *m/s* escalator velocity than escalator velocity of 0.4 *m/s*. At 5 s, the deposition on the man's skin for 0.6 *m/s* is $4.38 \times 10^{-11}\ kg/m^2$ which is approximately 319 % higher than 0.4 *m/s*. The deposition on the steps of the escalator begins approximately at 3.905 *s* and 4.215 *s* for escalator velocities of 0.4 *m/s* and 0.6 *m/s* respectively. At 5 *s*, the deposition on the steps of the escalator for 0.4 *m/s* and 0.6 *m/s* are $1.1 \times 10^{-11}\ kg/m^2$ and $1.55 \times 10^{-12}\ kg/m^2$ respectively.

The deposition of cough droplets is demonstrated in Figure **5.12**(b) for two different ambient relative humidities of 54% and 84% at the downward-escalator velocity of 0.4 *m/s*. Deposition of cough droplets on human skin in 54% relative humidity starts from 0.315 *s* whereas it begins from 0.25 *s* in 84% ambient relative humidity. It is seen that deposition is greater in 84% ambient relative humidity. At 5 *s*, the deposition on the man's skin in 84% ambient relative humidity is $4.34 \times 10^{-11}\ kg/m^2$ which is approximately 315 % higher than the ambient relative humidity of 84%. The deposition of cough droplets on the escalator steps in ambient relative humidity of 54% and 84% begins from 3.91 *s* and 3.79 *s* respectively.

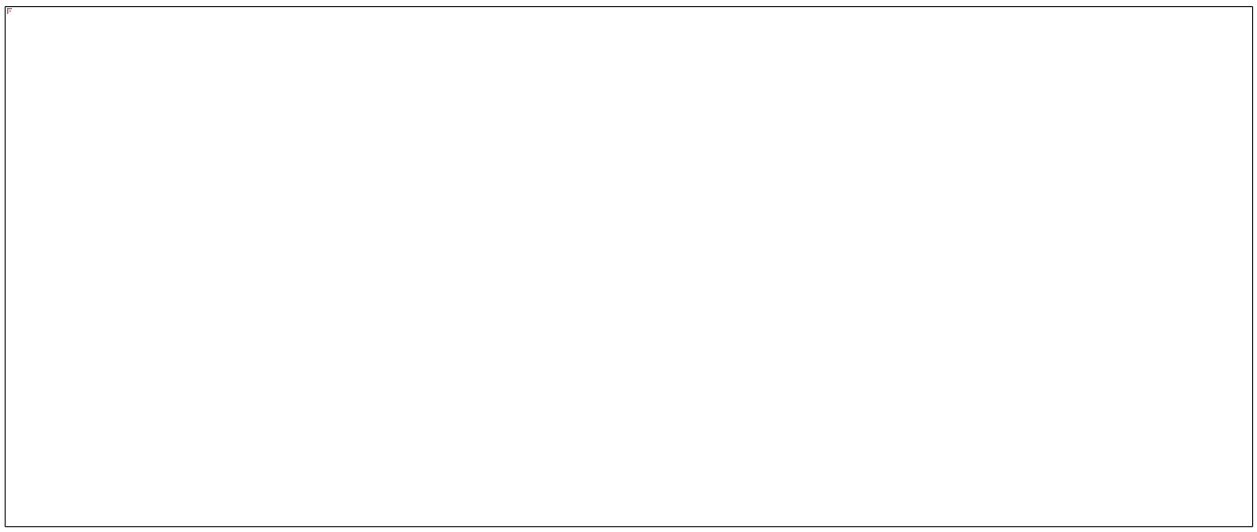

Figure 5.12. Deposition of droplets for different (a) escalator velocities, (b) RHs in velocities in downward-moving escalator

5.5. Response Surfaces of Cough Droplets

The response surfaces of deposition on the human body and steps, aerosol concentration, and penetration length at 5 *s* are demonstrated in Figure 5.13 (a-d) respectively. It is observed from Figure **5.13**(a) that deposition on the human body in lower RH is higher at lower operational speed. But between 0.6 *m/s* to 0.7 *m/s* , higher deposition is observed for RH between 60-70%. In Figure **5.13**(b), higher operational speeds with RH between 65-75% demonstrate higher deposition on the steps. The lowest aerosol concentration is found in Figure 5.13(c) for the speed of 0.4 *m/s* and 0.7 *m/s* at 54% RH. From Figure **5.13**(d), higher droplet penetration length is found at higher operational speed and higher RH. Four quadratic fittings are derived using the contours from Figure 5.13 (a-d) as a function of escalator operational speed and RH for the deposition of cough droplets on the human body and steps, concentration of aerosol, and penetration length.

$$Dm(V,RH) = 1.291 \times 10^{-10} - 6.555 \times 10^{-10}\, V - 8.737 \times 10^{-13}\, RH + 6.267 \times 10^{-10}\, V^2 + 4.276 \times 10^{-12}\, V\, RH \quad (5.1)$$

$$Ds(V,RH) = -4.236 \times 10^{-11} + 5.646 \times 10^{-12}\, V + 1.564 \times 10^{-12}\, RH - 1.249 \times 10^{-11}\, V^2 - 1.545 \times 10^{-13}\, V\, RH - 1.044 \times 10^{-14}\, RH^2 \quad (5.2)$$

$$C(V,RH) = 5.22 \times 10^{-10} - 6.507 \times 10^{-10}\, V + 4.618 \times 10^{-13}\, RH + 1.073 \times 10^{-10}\, V^2 + 5.457 \times 10^{-12}\, V\, RH \quad (5.3)$$

$$L(V,RH) = 2.285 - 1.066\, V - 0.01643\, RH + 0.5575\, V^2 + 0.03459\, V\, RH \quad (5.4)$$

The statistics of fit quality are mentioned in the following Table 5.1.

Table 5.1. Statistics of fit quality for DME

Functions	SSE	R-square	Adjusted R-square	RMSE
$Dm(V,RH)$	9.933e-33	0.8735	0.8103	3.524e-17
Ds(V, RH)	1.194e-33	0.7267	0.5315	-
$C(V,RH)$	4.398e-32	0.9777	0.9666	7.415e-17
L(V, RH)	3.402e-13	0.8873	0.8309	2.062e-07

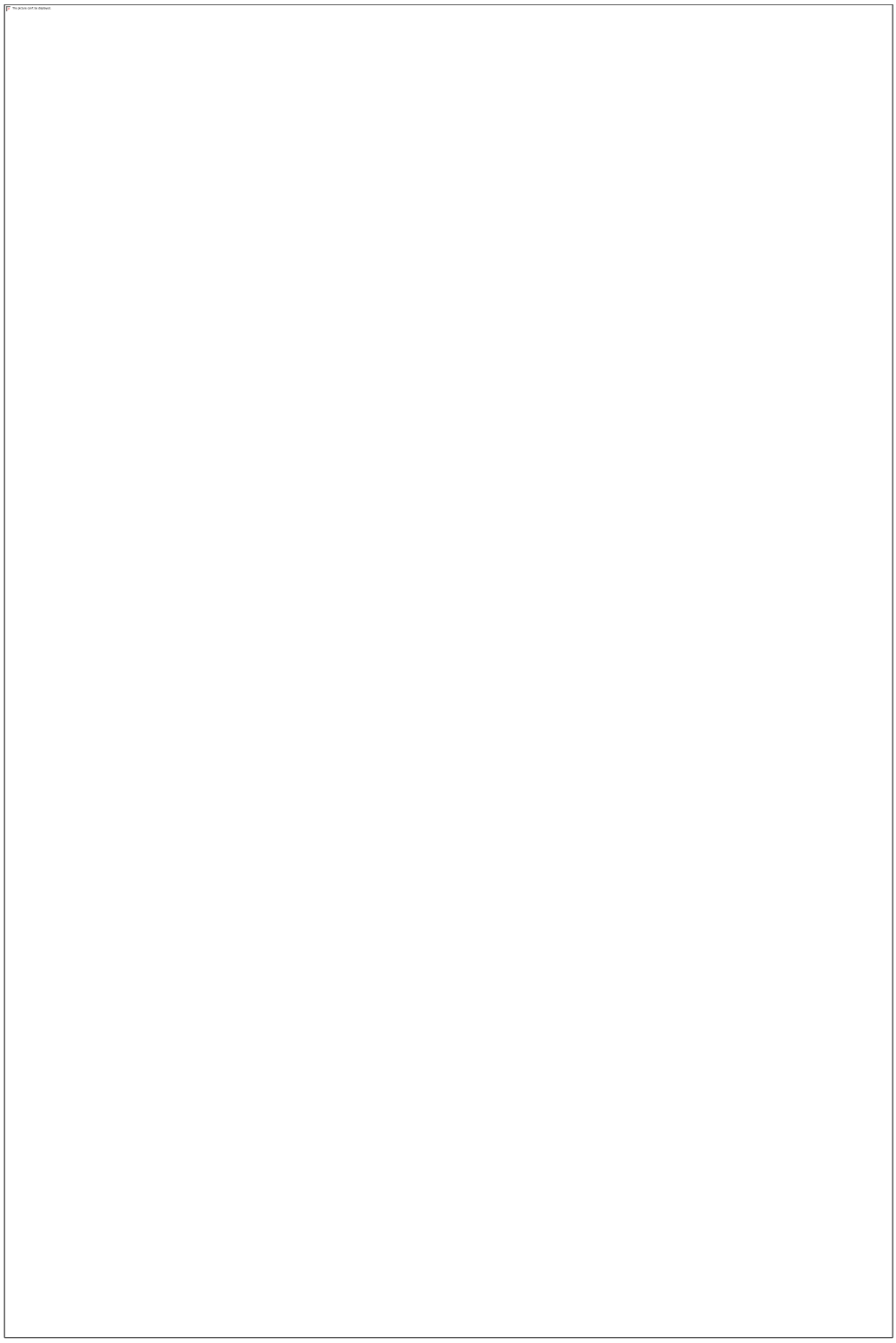

Figure 5.13. Response surface of (a) deposition on the human body, (b) deposition on steps, (c) aerosol concentration, (d) droplet penetration length in downward-moving escalator

5.6. Multi-objective Optimization

A metaheuristic genetic algorithm (GA) was used in a multi-objective optimization to determine the ideal operational speed and RH for reducing aerosol concentration and aerosol penetration length from a cough. Figure 5.14 depicts the Pareto front, which includes non-dominated solutions. The non-dominated solutions of Pareto front for UME are listed in table B2.

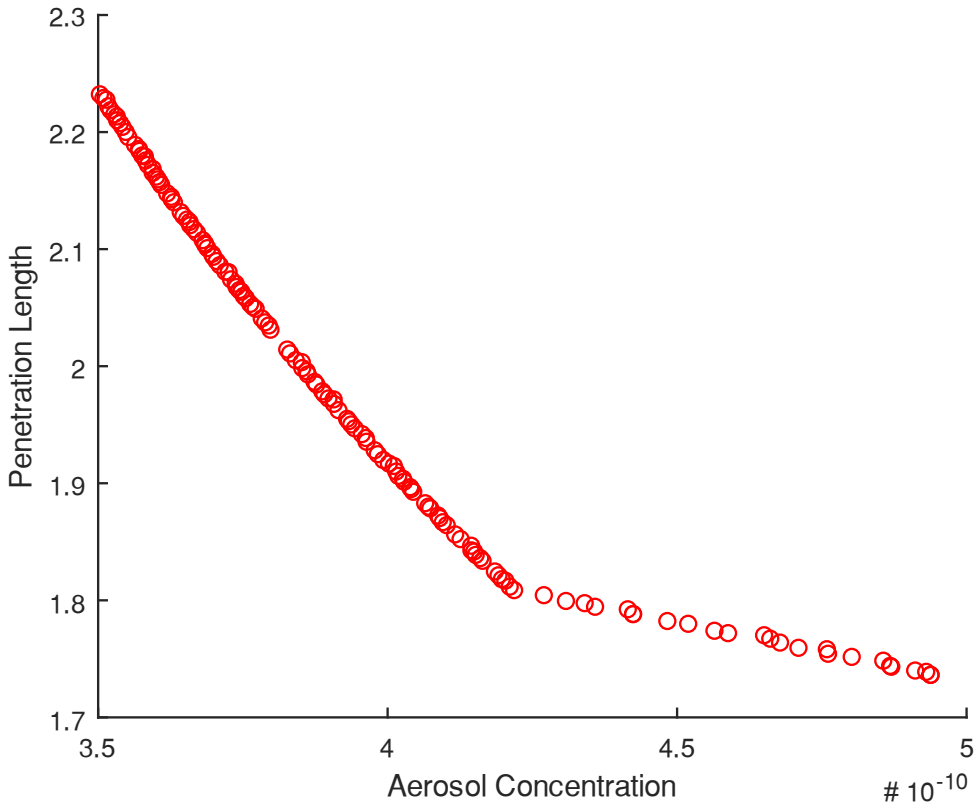

Figure 5.14. Pareto front of DME optimization

It is clear from the Pareto front's non-dominated solutions that faster operational speeds and lower relative humidity causes concentration to decrease while increasing penetration length. The droplet penetration length decreases with increasing aerosol concentration.

5.7. Conclusion

The numerical simulations of cough aerosol transmission in a downward-moving escalator offer a detailed understanding of the complex dynamics involved. The study focused on analyzing the effects of escalator velocity and ambient relative humidity on the dispersion, evaporation, and deposition of cough droplets.

One of the key findings was related to the airflow dynamics around the human body on the escalator. Velocity contours showed that the airflow over the steps created forward-facing steps (FFS) and separation zones behind the human, forming recirculation zones. The wake zone behind the human, where the maximum velocity was located, played a crucial role in recirculating cough aerosols. Higher escalator velocities resulted in larger wake zones, indicating increased potential for aerosol transmission. Turbulent kinetic energy (TKE) analysis revealed that the regions with higher TKE were located near the steps' outer sharp edges, indicating increased turbulence in these regions. The TKE distribution varied with escalator velocity, with higher velocities leading to a wider region of increased TKE. However, the TKE distribution was similar for different relative humidity levels, indicating that humidity had a minimal effect on turbulence intensity. The study also investigated the penetration length of cough droplets, showing that higher escalator velocities resulted in greater penetration lengths. The effect of relative humidity on penetration length was minimal, with both 54% and 84% RH showing similar penetration lengths. This finding suggests that escalator velocity plays a more significant role in droplet dispersion than relative humidity in this context. Evaporation analysis showed that the rate of evaporation of cough droplets was higher during the initial stages of the simulation, primarily due to the higher kinetic energy of the droplets. However, evaporation rates decreased as the droplets lost kinetic energy and the evaporation rate plateaued after a certain time. Higher relative humidity levels resulted in slower evaporation rates, likely due to the presence of water vapor in the air. The study also investigated the deposition of cough droplets on the escalator steps and human skin. It found that higher escalator velocities and lower relative humidity levels resulted in greater deposition on both surfaces. This finding suggests that escalator velocity and relative humidity are important factors to consider in mitigating the risk of indirect contact transmission of diseases like SARS.

In conclusion, the study provides valuable insights into the complex dynamics of cough aerosol transmission in a downward-moving escalator. The findings underscore the importance of considering airflow dynamics, escalator velocity, and relative humidity in indoor environments to mitigate the risk of airborne disease transmission. Further research in this area could help develop effective strategies to reduce the transmission of respiratory diseases in crowded indoor spaces.

Chapter 6
Result & Discussion: Aircraft Cabin

In this pivotal chapter, a comprehensive analysis of various key parameters is given, including Heat Removal Efficiency (HRE), Velocity Non-Uniformity Index (VNUI), Temperature Non-Uniformity Index (TNU), Percentage Dissatisfied (PD), Draft Rate (DR), and Airborne Disease Transmission Infection Risk. These parameters play a vital role in assessing the performance of aircraft cabin environments and guiding decisions related to cabin design and operation. Through an in-depth examination of these factors, this chapter, it is aimed to explore the cabin air quality, thermal comfort, and airborne disease transmission, while also proposing potential enhancements and solutions for the benefit of passengers and the aviation industry as a whole.

6.1. Ventilation Airflow

In this section, two key ventilation methods are focused: Mixing Ventilation (MV) and Displacement Ventilation (DV). The impact of additional outlets on DV's performance is also investigated.

The HRE of MV is 40.10%, while the HRE of DV is significantly higher at 67.73%. This high HRE of DV indicates that it is a more efficient system for removing heat from indoor spaces than MV due to the way it circulates air in a room. The HRE of DV can be worsened by about 5.9%, if extra outlets near two side walls are added, resulting in an HRE of 67.73% because of an increase in recirculation. The HRE of DV is 68.9% higher than MV. In a DV configuration, cool, fresh air is introduced into the aircraft cabin at a low level, usually near the floor, and removed through the exhaust outlets. As a result, the air in the cabin flows in a stratified pattern, with colder air at the bottom and warmer air near the ceiling. This stratified air-flow pattern is more efficient for removing heat from the cabin than the air-flow pattern created by MV, where colder air is mixed with warmer air throughout the cabin. As illustrated by air recirculation in Figure 6.1, there is a significant extent of air recirculation in the MV configuration which is constantly mixed and redistributed throughout the cabin. The stratified flow pattern of a DV layout, in contrast, lowers

air recirculation, which can aid in halting the spread of respiratory aerosol contaminants and maintain improved indoor air quality.

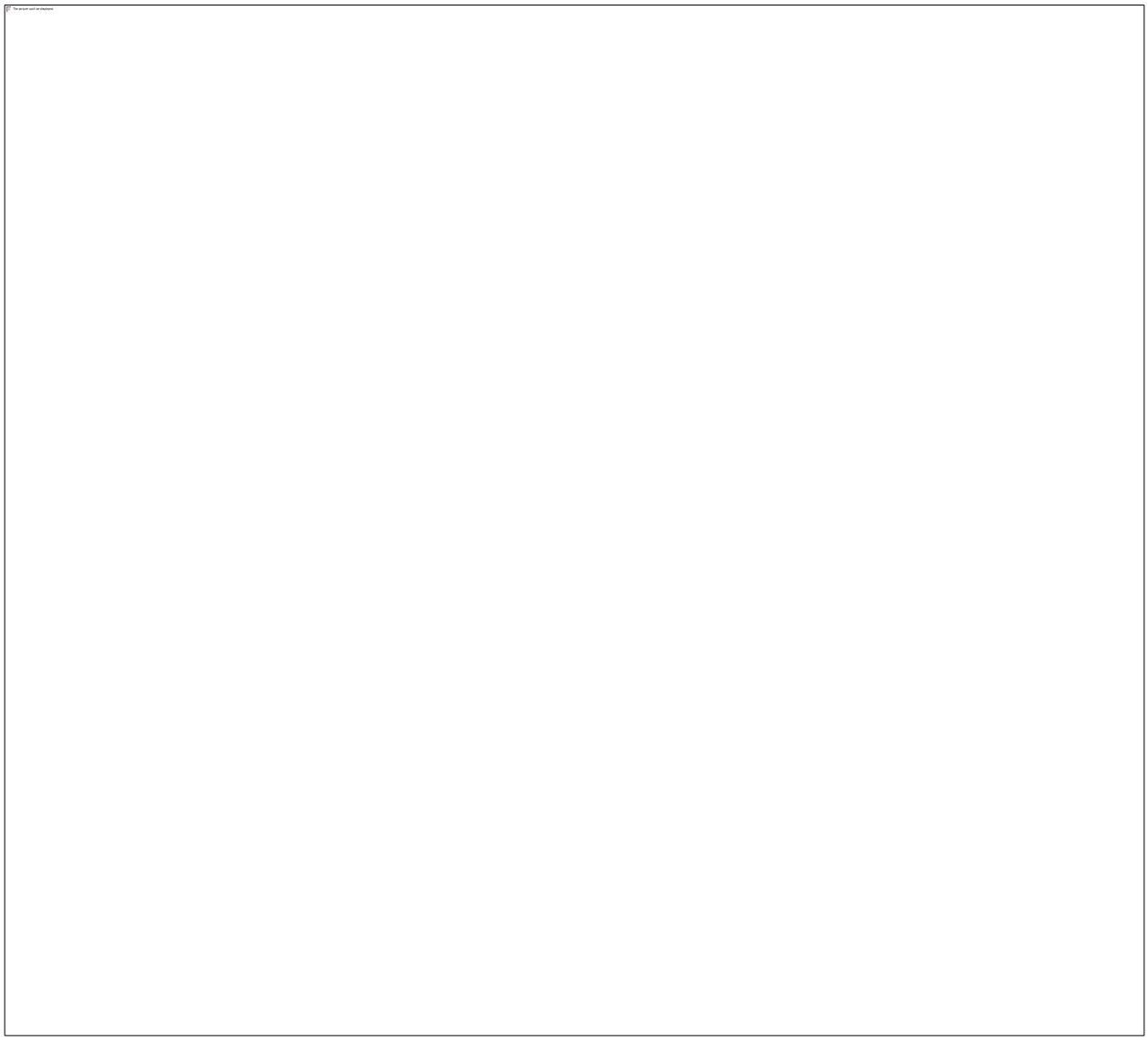

Figure 6.1. Air recirculation of (a) MV, (b) DV, and (c) DV – Extra outlet

Table 6.1. HRE for different ventilation configurations

Ventilation Type	HRE
MV	40.10%
DV	67.73%
DV – Extra outlet	63.96%

Table 6.2 and Table 6.3 show the VNUI and TNU values for three different types of ventilation systems: mechanical ventilation (MV), displacement ventilation (DV), and DV with an extra outlet. The highest VNUI value was observed in DV with a value of 0.731, indicating that the air velocity distribution in spaces using is somewhat uneven. The higher VNUI can lead to a greater amount of non-uniformity in the airflow distribution. On the other hand, the VNUI value for MV was significantly lower with a value of 0.487, indicating a more even air velocity distribution compared to DV. This is because the DV configuration works by providing fresh air near the cabin floor, which gradually rises and displaces the whole room's air. This results in a more non-uniform air distribution throughout the space. However, the VNUI value for DV with an extra outlet was slightly lower at 0.518 compared to DV. The extra outlet could potentially affect the air distribution pattern in the space. The results suggest that the MV configuration may provide a more even air velocity distribution compared to the DV configuration. Table 4 demonstrates that the MV has the lowest TNUI value of 0.487, indicating that it is effective at maintaining a consistent temperature distribution throughout the space. However, the DV has slightly higher TNUI values of 0.731, which suggests that there is some temperature non-uniformity within the cabin. The TNUI values for DV with and without an extra outlet are the same, indicating that the additional outlet did not significantly affect the TNUI of the ventilation configuration.

Table 6.2. VNUI for different ventilation configurations

Ventilation Type	VNUI
MV	0.487
DV	0.731
DV – Extra outlet	0.518

Table 6.3. TNUI for different ventilation configurations

Ventilation Type	TNUI
MV	0.00171
DV	0.00304
DV – Extra outlet	0.00304

Figure 6.2 presents the Percentage Dissatisfied (PD) of passengers with the MV, DV, and DV with extra outlet configuration in various aircraft cabin seats. The dissatisfaction levels of MV configuration range from as low as 0.34% to as high as 6.75%. The figure reveals that most of the seats have a low level of dissatisfaction with the MV configuration, as the percentage of dissatisfied passengers is below 5%. This indicates that the MV configuration is effective in most of the aircraft cabin seats. However, there are a few seats where the PD for the passengers is relatively high, such as A3 and C7, which have dissatisfaction levels of 6.75% and 4.91%, respectively. The average PD for all seats in DV is 1.359%.

The dissatisfaction levels with the DV configuration range from 2.97% to 43.85% as demonstrated in Figure 6.2. It is evident from the figure that the DV configuration is not as effective as the MV configuration, as the PD of passengers is generally higher for most of the seats. The highest level of dissatisfaction is observed in seats A7 and C1, with dissatisfaction levels of 43.85% and 42.34%, respectively. The seats in the B and C series, except for B5, have relatively high dissatisfaction levels, ranging from 19.76% to 39.75%. On the other hand, the seats in the D series have a wide range of dissatisfaction levels, with some seats having a relatively low level of dissatisfaction, such as D1 with 2.98%, while others, such as D2 and D7 with 26.98% and 26.70%, have a relatively high level of dissatisfaction. The average PD for all seats in DV is 16.283%.

The PD for some seats increases with the addition of an extra outlet with the DV system, while the PD for other seats may drops as shown in Figure 6.2. As shown in Figure 6.2(c), in the C series, the PDs of C1, C2, C4, C6, and C7 are greater in DV with an additional outlet compared to the DV system. Meanwhile, there is an increase in the PDs of C3 and C5. This suggests that the extra outlet may not be effective in improving PD in some particular seats.

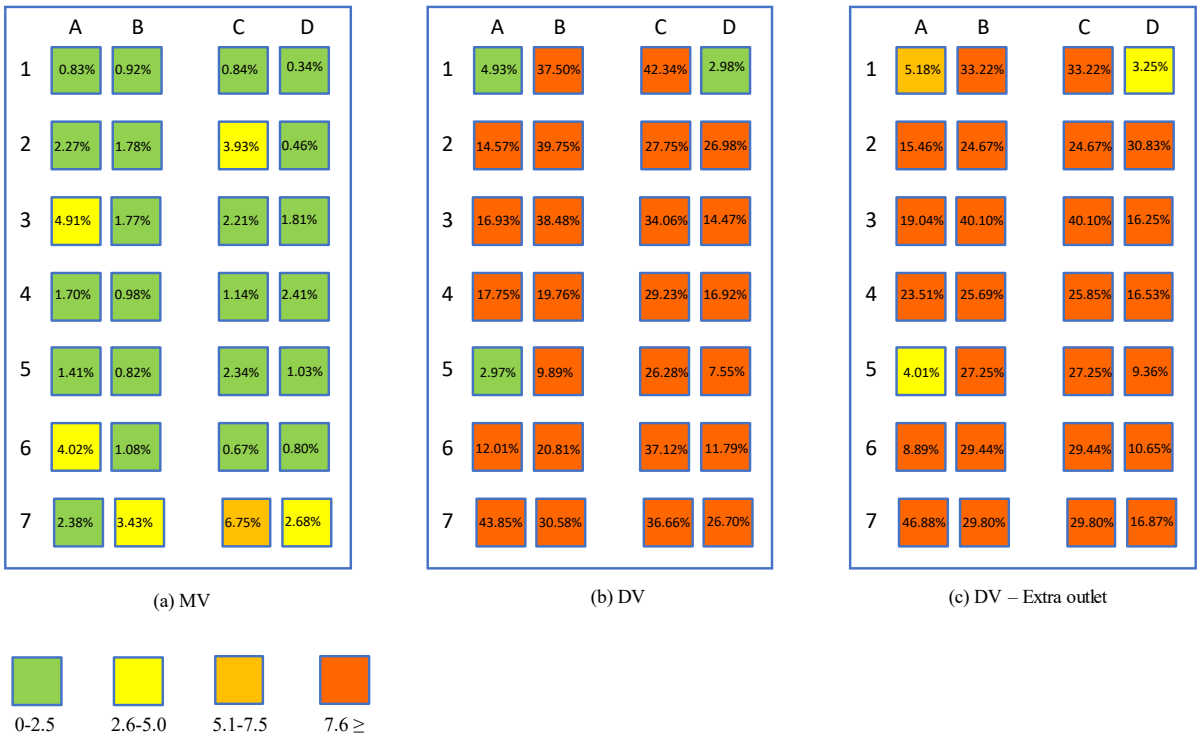

Figure 6.2. Percentage Dissatisfied (PD) for (a) MV, (b) DV, and (c) DV with extra outlet

Figure 6.3 shows the Draft Rate (DR) of MV, DV, and DV with extra outlets for different seats in an aircraft cabin. DR measures air movement and indicates the average air velocity experienced by a person sitting in a specific seat. When the DR value is higher, it results in increased air velocity and draft rate for the seat. The average DR in MV for all seats is approximately 3.98%. However, there is a significant variation in DR values among the seats, ranging from a low of 1.64% for seat D4 to a high of 9.89% for seat C6. Seats in the C and A series of the aircraft cabin tend to have higher DR values than those in the B and D series. This is due to differences in the air distribution system. Seat C6 has the highest DR value, while seats D3 and D4 have the lowest DR values.

On average, the DR in DV configuration for all seats is around 2.59%. The DR values in DV configuration among the seats vary significantly, with seat B7 having the lowest value of only 1.0% and seat D2 having the highest value of 3.71%. Seats in the B and D series of the aircraft cabin generally exhibit higher DR values compared to seats in the A and C series. It is noticeable

that the DR values for DV tend to be lower compared to MV, as DV uses a unique air supply approach near the floor.

It's important to mention that the DR values for displacement ventilation are generally lower than those for mixing ventilation. This is because displacement ventilation uses a unique air supply approach near the floor.

For MV, the average DR value is approximately 3.98%, while for DV, it is approximately 2.59%. This indicates that, on average, MV tends to provide higher air velocities and potentially higher levels of draft rate compared to DV. When it comes to MV configuration, the process typically involves mixing supply air with room air. As a result, the air velocities increase, and the distribution of air throughout the cabin becomes more consistent. In situations where uniform air distribution and higher air velocities are needed, MV could be a good option. However, if a lower air velocity is preferred to avoid drafts, DV may be the better choice.

For DV with an extra outlet, the average DR for all seats with the extra outlet is approximately 2.21%. The presence of an extra outlet with DV contributes to decreased DR. However, there is notable variation in the DR values among the seats, ranging from a low of 0.45% for seat C3 to a high of 4.21% for seat B1.

Figure 6.3. Draft Rate (DR) for (a) MV, (b) DV, and (c) DV with extra outlet

6.2. Infection Risk

Figure 6.4 demonstrates the infection risk scenarios for near-the-wall and near-aisle cough injection in the aircraft cabin. The scenarios include no mask, a surgical mask with 71.5% efficiency, a mask with 90% efficiency, and an N95 mask with 98% efficiency.

For near-wall cough injection in MV case as shown in Figure 6.4 the infection risk percentages range from 0% to 100% without any mask. The highest infection risk of 100% is observed in seat B4, indicating that this location is highly susceptible to infection from a near-wall cough injection without any protective measures. Several other seats, such as A5 (89.76%), B5 (75.35%), C4 (77.44%), C5 (93.94%), and D5 (73.37%), also exhibit relatively high infection risks. It is worth noting that the seats with the lowest infection risks, such as A6 (5.56%), A7 (0%), D7 (5.56%), and D6 (13.10%), still pose a negligible risk of infection.

When a surgical mask with an efficiency of 71.5% is worn, the infection risk percentages decrease significantly compared to the previous case. The highest infection risk now stands at 99.89% in

seat B4, which is still a concerning value. However, several other high-risk seats, such as A5 (47.77%), B5 (32.91%), C5 (55.03%), and D5(55.03%), demonstrate a noticeable reduction in airborne infection risk.

The infection risk decreases even further due to the utilization of an N95 mask with a higher efficiency of 98%. The highest infection risk remains in seat B4 (38.12%), but it is substantially lower compared to the previous cases. Similarly, seats A5 (4.46%), B5 (2.76%), and C5 (5.45%) experience significant reductions in infection risk. The N95 mask minimizes the risk of airborne transmission ensuring effective containment of respiratory droplets and aerosol because of its high filtration efficiency.

Figure 6.4. Infection risk for (a) MV (near wall cough injection) without mask (η=0), (b) MV (near wall cough injection) with surgical mask (η=0.715), (c) MV (near wall cough injection) with mask (η=0.9), and (d) MV (near wall cough injection) with N95 mask (η=0.98)

The seat close to the index person in the same row is still the most vulnerable to respiratory droplet transmission for the near aisle cough injection shown in Figure 6.5 similar to near-wall cough injection. The infection risk reduces in A5, B5, and D5 seats for the near-aisle cough injection which was more susceptible to infection for the near-wall index person.

The risk of infection is reduced in seats A5 (64.53%), B5 (69.07%), and D5 (52.70%) without wearing masks by the other passengers for near-aisle seated index person who were previously more susceptible to infection for the near-wall index person case. In general, rows 3-5 are prone to high to moderate risk. These seats are situated in areas where cough droplets can easily reach due to airflow patterns. Near aisle cough injection in MV configuration results in higher risks for C5 than near wall injection. Seats A7 (0%), B7 (0%), and C7(0%) exhibit negligible infection risks.

The usage of surgical and N95 masks reduces the infection risk tremendously. But it is noticeable that the seat (A4) close to the index person remains susceptible to infection. However, the infection risk is negligible for all passengers.

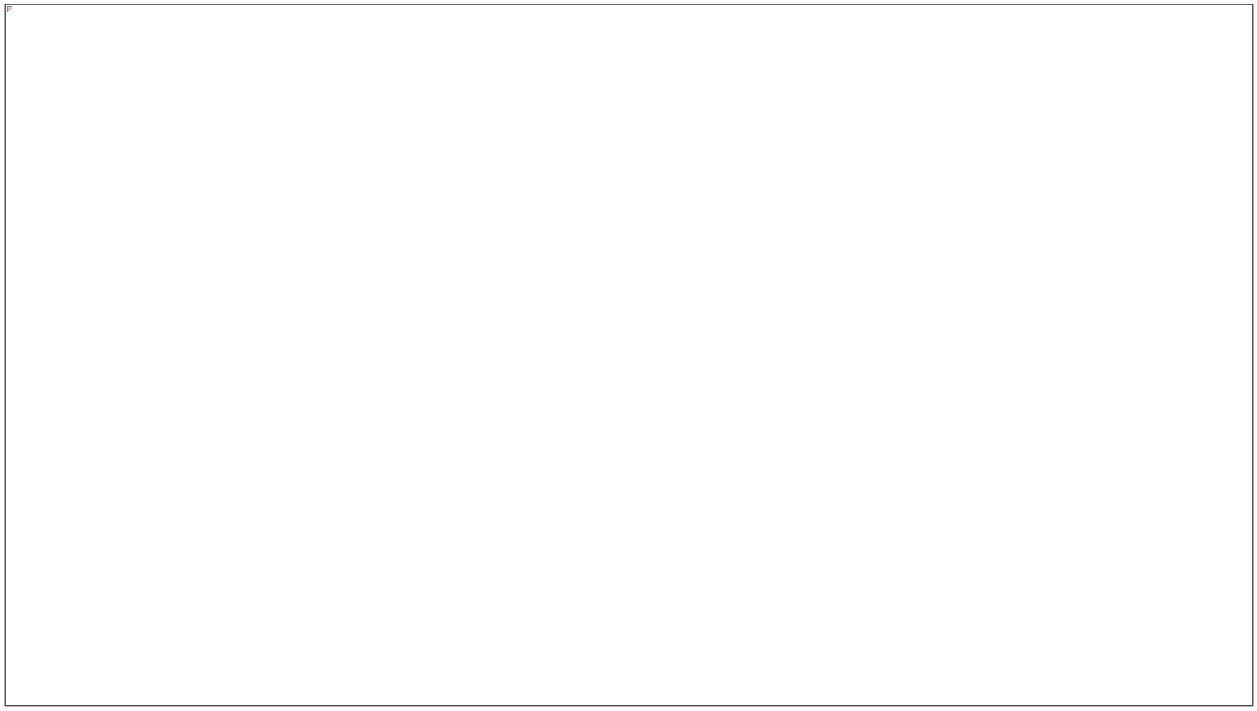

Figure 6.5. Infection risk for (a) MV (near-aisle cough injection) without mask (η=0), (b) MV (near-aisle cough injection) with surgical mask (η=0.715), (c) MV (near-aisle cough injection) with mask (η=0.9), and (d) MV (near-aisle cough injection) with N95 mask (η=0.98)

In Figure 6.6, the risk of infection from near-wall coughing in the aircraft cabin seats in the DV configuration is shown. The data is presented for both scenarios: without masks and with masks of varying efficiency levels. The infection risks for near-wall cough injection in DV show

similarities to the MV scenario for seat B4. Seats B4 continues to exhibit the highest infection risks of 100%, indicating their extreme vulnerability to respiratory droplet transmission. Additionally, seats A5, B5, C4, C5, and D5 remain high-risk seats in both scenarios of MV and DV, emphasizing their susceptibility to infection risk. It is worth noting that seats such as A1 (0%), B1 (0%), and D1 (0%) have effectively eliminated the associated risks. In the highly infectious zone, such as A5(87.12%), C5(78.88%), and D5 (66.51%), the risks are also reduced compared to the MV scenario. Conversely, some seats experience higher infection risks in the DV scenario compared to MV. Notably, seats B5 (99.87%), and C4 (90.57%) demonstrate higher risks in the DV setup. This variation is because of the different airflow patterns and ventilation strategies employed in DV, which affect the dispersion, deposition, and dilution of respiratory droplets and aerosol. Wearing surgical or N95 masks can reduce the risk of infection for the passenger near the index person (B4), but the risk is 30.46% higher compared to near-wall cough injection in MV.

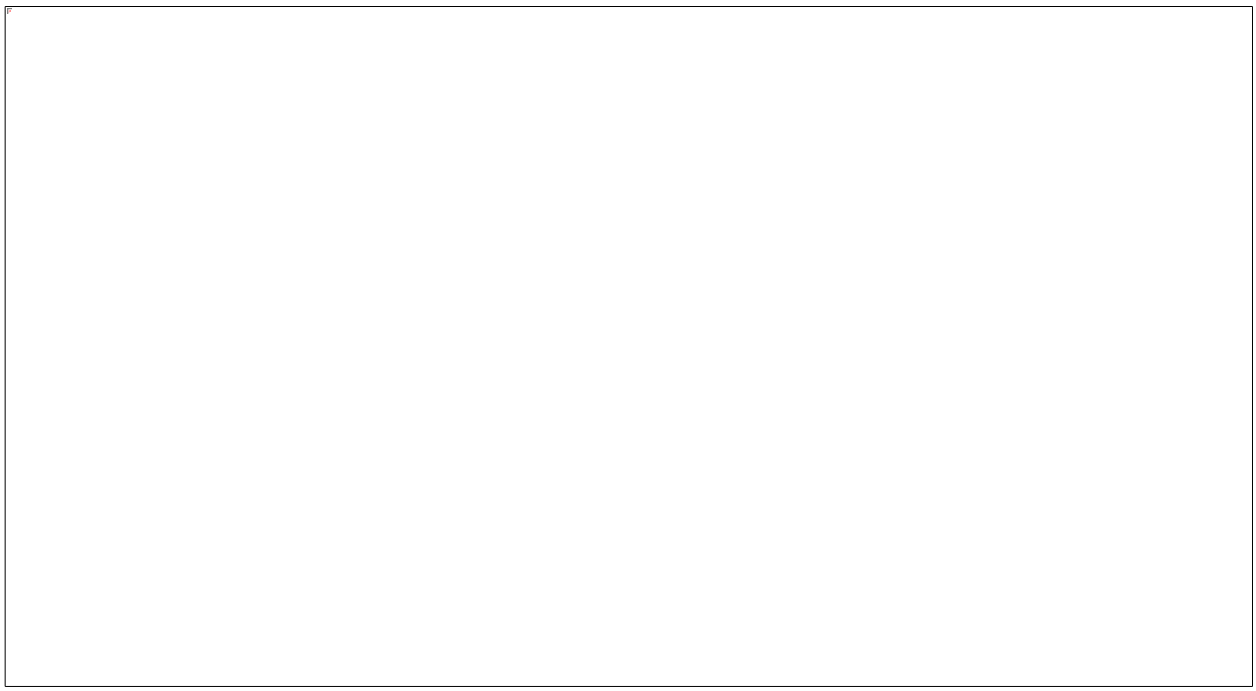

Figure 6.6. Infection risk for (a) DV (near wall cough injection) without mask (η=0), (b) DV (near wall cough injection) with surgical mask (η=0.715), (c) DV (near wall cough injection) with mask (η=0.9), and (d) DV (near wall cough injection) with N95 mask (η=0.98)

Figure 6.7 demonstrates the infection risk for a near-aisle coughing index person in the DV configuration. The infection risk is significantly low for the near aisle DV configuration than for

MV near aisle cough injection. The high infection zone is limited to only two seats without a mask; with a surgical mask, it reduces to one seat, and the risk for all passengers is negligible for an N95 mask. Seats A1, A2, A3, A6, A7, B1, B6, B7, C6, C7, D1, D6, and D7 have an infection risk of 0% without using any mask. The seats located in C4 and D4 present a high risk of infection, exceeding 90%. It is apparent that the individual seated next to the index person poses a 20.6% risk of infection when not wearing a mask. This risk was 100% for the near-aisle cough injection in MV configuration. The usage of surgical and N95 masks reduces the infection risk from 99.96% to 89.01% and 14.36% respectively.

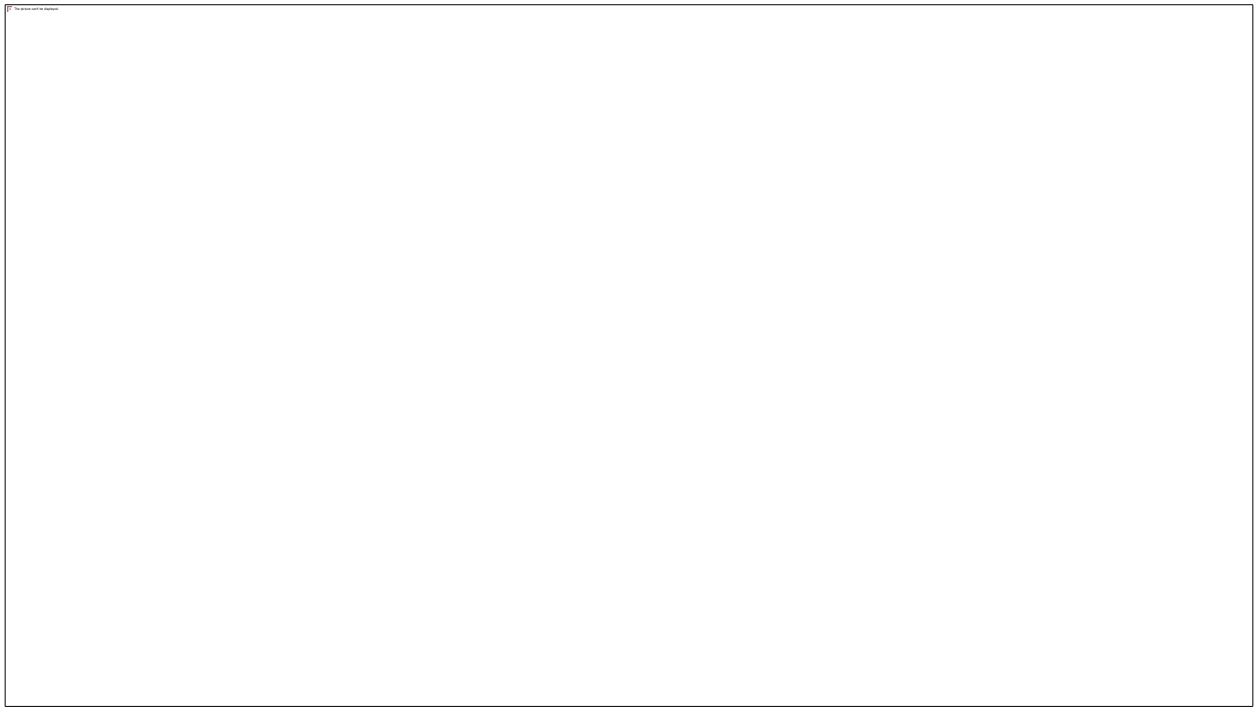

Figure 6.7. Infection risk for (a) DV (near aisle cough injection) without mask (η=0), (b) DV (near aisle cough injection) with surgical mask (η=0.715), (c) DV (near aisle cough injection) with mask (η=0.9), and (d) DV (near aisle cough injection) with N95 mask (η=0.98)

The effect of additional outlets in the DV system on the risk of airborne disease transmission is demonstrated in Figure 6.8. The additional outlet decreases the infection risk for A2, B2, A7, B7, D2, C7, and D7 seats without wearing a mask to 0%. These seats were previously in the lower infection zone having an infection risk lower than 25% without additional outlets. It has been found that certain seats, such as A5 (60.24%), B3 (25.00%), B5 (82.15%), and B6 (20.58%), have a higher risk of infection risk for the additional outlet without wearing the mask. However, seats in

the C and D series generally have a lower risk of infection, with the exception of C4. The additional outlet in the DV configuration raises the infection risk for B4 (35.88%) by 22.79% in the case of wearing an N95 mask.

Figure 6.8. Infection risk for (a) DV with extra outlet (near wall cough injection) without mask (η=0), (b) DV with extra outlet (near wall cough injection) with surgical mask (η=0.715), (c) DV with extra outlet (near wall cough injection) with mask (η=0.9), and (d) DV with extra outlet (near wall cough injection) with N95 mask (η=0.98)

Figure 6.9 demonstrates the effect of an extra outlet in DV configuration for the near aisle cough injection on the airborne infection risk. The incorporation of additional outlets nullifies the infection risk for A5, B2, and C1 seats without wearing any masks. However, it results in the creation of an elevated infectious risk zone for the third row. According to Figure 6.9, there are specific seats on which the risk of infection decreases. These seats include B5 (20.58%), C2 (5.56%), C4 (95.54%), D2 (20.59%), and D4 (82.25%). However, there are also seats in which the risk of infection increases, such as A3 (36.96%), B3 (85.87%), C3 (91.61%), D3 (60.07%), C6 (20.59%), D5 (36.93%), and D6 (20.59%). By wearing a surgical mask, the risk of infection for

seat C4 is reduced to 58.79%. However, using a more efficient mask like N95 can eliminate the risk altogether.

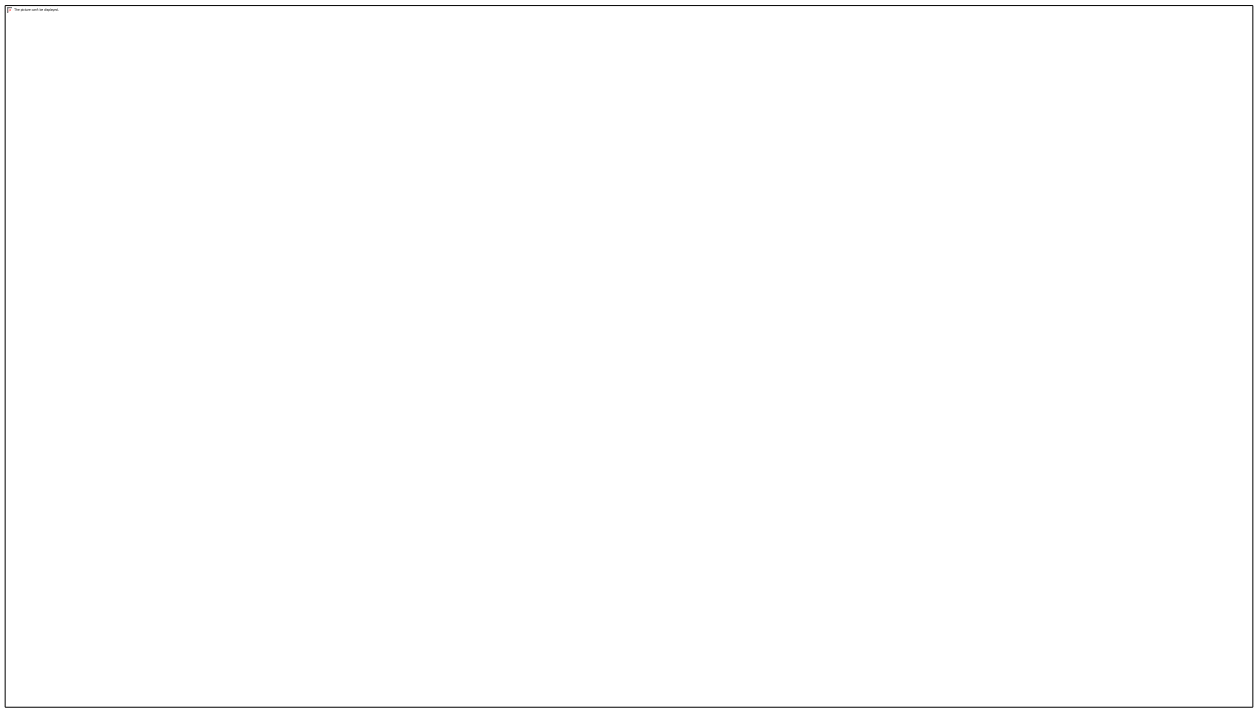

Figure 6.9. Infection risk for (a) DV with extra outlet (near aisle cough injection) without mask (η=0), (b) DV with extra outlet (near aisle cough injection) with surgical mask (η=0.715), (c) DV with extra outlet (near aisle cough injection) with mask (η=0.9), and (d) DV with extra outlet (near aisle cough injection) with N95 mask (η=0.98)

In Figure 6.10(a), the impact of mask filtration efficiency on the risk of infection over time of exposure is illustrated. As anticipated, the risk of airborne disease transmission infection increases with the duration of exposure, as depicted in Figure 6.10(a). The N95 mask with an efficiency rating of 98% has proven to significantly reduce the spatiotemporal infection risk, even with high exposure time.

Additionally, Figure 6.10(b) indicates how the $TCID_{50}$ affects the likelihood of infection with respect to viral load. The Median Tissue Culture Infectious Dose ($TCID_{50}$) refers to the amount of virus particles needed to infect 50% of a given tissue culture. Lower $TCID_{50}$ causes a greater risk

of infection due to a higher concentration of infectious particles. This is because a smaller amount of the virus is needed to cause infection when the $TCID_{50}$ is lower. The infection probability is significantly higher for lower $TCID_{50}$. In terms of infection probability, a higher $TCID_{50}$ (i.e., 100000) with a higher viral load poses almost negligible risk to susceptible passengers, whereas a lower $TCID_{50}$ of 1000 at a viral load of 6×10^{9} copies/mL results in a 100% infection probability.

Figure 6.10. Effect of (a) exposure time and (b) viral load on infection probability

6.3. Conclusion

In conclusion, the comprehensive analysis of key parameters such as Heat Removal Efficiency (HRE), Velocity Non-Uniformity Index (VNUI), Temperature Non-Uniformity Index (TNU), Percentage Dissatisfied (PD), Draft Rate (DR), and Airborne Disease Transmission Infection Risk provides valuable insights into the performance of aircraft cabin environments. The study highlights the superiority of Displacement Ventilation (DV) over Mixing Ventilation (MV) in terms of HRE, with DV showing a 68.9% higher efficiency. DV's stratified airflow pattern reduces air recirculation, potentially limiting the spread of respiratory aerosols and improving indoor air quality. However, DV may lead to uneven air velocity distribution and temperature non-uniformity compared to MV. PD analysis reveals that MV generally provides more even airflow and thermal comfort, with lower dissatisfaction levels than DV. Additionally, DV with an extra outlet can impact airflow distribution and PD in certain seats. The infection risk analysis

demonstrates that DV configurations generally reduce infection risks compared to MV, with DV near-aisle cough injection showing significantly lower risks. In addition to the findings highlighted above, the study also reveals the impact of additional outlets on DV performance, indicating that while extra outlets can improve HRE, they may also lead to increased air recirculation and potential discomfort for passengers in certain seating areas. Furthermore, the analysis of Draft Rate (DR) shows that DV generally results in lower draft rate compared to MV, which is crucial for passenger comfort. The infection risk assessment provides valuable insights into the effectiveness of different ventilation configurations and mask types in reducing the risk of airborne disease transmission. It is evident that wearing masks, especially N95 masks, can significantly reduce infection risks, highlighting the importance of mask-wearing policies in mitigating the spread of airborne diseases in aircraft cabins. The study's findings can inform the development of guidelines and strategies for improving cabin air quality and passenger safety, ultimately benefiting both passengers and the aviation industry as a whole. The study underscores the importance of ventilation strategies and mask efficiency in mitigating airborne disease transmission, offering insights for improving cabin design and operation for the aviation industry.

Chapter 7
Conclusion And Recommendation

7.1. Conclusions

Three-dimensional Eulerian-Lagrangian multiphase CFD simulations were conducted to figure out the dispersion, deposition, and transport of cough aerosol in an UME, DME, and aircraft cabin. A two-way coupling approach was employed to understand the complex cough droplet evaporation process. The following sections list the findings from these studies.

7.1.1. Escalator

The cough droplets expelled from the mouth entered the recirculation zones near steps via the upper portion of the shoulder and wake zone behind the torso. For UME, most of the larger droplets are found in front of the trajectories but a few larger droplets are found in the wake zone behind the torso if the RH is high. The opposite was found in the DME. Higher penetration length was observed with higher operational speed and lower RH. UME demonstrated higher droplet penetration length than DME. The droplets contaminated the lower portion of the human body at a lower operational speed if another passenger stood two steps behind the infected person in UME. Conversely, if a passenger is two steps behind an infected person in a DME, the whole body is contaminated. The hand railings were one of the most potentially contaminated surfaces by the expelled respiratory droplets. Higher operational speed and lower RH demonstrated higher evaporation during the injection period ($0 – 0.5\ s$) and no common patterns were found during the rest of the time when aerosol entered the wake zone. Aerosol concentration was found lower at 0.4 *m/s* and 0.7 *m/s* operational speed in 54% RH. Coalescence was found frequently in the wake zone and recirculation zone near the steps. GA demonstrated that higher operational speed and lower RH were responsible for lower concentration with higher penetration length. In comparison to DME, more deposition was seen with UME.

7.1.2. Aircraft cabin

A spatiotemporal infection risk model was utilized for the assessment of airborne disease transmission risk by modeling the virus-laden aerosol using CFD from the coughing in a single-aisle aircraft cabin. This infection risk model incorporates some biomedical factors such as viral load, $TCID_{50}$, and pulmonary ventilation rate. The effect of PPE worn by susceptible passengers with different efficiencies and index person locations (near-wall and near-aisle) was assessed for the MV, DV, and DV with extra outlets ventilation configurations. Additionally, the VNUI, TNUI, HRE, PD, and DR were used to evaluate the ventilation effectiveness of these three ventilation configuration types. The HRE of DV is 68.9% higher compared to MV. The highest VNUI value was found in DV with a value of 0.731. Extra outlets in the DV system lower the VNUI while these do not affect TNUI. PD was found lower for MV compared to DV with a range between 0.34% to 6.75%. the additional outlets do not effectively enhance PD for particular seats in DV. The average DR in MV for all seats is approximately 3.98% whereas it is around 2.59% for DV configuration. The location of the index passenger affects the aerosol dispersion in the cabin resulting in different infection risk maps. The closest seat to the index person in the same row is the most susceptible to infection risk both for near-wall and near-aisle cough injection in MV configuration and for near-wall cough injection in DV configuration. But the near-aisle seat shows the highest risk for near-aisle cough injection in DV configuration. Highly efficient masks such as N95 can reduce the infection risk significantly for all cases. However, the closest passenger to the index person in the same row is still susceptible to risk by wearing N95 masks for near-wall cough injection in MV and DV, and near-aisle cough injection in DV. Highly infectious zones are in the same row seated with the index person and the back from the index person for MV near-wall and near-aisle injections. In the near-wall MV cough injection, the highly infectious zones decrease while the medium infectious zones increase. The infection risk is negligible for the first two columns containing the index person in the near-aisle DV configuration. However, the risk for near wall DV system is decreased for some seats, whereas it is increased for other few seats. In general, DV shows a lower infection risk for susceptible passengers with higher HRE and dissatisfaction for the passengers. The increase in exposure time and viral load causes an increase in infection risk. However, a higher $TCID_{50}$ and better mask efficiency can decrease the risk of infection.

7.2. Recommendation for future work

Human movement can affect aerosol transport which is not considered in this study. Further study can be performed considering more passengers with and without movement beside and behind the index passenger. The study of the effects of passenger spacing and crowd dynamics on aerosol transmission can also be approached. The risk of infection needs to be measured in other aircraft cabins, like double aisles. More research is required to determine the impact of a few other variables, such as the movement of cabin crew and the inclination of the chairs, on aerosol transmission throughout the cabin. Other situations, such as sneezing or coughing while standing or moving, may be of interest for future investigations. It is recommended to conduct experimental validation of the computational models used in this study. This could involve setting up physical mock-ups using thermal manikins and using test facilities to replicate cabin environments and different airflow conditions. Additionally, investigating the impact of different seating arrangements, such as seating density, configurations, and the use of barriers between seats, on airflow patterns and infection risk could provide valuable insights for optimizing cabin layouts. Furthermore, integrating real-time monitoring systems for air quality and passenger movements could enable a more dynamic and adaptive approach to cabin ventilation and disease prevention. Investigation of various risk mitigation techniques, for example using UV-C irradiation, air purifier, or other interventions need to be well explored to lessen the transmission of aerosols in the indoor environments. Advanced filtration technologies and air purification systems along with novel materials for cabin interiors can be explored. These may offer additional layers of protection against airborne pathogens. Investigating the use of novel materials for cabin interiors that have antimicrobial or antiviral properties could also help in reducing the risk of disease transmission. These materials could be used for surfaces that are frequently touched by passengers, such as passenger armrests, tray tables, and seat backs, to help prevent the spread of infectious pathogens. Epidemiological studies can figure out the actual risk of airborne disease transmission in these indoor environments.

References

1. Zhang J, Litvinova M, Wang W, et al (2020) Evolving epidemiology and transmission dynamics of coronavirus disease 2019 outside Hubei province, China: a descriptive and modelling study. Lancet Infect Dis 20:793–802. https://doi.org/10.1016/S1473-3099(20)30230-9

2. Zhu H, Wei L, Niu P (2020) The novel coronavirus outbreak in Wuhan, China. Glob Health Res Policy 5:1–3. https://doi.org/10.1186/S41256-020-00135-6

3. Chia PY, Coleman KK, Tan YK, et al (2020) Detection of air and surface contamination by SARS-CoV-2 in hospital rooms of infected patients. Nature Communications 2020 11:1 11:1–7. https://doi.org/10.1038/s41467-020-16670-2

4. Guo ZD, Wang ZY, Zhang SF, et al (2020) Aerosol and Surface Distribution of Severe Acute Respiratory Syndrome Coronavirus 2 in Hospital Wards, Wuhan, China, 2020. Emerg Infect Dis 26:1586. https://doi.org/10.3201/EID2607.200885

5. Hinds WC (1999) Aerosol technology: properties, behavior, and measurement of airborne particles. John Wiley & Sons

6. Heyder J (2009) Definition of an Aerosol. Journal of Aerosol Medicine 4:217–221. https://doi.org/10.1089/JAM.1991.4.217

7. Bourouiba L, Dehandschoewercker E, Bush JWM (2014) Violent expiratory events: on coughing and sneezing. J Fluid Mech 745:537–563. https://doi.org/10.1017/JFM.2014.88

8. Tellier R (2006) Review of Aerosol Transmission of Influenza A Virus. Emerg Infect Dis 12:1657. https://doi.org/10.3201/EID1211.060426

9. Thomas RJ (2013) Particle size and pathogenicity in the respiratory tract. Virulence 4:847–858. https://doi.org/10.4161/VIRU.27172

10. Aliabadi AA, Rogak SN, Bartlett KH, Green SI (2011) Preventing Airborne Disease Transmission: Review of Methods for Ventilation Design in Health Care Facilities. Adv Prev Med 2011:1–21. https://doi.org/10.4061/2011/124064

11. Chirico F, Sacco A, Bragazzi NL, Magnavita N (2020) Can Air-Conditioning Systems Contribute to the Spread of SARS/MERS/COVID-19 Infection? Insights from a Rapid Review of the Literature. Int J Environ Res Public Health 17:6052. https://doi.org/10.3390/IJERPH17176052

12. Greenhalgh T, Jimenez JL, Prather KA, et al (2021) Ten scientific reasons in support of airborne transmission of SARS-CoV-2. The Lancet 397:1603–1605. https://doi.org/10.1016/S0140-6736(21)00869-2

13. Vejerano EP, Marr LC (2018) Physico-chemical characteristics of evaporating respiratory fluid droplets. J R Soc Interface 15:. https://doi.org/10.1098/RSIF.2017.0939

14. Spicer SS, Martinez JR (1984) Mucin biosynthesis and secretion in the respiratory tract. Environ Health Perspect 55:193–204. https://doi.org/10.1289/EHP.8455193

15. Bansil R, Turner BS (2006) Mucin structure, aggregation, physiological functions and biomedical applications. Curr Opin Colloid Interface Sci 11:164–170. https://doi.org/10.1016/J.COCIS.2005.11.001

16. Nicas M, Nazaroff WW, Hubbard A (2010) Toward Understanding the Risk of Secondary Airborne Infection: Emission of Respirable Pathogens. J Occup Environ Hyg 2:143–154. https://doi.org/10.1080/15459620590918466

17. Scharfman BE, Techet AH, Bush JWM, Bourouiba L (2016) Visualization of sneeze ejecta: steps of fluid fragmentation leading to respiratory droplets. Exp Fluids 57:1–9. https://doi.org/10.1007/S00348-015-2078-4/FIGURES/10

18. Schipper RG, Silletti E, Vingerhoeds MH (2007) Saliva as research material: Biochemical, physicochemical and practical aspects. Arch Oral Biol 52:1114–1135. https://doi.org/10.1016/J.ARCHORALBIO.2007.06.009

19. Zhu SW, Kato S, Yang JH (2006) Study on transport characteristics of saliva droplets produced by coughing in a calm indoor environment. Build Environ 41:1691–1702. https://doi.org/10.1016/J.BUILDENV.2005.06.024

20. Zhu N, Zhang D, Wang W, et al (2020) A Novel Coronavirus from Patients with Pneumonia in China, 2019. New England Journal of Medicine 382:727–733. https://doi.org/10.1056/NEJMOA2001017/SUPPL_FILE/NEJMOA2001017_DISCLOSURES.PDF

21. Gralton J, Tovey E, McLaws ML, Rawlinson WD (2011) The role of particle size in aerosolised pathogen transmission: A review. Journal of Infection 62:1–13. https://doi.org/10.1016/J.JINF.2010.11.010

22. Anand S, Mayya YS (2020) Size distribution of virus laden droplets from expiratory ejecta of infected subjects. Sci Rep 10:1–9. https://doi.org/10.1038/s41598-020-78110-x

23. Duguid JP (1946) The size and the duration of air-carriage of respiratory droplets and droplet-nuclei. Epidemiol Infect 44:471–479. https://doi.org/10.1017/S0022172400019288

24. Lee J, Yoo D, Ryu S, et al (2019) Quantity, Size Distribution, and Characteristics of Cough-generated Aerosol Produced by Patients with an Upper Respiratory Tract Infection. Aerosol Air Qual Res 19:840–853. https://doi.org/10.4209/AAQR.2018.01.0031

25. Chao CYH, Wan MP, Morawska L, et al (2009) Characterization of expiration air jets and droplet size distributions immediately at the mouth opening. J Aerosol Sci 40:122–133. https://doi.org/10.1016/J.JAEROSCI.2008.10.003

26. Mui KW, Wong LT, Wu CL, Lai ACK (2009) Numerical modeling of exhaled droplet nuclei dispersion and mixing in indoor environments. J Hazard Mater 167:736–744. https://doi.org/10.1016/J.JHAZMAT.2009.01.041

27. Zhao B, Zhang Z, Li X (2005) Numerical study of the transport of droplets or particles generated by respiratory system indoors. Build Environ 40:1032–1039. https://doi.org/10.1016/J.BUILDENV.2004.09.018

28. Bahl P, Silva CM de, Chughtai AA, et al (2020) An experimental framework to capture the flow dynamics of droplets expelled by a sneeze. Experiments in Fluids 2020 61:8 61:1–9. https://doi.org/10.1007/S00348-020-03008-3

29. Bahl P, Silva CM de, Chughtai AA, et al (2020) An experimental framework to capture the flow dynamics of droplets expelled by a sneeze. Exp Fluids 61:1–9. https://doi.org/10.1007/S00348-020-03008-3

30. Gupta JK, Lin CH, Chen Q (2009) Flow dynamics and characterization of a cough. Indoor Air 19:517–525. https://doi.org/10.1111/J.1600-0668.2009.00619.X

31. Judson SD, Munster VJ (2019) Nosocomial Transmission of Emerging Viruses via Aerosol-Generating Medical Procedures. Viruses 11:940. https://doi.org/10.3390/V11100940

32. Cowling BJ, Ip DKM, Fang VJ, et al (2013) Aerosol transmission is an important mode of influenza A virus spread. Nat Commun 4:1–6. https://doi.org/10.1038/ncomms2922

33. How Coronavirus Spreads. https://www.cdc.gov/coronavirus/2019-ncov/prevent-getting-sick/how-covid-spreads.html. Accessed 18 Jul 2021

34. Morawska L, Cao J (2020) Airborne transmission of SARS-CoV-2: The world should face the reality. Environ Int 139:105730. https://doi.org/10.1016/J.ENVINT.2020.105730

35. L L, J W, Y L, A O (2017) Evaporation and dispersion of respiratory droplets from coughing. Indoor Air 27:179–190. https://doi.org/10.1111/INA.12297

36. Bourouiba L (2016) A Sneeze. New England Journal of Medicine 375:e15. https://doi.org/10.1056/NEJMICM1501197

37. Parienta D, Morawska L, Johnson GR, et al (2011) Theoretical analysis of the motion and evaporation of exhaled respiratory droplets of mixed composition. J Aerosol Sci 42:1–10. https://doi.org/10.1016/J.JAEROSCI.2010.10.005

38. Beggs CB (2016) The Airborne Transmission of Infection in Hospital Buildings: Fact or Fiction?: http://dx.doi.org/101177/1420326X03012001002 12:9–18. https://doi.org/10.1177/1420326X03012001002

39. Wells WF On air-borne infection: study II droplets and droplet nuclei. Am J Epidemiol 20:611–618

40. Tan ZP, Silwal L, Bhatt SP, Raghav V (2021) Experimental characterization of speech aerosol dispersion dynamics. Sci Rep 11:1–12. https://doi.org/10.1038/s41598-021-83298-7

41. Asadi S, Wexler AS, Cappa CD, et al (2019) Aerosol emission and superemission during human speech increase with voice loudness. Sci Rep 9:1–10. https://doi.org/10.1038/s41598-019-38808-z

42. Asadi S, Wexler AS, Cappa CD, et al (2020) Effect of voicing and articulation manner on aerosol particle emission during human speech. PLoS One 15:e0227699. https://doi.org/10.1371/JOURNAL.PONE.0227699

43. Riley EC, Murphy G, Riley RL (1978) AIRBORNE SPREAD OF MEASLES IN A SUBURBAN ELEMENTARY SCHOOL. Am J Epidemiol 107:421–432. https://doi.org/10.1093/OXFORDJOURNALS.AJE.A112560

44. Li X, Lester D, Rosengarten G, et al (2022) A spatiotemporally resolved infection risk model for airborne transmission of COVID-19 variants in indoor spaces. Science of The Total Environment 812:152592. https://doi.org/10.1016/J.SCITOTENV.2021.152592

45. Li Y, Qian H, Hang J, et al (2021) Probable airborne transmission of SARS-CoV-2 in a poorly ventilated restaurant. Build Environ 196:107788. https://doi.org/10.1016/J.BUILDENV.2021.107788

46. Mirzaie M, Lakzian E, Khan A, et al (2021) COVID-19 spread in a classroom equipped with partition – A CFD approach. J Hazard Mater 420:126587. https://doi.org/10.1016/J.JHAZMAT.2021.126587

47. Zhang Y, Feng G, Kang Z, et al (2017) Numerical Simulation of Coughed Droplets in Conference Room. Procedia Eng 205:302–308. https://doi.org/10.1016/J.PROENG.2017.09.981

48. Dbouk T, Drikakis D (2021) On airborne virus transmission in elevators and confined spaces. Physics of Fluids 33:011905. https://doi.org/10.1063/5.0038180

49. Duchaine F, Cizeron M, Odier N, et al (2022) High-performance CFD for Respiratory Droplet Turbulent Dispersion in a Ventilated City Bus. International Journal of Computational Fluid Dynamics 35:758–777. https://doi.org/10.1080/10618562.2021.1989421

50. Fišer J, Jícha M (2013) Impact of air distribution system on quality of ventilation in small aircraft cabin. Build Environ 69:171–182. https://doi.org/10.1016/J.BUILDENV.2013.08.007

51. Zhang T, Chen Q (Yan) (2007) Novel air distribution systems for commercial aircraft cabins. Build Environ 42:1675–1684. https://doi.org/10.1016/J.BUILDENV.2006.02.014

52. Pang L, Xu J, Fang L, et al (2013) Evaluation of an improved air distribution system for aircraft cabin. Build Environ 59:145–152. https://doi.org/10.1016/J.BUILDENV.2012.08.015

53. Nielsen PV (1988) Displacement ventilation in a room with low-level diffusers. Dept. of Building Technology and Structural Engineering, Aalborg University, Aalborg

54. Corgnati SP, Perino M, Fracastoro G V., Nielsen P V. (2009) Experimental and numerical analysis of air and radiant cooling systems in offices. Build Environ 44:801–806. https://doi.org/10.1016/J.BUILDENV.2008.05.022

55. Bosbach J, Lange S, Dehne T, et al (2013) Alternative ventilation concepts for aircraft cabins. CEAS Aeronaut J 4:301To – 313. https://doi.org/10.1007/s13272-013-0074-z

56. (2013) ANSI/ASHRAE Standard 161-2013 Air Quality within Commercial Aircraft

57. Dehne T, Bosbach J, Heider A (2014) Comparison of surface temperatures and cooling rates for different ventilation concepts in an A320 aircraft cabin under flight conditions. In: RoomVent 2014: Proceedings of the 13th CSCANVAC international conference on air distribution in rooms. pp 19–22

58. Zhang Y, Liu J, Pei J, et al (2017) Performance evaluation of different air distribution systems in an aircraft cabin mockup. Aerosp Sci Technol 70:359–366. https://doi.org/10.1016/J.AST.2017.08.009

59. Kaczmarczyk J, Melikov A, Fanger PO (2004) Human response to personalized ventilation and mixing ventilation. Indoor Air 14:17–29. https://doi.org/10.1111/J.1600-0668.2004.00300.X

60. Zhang TT, Li P, Wang S (2012) A personal air distribution system with air terminals embedded in chair armrests on commercial airplanes. Build Environ 47:89–99. https://doi.org/10.1016/J.BUILDENV.2011.04.035

61. Nagda NL, Rector HE (2003) A critical review of reported air concentrations of organic compounds in aircraft cabins. Indoor Air 13:292–301. https://doi.org/10.1034/J.1600-0668.2003.00202.X

62. Michaelis S (2011) Contaminated aircraft cabin air. J Biol Phys Chem 11:132–145. https://doi.org/10.4024/24MI11A.jbpc.11.04

63. Bischof W (1973) Ozone measurements in jet airliner cabin air. Water Air Soil Pollut 2:3–14. https://doi.org/10.1007/BF00572385

64. Spengler JD, Ludwig S, Weker RA (2004) Ozone exposures during trans-continental and trans-Pacific flights. Indoor Air 14:67–73. https://doi.org/10.1111/J.1600-0668.2004.00275.X

65. National Research Council, Division on Earth and Life Studies, Board on Environmental Studies and Toxicology, Committee on Air Quality in Passenger Cabins of Commercial Aircraft (2002) The airliner cabin environment and the health of passengers and crew. National Academy Press

66. Hunt EHH, Reid DHR, Space DR, Tilton FE (1995) Commercial airliner environmental control system. In: Aerospace Medical Association annual meeting. Anaheim, California

67. Bekö G, Allen JG, Weschler CJ, et al (2015) Impact of Cabin Ozone Concentrations on Passenger Reported Symptoms in Commercial Aircraft. PLoS One 10:. https://doi.org/10.1371/JOURNAL.PONE.0128454

68. Bhangar S, Cowlin SC, Singer BC, et al (2008) Ozone levels in passenger cabins of commercial aircraft on North American and transoceanic routes. Environ Sci Technol 42:3938–3943. https://doi.org/10.1021/ES702967K/SUPPL_FILE/ES702967K-FILE003.PDF

69. Walkinshaw DS;, ENG P; (2020) A Brief Introduction To Passenger Aircraft Cabin Air Quality. ASHRAE J 12–16

70. Singer BC, Zhao H, Preble C V., et al (2022) Measured influence of overhead HVAC on exposure to airborne contaminants from simulated speaking in a meeting and a classroom. Indoor Air 32:e12917. https://doi.org/10.1111/INA.12917

71. Yin Y, Xu W, Gupta J, et al (2009) Experimental study on displacement and mixing ventilation systems for a patient ward. HVAC and R Research 15:1175–1191. https://doi.org/10.1080/10789669.2009.10390885

72. Chung KC, Hsu SP (2001) Effect of ventilation pattern on room air and contaminant distribution. Build Environ 36:989–998. https://doi.org/10.1016/S0360-1323(00)00051-2

73. Qian H, Li Y, Nielsen P V., Hyldgaard CE (2008) Dispersion of exhalation pollutants in a two-bed hospital ward with a downward ventilation system. Build Environ 43:344–354. https://doi.org/10.1016/J.BUILDENV.2006.03.025

74. Escombe AR, Oeser CC, Gilman RH, et al (2007) Natural Ventilation for the Prevention of Airborne Contagion. PLoS Med 4:e68. https://doi.org/10.1371/JOURNAL.PMED.0040068

75. Olsen SJ, Chang H-L, Cheung TY-Y, et al (2003) Transmission of the Severe Acute Respiratory Syndrome on Aircraft. New England Journal of Medicine 349:2416–2422. https://doi.org/10.1056/NEJMOA031349

76. Zee M, Davis AC, Clark AD, et al (2021) Computational fluid dynamics modeling of cough transport in an aircraft cabin. Sci Rep 11:1–10. https://doi.org/10.1038/s41598-021-02663-8

77. Silcott D, Kinahan S, Santarpia J, et al (2020) RANSCOM/AMC commercial aircraft cabin aerosol dispersion tests

78. Isukapalli SS, Mazumdar S, George P, et al (2013) Computational fluid dynamics modeling of transport and deposition of pesticides in an aircraft cabin. Atmos Environ 68:198–207. https://doi.org/10.1016/J.ATMOSENV.2012.11.019

79. Zhang M, Yu N, Zhang Y, et al (2021) Numerical Simulation of the Novel Coronavirus Spread in Commercial Aircraft Cabin. Processes 9:1601. https://doi.org/10.3390/PR9091601

80. Mirikar D, Palanivel S, Arumuru V (2021) Droplet fate, efficacy of face mask, and transmission of virus-laden droplets inside a conference room. Physics of Fluids 33:065108. https://doi.org/10.1063/5.0054110

81. Curtius J, Granzin M, Schrod J (2021) Testing mobile air purifiers in a school classroom: Reducing the airborne transmission risk for SARS-CoV-2. Aerosol Science and Technology 55:586–599. https://doi.org/10.1080/02786826.2021.1877257/SUPPL_FILE/UAST_A_1877257_SM7182.PDF

82. Abuhegazy M, Talaat K, Anderoglu O, et al (2020) Numerical investigation of aerosol transport in a classroom with relevance to COVID-19. Physics of Fluids 32:103311. https://doi.org/10.1063/5.0029118

83. Arjmandi H, Amini R, khani F, Fallahpour M (2022) Minimizing the respiratory pathogen transmission: Numerical study and multi-objective optimization of ventilation systems in a

classroom. Thermal Science and Engineering Progress 28:101052. https://doi.org/10.1016/J.TSEP.2021.101052

84. Arma Khan (2022) A Numerical Modelling Approach to Study the Impact of Ventilation Configurations on Airborne Transmission in Indoor Environments. York University

85. Kishon Webb (2023) Aerosol Transmission of Covid-19 and Other Airborne Diseases in Office Environments Using Computational Fluid Dynamic Modeling and Machine Learning. York University

86. Wu L, Liu X, Yao F, Chen Y (2021) Numerical study of virus transmission through droplets from sneezing in a cafeteria. Physics of Fluids 33:023311. https://doi.org/10.1063/5.0040803

87. Shao S, Zhou D, He R, et al (2021) Risk assessment of airborne transmission of COVID-19 by asymptomatic individuals under different practical settings. J Aerosol Sci 151:105661. https://doi.org/10.1016/J.JAEROSCI.2020.105661

88. Park S, Choi Y, Song D, Kim EK (2021) Natural ventilation strategy and related issues to prevent coronavirus disease 2019 (COVID-19) airborne transmission in a school building. Science of The Total Environment 789:147764. https://doi.org/10.1016/J.SCITOTENV.2021.147764

89. Talaat K, Abuhegazy M, Mahfoze OA, et al (2021) Simulation of aerosol transmission on a Boeing 737 airplane with intervention measures for COVID-19 mitigation. Physics of Fluids 33:033312. https://doi.org/10.1063/5.0044720

90. Schoen LJ (2020) Guidance for building operations during the COVID-19 pandemic. ASHRAE J 5:

91. Seppänen O, Fisk WJ (2002) Association of ventilation system type with SBS symptoms in office workers. Indoor Air 12:98–112. https://doi.org/10.1034/j.1600-0668.2002.01111.x

92. Yang Y, Zhang H, Nunayon SS, et al (2018) Disinfection efficacy of ultraviolet germicidal irradiation on airborne bacteria in ventilation ducts. Indoor Air 28:806–817. https://doi.org/10.1111/INA.12504

93. Ryan RM, Wilding GE, Wynn RJ, et al (2011) Effect of enhanced ultraviolet germicidal irradiation in the heating ventilation and air conditioning system on ventilator-associated pneumonia in a neonatal intensive care unit. Journal of Perinatology 2011 31:9 31:607–614. https://doi.org/10.1038/jp.2011.16

94. Sung M, Kato S (2010) Method to evaluate UV dose of upper-room UVGI system using the concept of ventilation efficiency. Build Environ 45:1626–1631. https://doi.org/10.1016/J.BUILDENV.2010.01.011

95. Pavelchak N, DePersis RP, London M, et al (2000) Identification of Factors That Disrupt Negative Air Pressurization of Respiratory Isolation Rooms. Infect Control Hosp Epidemiol 21:191–195. https://doi.org/10.1086/501742

96. Liu S, Koupriyanov M, Paskaruk D, et al (2022) Investigation of airborne particle exposure in an office with mixing and displacement ventilation. Sustain Cities Soc 79:103718. https://doi.org/10.1016/J.SCS.2022.103718

97. Ong SWX, Tan YK, Chia PY, et al (2020) Air, surface environmental, and personal protective equipment contamination by severe acute respiratory syndrome coronavirus 2 (SARS-CoV-2) from a symptomatic patient. JAMA 323:. https://doi.org/https://doi.org/10.1001/jama.2020.3227

98. van Doremalen N, Bushmaker T, Morris DH, et al (2020) Aerosol and Surface Stability of SARS-CoV-2 as Compared with SARS-CoV-1. New England Journal of Medicine 382:1564–1567. https://doi.org/10.1056/NEJMC2004973/SUPPL_FILE/NEJMC2004973_DISCLOSURES.PDF

99. Walker CM, Ko G (2007) Effect of ultraviolet germicidal irradiation on viral aerosols. Environ Sci Technol 41:5460–5465. https://doi.org/10.1021/ES070056U/SUPPL_FILE/ES070056USI20070422_114454.PDF

100. Raeiszadeh M, Adeli B (2020) A Critical Review on Ultraviolet Disinfection Systems against COVID-19 Outbreak: Applicability, Validation, and Safety Considerations. ACS Photonics 7:2941–2951. https://doi.org/10.1021/ACSPHOTONICS.0C01245

101. Cole EC, Cook CE (1998) Characterization of infectious aerosols in health care facilities: An aid to effective engineering controls and preventive strategies. Am J Infect Control 26:453–464. https://doi.org/10.1016/S0196-6553(98)70046-X

102. Shimoda H, Matsuda J, Iwasaki T, Hayasaka D (2021) Efficacy of 265-nm ultraviolet light in inactivating infectious SARS-CoV-2. J Photochem Photobiol 7:100050. https://doi.org/10.1016/J.JPAP.2021.100050

103. McDevitt JJ, Rudnick SN, Radonovich LJ (2012) Aerosol susceptibility of influenza virus to UV-C light. Appl Environ Microbiol 78:1666–1669. https://doi.org/10.1128/AEM.06960-11/ASSET/CF999881-31B7-41E6-820D-07D5B7A90E8F/ASSETS/GRAPHIC/ZAM9991030040001.JPEG

104. Tzoutzas I, Maltezou HC, Barmparesos N, et al (2021) Indoor Air Quality Evaluation Using Mechanical Ventilation and Portable Air Purifiers in an Academic Dentistry Clinic during the COVID-19 Pandemic in Greece. Int J Environ Res Public Health 18:8886. https://doi.org/10.3390/IJERPH18168886

105. Zhai Z, Li H, Bahl R, Trace K (2021) Application of Portable Air Purifiers for Mitigating COVID-19 in Large Public Spaces. Buildings 11:329. https://doi.org/10.3390/BUILDINGS11080329

106. (2013) ASME A17.1-2013/CSA B44-13 Safety code for elevators and escalators

107. Chea B, Bolt A, Agelin-Chaab M, Dincer I (2021) Assessment of effectiveness of optimum physical distancing phenomena for COVID-19. Physics of Fluids 33:051903. https://doi.org/10.1063/5.0046429

108. Dbouk T, Drikakis D (2020) On coughing and airborne droplet transmission to humans. Physics of Fluids 32:053310. https://doi.org/10.1063/5.0011960

109. Zhang Z, Chen Q (2006) Experimental measurements and numerical simulations of particle transport and distribution in ventilated rooms. Atmos Environ 40:3396–3408. https://doi.org/10.1016/J.ATMOSENV.2006.01.014

110. Zhao B, Zhang Y, Li X, et al (2004) Comparison of indoor aerosol particle concentration and deposition in different ventilated rooms by numerical method. Build Environ 39:1–8. https://doi.org/10.1016/J.BUILDENV.2003.08.002

111. ANSYS Inc (2020) ANSYS Fluent Theory Guide

112. Saffman PG (1965) The lift on a small sphere in a slow shear flow. J Fluid Mech 22:385–400. https://doi.org/10.1017/S0022112065000824

113. Li A, Ahmadi G (2007) Dispersion and Deposition of Spherical Particles from Point Sources in a Turbulent Channel Flow. http://dx.doi.org/101080/02786829208959550 16:209–226. https://doi.org/10.1080/02786829208959550

114. Shih TH, Liou WW, Shabbir A, et al (1995) A new k-ϵ eddy viscosity model for high reynolds number turbulent flows. Comput Fluids 24:227–238. https://doi.org/10.1016/0045-7930(94)00032-T

115. Khatoon S, Kim MH (2017) Human Thermal Comfort and Heat Removal Efficiency for Ventilation Variants in Passenger Cars. Energies (Basel) 10:1710. https://doi.org/10.3390/EN10111710

116. Hens HSL (2010) Applied Building Physics Boundary Conditions, Building Performance and Material Properties. Wilhelm Ernst & Sohn

117. Liu M, Chang D, Liu J, et al (2021) Experimental investigation of air distribution in an airliner cabin mockup with displacement ventilation. Build Environ 191:107577. https://doi.org/10.1016/J.BUILDENV.2020.107577

118. B. Awbi H (2008) Ventilation Systems Design and Performance. Taylor & Francis

119. Ameen A, Cehlin M, Larsson U, Karimipanah T (2019) Experimental Investigation of the Ventilation Performance of Different Air Distribution Systems in an Office Environment—Cooling Mode. Energies (Basel) 12:1354. https://doi.org/10.3390/EN12071354

120. Aramendia I, Fernandez-Gamiz U, Lopez-Arraiza A, et al (2018) Experimental and Numerical Modeling of Aerosol Delivery for Preterm Infants. International Journal of Environmental Research and Public Health 2018, Vol 15, Page 423 15:423. https://doi.org/10.3390/IJERPH15030423

121. Chillón SA, Ugarte-Anero A, Aramendia I, et al (2021) Numerical Modeling of the Spread of Cough Saliva Droplets in a Calm Confined Space. Mathematics 2021, Vol 9, Page 574 9:574. https://doi.org/10.3390/MATH9050574

122. Meana-Fernández A, Fernández Oro JM, Argüelles Díaz KM, et al (2019) Application of Richardson extrapolation method to the CFD simulation of vertical-axis wind turbines and analysis of the flow field. Engineering Applications of Computational Fluid Mechanics 13:359–376. https://doi.org/10.1080/19942060.2019.1596160

123. Roache PJ (1998) Verification and validation in computational science and engineering. Albuquerque: Hermosa Publisher

124. Jamil M, Yang XS (2013) A literature survey of benchmark functions for global optimisation problems. International Journal of Mathematical Modelling and Numerical Optimisation 4:150–194. https://doi.org/10.1504/IJMMNO.2013.055204

Appendix A: Upward-Moving Escalator

Table A1. Non-dominated solutions of Pareto front for UME

C	L	V	RH
2.45E-10	4.931	0.699	54.010
2.46E-10	4.926	0.698	54.049
2.46E-10	4.922	0.699	54.296
2.47E-10	4.916	0.697	54.252
2.47E-10	4.913	0.699	54.548
2.48E-10	4.907	0.699	54.703
2.49E-10	4.904	0.699	54.814
2.49E-10	4.902	0.697	54.767
2.50E-10	4.893	0.699	55.171
2.51E-10	4.888	0.695	54.994
2.52E-10	4.882	0.696	55.295
2.53E-10	4.880	0.689	54.825
2.53E-10	4.876	0.696	55.474
2.54E-10	4.874	0.690	55.045
2.54E-10	4.871	0.698	55.737
2.54E-10	3.195	0.403	54.105
2.55E-10	3.191	0.403	54.605
2.57E-10	3.187	0.403	55.105
2.58E-10	3.185	0.403	55.492
2.60E-10	3.182	0.403	55.953
2.62E-10	3.179	0.403	56.483
2.68E-10	3.173	0.403	58.009
2.68E-10	3.169	0.403	58.147
2.70E-10	3.165	0.403	58.598
2.72E-10	3.163	0.403	59.145
2.74E-10	3.158	0.403	59.699
2.82E-10	3.151	0.403	61.580
2.83E-10	3.148	0.403	61.816
2.88E-10	3.144	0.403	62.816
2.92E-10	3.141	0.403	63.816
2.95E-10	3.139	0.403	64.316
3.03E-10	3.136	0.403	65.913
3.18E-10	3.131	0.403	68.810

Appendix B: Downward-Moving Escalator

Table B1.Non-dominated solutions of Pareto front for DME

C	L	V	RH
3.50E-10	2.232	0.700	54.000
3.53E-10	2.213	0.688	54.082
3.56E-10	2.189	0.672	54.064
3.59E-10	2.172	0.661	54.038
3.61E-10	2.155	0.650	54.015
3.65E-10	2.128	0.633	54.019
3.68E-10	2.108	0.619	54.079
3.70E-10	2.090	0.607	54.019
3.74E-10	2.068	0.592	54.023
3.77E-10	2.051	0.580	54.063
3.83E-10	2.014	0.555	54.053
3.86E-10	1.993	0.540	54.047
3.91E-10	1.972	0.524	54.259
3.94E-10	1.947	0.506	54.049
3.99E-10	1.920	0.487	54.039
4.03E-10	1.901	0.473	54.069
4.07E-10	1.879	0.455	54.111
4.13E-10	1.852	0.435	54.107
4.16E-10	1.834	0.421	54.101
4.22E-10	1.809	0.401	54.172
4.42E-10	1.788	0.401	61.880
4.65E-10	1.770	0.403	70.589
4.80E-10	1.752	0.401	76.147
4.86E-10	1.748	0.402	78.259
4.87E-10	1.744	0.400	78.619
4.87E-10	1.743	0.400	78.680
4.91E-10	1.740	0.400	80.259
4.93E-10	1.739	0.401	80.997
4.94E-10	1.736	0.400	81.242
4.94E-10	1.736	0.400	81.242